Modeling Complex Material Systems Using Stochastic Reconstruction and Lattice Particle Simulation

by

Yaopengxiao Xu

A Dissertation Presented in Partial Fulfillment
of the Requirements for the Degree
Doctor of Philosophy

Approved April 2018 by the
Graduate Supervisory Committee:
Yang Jiao, Chair
Yongming Liu
Qinghua Wang
Yi Ren

ARIZONA STATE UNIVERSITY
May 2018

ABSTRACT

In this dissertation, three complex material systems including a novel class of hyperuniform composite materials, cellularized collagen gel and low melting point alloy (LMPA) composite are investigated, using statistical pattern characterization, stochastic microstructure reconstruction and micromechanical analysis. In Chapter 1, an introduction of this report is provided, in which a brief review is made about these three material systems. In Chapter 2, detailed discussion of the statistical morphological descriptors and a stochastic optimization approach for microstructure reconstruction is presented. In Chapter 3, the lattice particle method for micromechanical analysis of complex heterogeneous materials is introduced. In Chapter 4, a new class of hyperuniform heterogeneous material with superior mechanical properties is investigated. In Chapter 5, a bio-material system, i.e., cellularized collagen gel is modeled using correlation functions and stochastic reconstruction to study the collective dynamic behavior of the embed tumor cells. In chapter 6, LMPA soft robotic system is generated by generalizing the correlation functions and the rigidity tunability of this smart composite is discussed. In Chapter 7, a future work plan is presented.

Dedicated to My Family

ACKNOWLEDGMENTS

I am indebted to a number of people who have made my stay at Arizona State University both productive and enjoyable. I thank my family and friends for their support and love, without which I could not have finished this dissertation.

I am sincerely grateful and deeply indebted to my advisor Dr. Yang Jiao, for his continued intellectual and professional guidance and his sincere care for my research. I also sincerely thank my committee members Dr. Yongming Liu, Dr. Yi Ren and Dr. Qing Hua Wang for their guidance and suggestions for my research. My work would not have been possible without close collaboration with my lab mates Dr. Shaohua Chen, Dr. Hechao Li, Pei-en Chen and Long Liang.

Also, I would like to thank our collaborators, Dr. Bo Sun from Oregon State University and Dr. Wanliang Shan from University of Nevada for their consistent support in my projects.

Finally, I would like to thank my family members and my fiancée, Xinyue Xu, for their love and support. They are always at my side.

TABLE OF CONTENTS

Page

CHAPTER Page

LIST OF FIGURES

Figure Page

Figure Page

Figure Page

Figure Page

Figure Page

Figure Page

1. INTRODUCTION

Complex composite materials consist of two or more materials with different properties that form regions large enough to be regarded as continua and which are usually firmly bonded together at the interface to give the composite unique properties. Composite materials are key to many performance-critical structural applications that range from automotive to aerospace transportation because of superior mechanical, thermal and other properties, such as light weight, high strength, corrosion resistance, etc. Composites also provide design flexibility not only because many of them can be molded into complex shapes but also the compositions of such type of materials can also be designed for special demand in industry. One of the key factors that be paid a lot of attention is the microstructure which plays a big role in mechanical performance of composites materials. In an effort to improve the manufacturability and multifunctionality of composite structures, for example, polymer microcomposites and nanocomposties have been developed. They can be characterized by refined microstructure which, when properly ordered, can result in increased performance; small quantities of hard inorganic particles can control the deformation, failure, heat resistance, and thermal degradation properties of polymers. Hence, the improvement of properties of composite materials can be considered from the microstructure. In this dissertation, we focus on three materials system and microstructure, hyperuniform, extracellular matrix and low-melting-point alloy composite.

A hyperuniform random heterogeneous material is one in which the local volume fraction fluctuations in an observation window decay faster than the reciprocal window volume as the window size increases and the infinite-wavelength local volume fraction fluctuations are completely suppressed[1][2]. Recent studies show that this new class of materials are endowed with superior physical properties such as large isotropic photonic band gaps and optimal transport properties[30][31][32]. Here, we employ a stochastic optimization procedure to systematically generate realizations of hyperuniform heterogeneous materials with controllable short-range order, which is quantified using the two-point correlation function $S_2(r)$ associated with the phase of interest[41][42]. Specifically, our procedure generalizes the widely-used Yeong-Torquato reconstruction procedure by

introducing an additional constraint for hyperuniformity and allowing one to only constrain $S_2(r)$ up to a certain cut-off distance γ. By systematically increasing the γ value for a given $S_2(r)$, one can produce a spectrum of hyperuniform heterogeneous materials with varying degrees of short-range order compatible of the specified $S_2(r)$. Moreover, the mechanical performance including both elastic and brittle fracture behaviors of the generated hyperuniform materials is analyzed using a volume-compensated lattice-particle method[62][63][64][65][66]. For purpose of comparison, the corresponding non-hyperuniform materials with the same short-range order are also constructed and their mechanical performance is analyzed. We find although the hyperuniform materials are softer than their non-hyperuniform counterparts, the former generally possesses a significantly higher brittle fracture strength than the latter. This superior mechanical behavior is attributed to the lower degree of stress concentration in the material resulting from the hyperuniform microstructure, which is crucial to crack initiation and propagation.

Statistical pattern characterization and stochastic microstructure reconstruction can also be applied in representation of extracellular matrix. Collective cellular dynamics in the three-dimensional extracellular matrix (ECM) plays a crucial role in many physiological processes such as cancer invasion. Both chemical and mechanical signaling support cell–cell communications on a variety of length scales, leading to collective migratory behaviors[69][70]. Here we conduct experiments using 3D in vitro tumor models and develop a phenomenological model in order to probe the cooperativity of force generation in the collective invasion of breast cancer cells. In our model, cell–cell communication is characterized by a single parameter that quantifies the correlation length of cellular migration cycles. We devise a stochastic reconstruction method to generate realizations of cell colonies with specific contraction phase correlation functions and correlation length a. We find that as a increases, the characteristic size of regions containing cells with similar contraction phases grows. For small a values, the large fluctuations in individual cell contraction phases smooth out the temporal fluctuations in the time-dependent deformation field in the ECM. For large a values, the periodicity of an individual cell contraction cycle is clearly manifested in the temporal variation of the overall deformation field in the ECM. Through quantitative comparisons of the simulated and experimentally measured deformation

fields, we find that the correlation length for collective force generation in the breast cancer discoid in geometrically micropatterned ECM (DIGME)[88] system is $a \approx 25$ μm, which is roughly twice the linear size of a single cell. One possible mechanism for this intermediate cell correlation length is the fiber-mediated stress propagation in the 3D ECM network in the DIGME system[31][32].

Another interesting problem is to effectively quantify the microstructure of smart composite and provide useful guidance for material design in order to have a good rigidity turnability[97]. Tunable dry adhesion is a crucial mechanism in soft (compliance) gripping. The grasping force, mainly originated from the van der Waals' force between the adhesive composite and the object to be gripped, can be controlled by reversibly varying the physical properties (e.g., stiffness) of the composite via external stimuli. The maximal grasping force F_{max} and its tunability depend on, among other factors, the stress distribution on the gripping interface and its fracture dynamics (during detaching), which in turn are determined by the composite microstructure. Here, we present a computational framework for the modeling and design of a class of binary smart composites containing a porous LMA phase and a polymer phase, in order to achieve desirable dynamically tunable dry adhesion. In particular, we employ spatial correlation functions to quantify, model and represent the binary composites, from which a wide spectrum of realistic virtual 3D composite microstructures can be generated using stochastic optimization. VCLP method is then employed to model the dynamic interfacial fracture process to compute F_{max} for different composite microstructures. We investigate two mechanisms for dry adhesion tuning enabled by the composite, including the interface defect tuning (via thermal expansion of the LMA phase due to Joule heating) and bulk rigidity tuning (via melting of the LMA phase due to Joule heating). We find that for an optimal microstructure among the ones studied here, a 6-fold reduction of Fmax can be achieved via interface defect tuning. This tunability is reduced by coating the composite interface with an extra layer of polymers in the case of rigidity tunning. Our computational results can provide valuable guidance for experimental fabrication of the LMA-polymer composites.

The generation of realizations of heterogeneous materials with specified but limited microstructural information is an intriguing inverse problem of both fundamental and practical importance. In this dissertation, a stochastic reconstruction process has been used to realize variety of

microstructures based on different statistical information, in which, one starts with a given, arbitrarily chosen, initial configuration of random medium and a set of reference functions. The medium can be a dispersion of particle-like building blocks or, more generally, a digitized image. The reference statistical functions quantitatively store the structure information and describe the desirable statistical characteristics of the target structure. The method proceeds to find a realization configuration, in which calculated correlations functions best match the reference functions. This is achieved by minimizing the sum of squared differences between the calculated and reference functions. Then the microstructure of interest can be inversed reconstructed via stochastic optimization techniques, such as the simulated annealing method.

Numerical simulations have been one of the most powerful tools of the solution for solid mechanical analysis of materials. In this report, Lattice particle method has been used for elastic and fracture properties analysis of these three materials systems mentioned above, hyperuniform and extracellular matrix. Lattice particle method, as the discretize approach, treats continuum materials as a combination of great number of material points. According to the constitutive relation, the model introduced local interaction potential of neighbor material points U_s and non-local virtual potential U_V to overcome the Poisson ratio problem in conventional discrete approach. In the meanwhile, the model enables the random crack initiation and propagation interaction during the tension or compression process which is a big issue in continuum based model.

In the following of this dissertation, the stochastic reconstruction method will be introduced in the chapter 2. In chapter 3, the briefly introduction of lattice particle method for mechanical analysis will be shown. Then the hyperuniform heterogeneous materials microstructure reconstruction and superior mechanical analysis will be discussed in chapter 4. In chapter 5, we provide the introduction of phase correlation reconstruction and the analysis of collective cellular dynamics. In the chapter 6, the generalized two-point correlation function will be introduced in the representation of LMPA composite and tunability of rigidity will be discussed. At the end of the report, a future work will be shown in chapter 7.

2. STOCHASTIC RECONSTRUCTION VIA SIMULATED ANNEALING

2.1 Two-point correlation function

Reconstruction of complex heterogeneous material system based on limited microstructural information is an interesting inverse problem[1]. An effective reconstruction process enables one to extract key information from a microstructure image and generate accurate reconstructed structures for subsequent analysis. This method provides people an efficient way to estimate the macroscopic properties without destructing the real sample or structure which is very necessary in many relevant research or industry area. Another advantage of reconstruction method is a three-dimensional structure of the heterogeneous material can be successfully reproduced using information extracted from two-dimensional slice cut through the material. Such ways are of great value in a wide variety of fields, including petroleum engineering, biology and medicine, because in many cases one only has two-dimensional information such as a micrograph or image.

Reproducing the heterogeneous material systems based on statistical functions is often referred to as a construction problem. In construction approach, researchers can identify the characteristics from the correlation function and in particular, people can also determine how much information contained in the statistical descriptors. In other words, a successful (re)construction approach not only can realize the original structure from lower level information source (ie, from 2D to 3D), but also enables one to control the final microstructure under controlling the statistical functions.

Gaussian random fields (GRF), as a popular (re)construction procedure, successively representing the phase and structure of material systems by going through a linear and a nonlinear filter to yield the discrete values. The original work of Gaussian random field in statistical topography was established by Rice [5, 6]. Then a lot of development and application had been done base on this work [7, 8, 9, 10]. In Gaussian random fields, it assumes that the two-phase random medium can be completely described by volume fraction and standard two-point correlation function, which is really model dependent [11].

Recently, Torquato and coworkers have introduced another stochastic (re)construction technique [1, 2, 3, 4]. In this method, one starts with a given, arbitrarily chosen, initial configuration of random medium and a set of target functions. The medium can be a dispersion of particle-like building blocks or, more generally, a digitized image [1, 2, 3, 4]. The statistical functions describe the desirable statistical characteristics of the structure of interest, which can be various correlation functions taken either from experiments or theoretical considerations. The method proceeds to find a realization (configuration) in which calculated correlation functions best match the target functions. This is achieved by minimizing the sum of squared differences between the calculated and target functions via stochastic optimization techniques, such as the simulated annealing method. This method is applicable to multidimensional and multiphase media, and is highly flexible to include any type and number of correlation functions as microstructural information. It is both a generalization and simplification of the aforementioned Gaussian-field (re)construction technique. Moreover, it does not depend on any particular statistics.

There are many different types of statistical descriptors that can be chosen as target functions as shown in the FIG.1; the most basic one is the aforementioned two-point correlation function S2(r), which is obtainable from small-angle X-ray scattering. However, not every hypothetical two-point correlation function corresponds to a realizable two-phase medium. Therefore, it is of great fundamental and practical importance to determine the necessary conditions that realizable two-point correlation functions must possess. Shepp showed that convex combinations and products of two scaled autocovariance functions of one-dimensional media (equivalent to two-point correlation functions; see definition below) satisfy all known necessary conditions for a realizable scaled autocovariance function. More generally, we will see that a hypothetical function obtained by a particular combination of a set of realizable scaled autocovariance functions corresponding to d-dimensional media is also realizable.

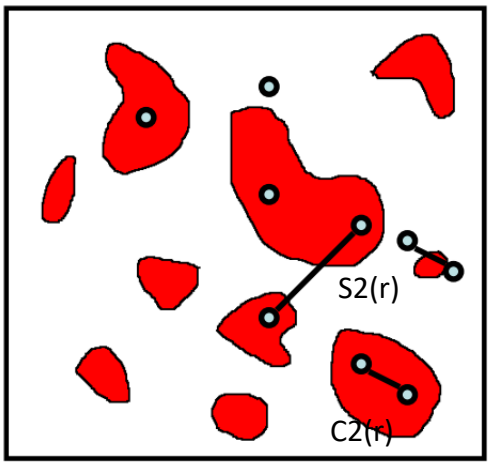

Fig. 2.1 Schematic illustration of the probability interpretation of the correlation functions. The 1- and 2-point configurations (i.e., one point and line segments) shown represent the events contributing to the associated correlation functions.

The ensuing discussion leading to the definitions of the n-point correlation functions follows closely the one given by Torquato. Consider a realization of a two-phase random heterogeneous material within d-dimensional Euclidean space $\mathbb{R}^d$. To characterize this binary system, in which each phase has volume fraction $\emptyset^{(i)}(x)$, it is customary to introduce the indicator function $I^{(i)}(x)$ defined as

$$I^{(i)}(x) = \begin{cases} 1, & x \in V_i \\ 0, & x \in \bar{V}_i \end{cases} \tag{2.1}$$

where $V_i \in \mathbb{R}^d$ is the region occupied by phase i and $\overline{V_i} \in \mathbb{R}^d$ is the region occupied by the other phase. The statistical characterization of the spatial variations of the binary system involves the calculation of n-point correlation functions:

$$S_n^{(i)}(x_1, x_2, \cdots, x_n) = \langle I^{(i)}(x_1) I^{(i)}(x_2) \cdots I^{(i)}(x_n) \rangle \tag{2.2}$$

where the angular brackets $\langle \cdots \rangle$ denote ensemble averaging over independent realizations of the random medium.

For statistically homogeneous media, the n-point correlation function depends not on the absolute positions but on their relative displacements, i.e.,

$$S_n^{(i)}(x_1, x_2, \cdots, x_n) = S_n^{(i)}(x_{12}, \cdots, x_{1n}) \tag{2.3}$$

for all n ≥ 1, where $x_{ij} = x_j - x_i$. Thus, there is no preferred origin in the system, which in Eq. (3) we have chosen to be the point x_1. In particular, the one-point correlation function is a constant everywhere, namely, the volume fraction $\emptyset_i$ of phase i, i.e.,

$$S_1^{(i)} = \langle I^{(i)}(x) \rangle = \emptyset_i \tag{2.4}$$

and it is the probability that a randomly chosen point in the medium belongs to phase i. For statistically isotropic media, the n-point correlation function is invariant under rigid-body rotation of the spatial coordinates. For $n \leq d$, this implies that $S_n^{(i)}$ n depends only on the distances $x_{ij} = |x_{ij}| \, (1 \leq i < j \leq n)$. For $n \geq d + 1$, it is generally necessary to retain vector variables because of chirality of the medium.

The two-point correlation function $S_2^{(i)}(x1, x2)$ defined as

$$S_2^{(i)} = \langle I^{(i)}(x_1) I^{(i)}(x_2) \rangle \tag{2.5}$$

is one of the most important statistical descriptors of random media. It also can be interpreted as the probability that two randomly chosen points x_1 and x_2 both lie in phase i. For statistical homogeneous and isotropic media, $S_2^{(i)}$ only depends on scalar distances, i.e.,

$$S_2^{(i)}(x_1, x_2) = S_2^{(i)}(|\boldsymbol{r}|) \tag{2.6}$$

where $r = x_{12}$.

Global information about the surface of the *i*th phase may be obtained by ensemble averaging the gradient of $I^i(x)$.

2.2 Stochastic Optimization

Generally, consider a given set of correlation functions $f_n^{\alpha}\,(r_1, r_2, \ldots, r_n)$ of the phase of interest that provides partial information on the random medium. The index α is used to denote the type of correlation functions. Note that the set of f_n^{α} should not be confused with the basis function set $\wp$, the former contains correlation functions of different type, i.e., two-point correlation function, lineal-path function, two-point cluster function, etc., while the latter contains basis functions through which the scaled autocovariance function of the medium of interest can be expressed. The information contained

in f_n^α could be obtained either from experiments or it could represent a hypothetical medium based on simple models. In both cases we would like to generate the underlying micro-structure with a specified set of correlation functions. In the former case, the formulated inverse problem is frequently referred to as a “reconstruction” procedure, and in the latter case as a “construction”. As we have noted earilier, it is natural to formulate the construction or reconstruction problem as an optimization problem [1, 2, 3, 4]. The discrepancies between the statistical properties of the best generated structure and the imposed ones is minimized. This can be readily achieved by introducing the “energy” function E defined as a sum of squared differences between target correlation functions, which we denote by $\widehat{f_n^\alpha}$, and those calculated from generated structures, i.e.,

$$E = \sum_{r_1, r_2, \cdots r_n} \sum_a [f_n^\alpha(r_1, r_2, \cdots r_n) - \widehat{f_n^\alpha}(r_1, r_2, \cdots r_n)]^2 \tag{2.7}$$

Note that for every generated structure (configuration), these is a set of corresponding f_n^α . If we consider every structure (configuration) as a “state” of the system, E can be considered as a function of the states. The optimization technique suitable for the problem at hand is the method of simulated annealing. It is a popular method for the optimization of large-scale problems, especially those where a global minimum is hidden among many local extrema. The concept of finding the lowest energy state by simulated annealing is based on a well-known physical fact: If a system is heated to a high temperature T and then slowly cooled down to absolute zero, the system equilibrates to its ground state. At a given temperature T, the probability of being in a state with energy E is given by the Boltzmann distribution P(E) ~ exp(−E/T). At each annealing step k, the system is allowed to evolve long enough to thermalize at T(k). The temperature is then lowered according to a prescribed annealing schedule T(k) until the energy of the system approaches it ground state value within an acceptable tolerance. It is important to keep the annealing rate slow enough in order to avoid trapping in some metastable states. In our problem, the discrete configuration space includes the states of all possible pixel allocations. Starting from a given state (current configuration), a new state (new configuration) can be obtained by interchanging two arbitrarily selected pixels of different phases. This simple evolving

procedure preserves the volume fraction of all involved phases and guarantees ergodicity in the sense that each state is accessible from any other state by a finite number of interchange steps. However, in the later stage of the procedure, biased and more sophisticated interchange rules, i.e., surface optimization, could be used to improve the efficiency. We choose the Metropolis algorithm as the acceptance criterion: the acceptance probability P for the pixel interchange is given by

$$P(E_{old} - E_{new}) = \begin{cases} 1, & \Delta E < 0, \\ \exp\left(-\frac{\Delta E}{T}\right), & \Delta E \geq 0, \end{cases} \tag{2.8}$$

where $\Delta E = E_{old} - E_{new}$. The temperature T is initially chosen so that the initial acceptance probability for a pixel interchange with $\Delta E \geq 0$ averages approximately 0.5. An inverse logarithmic annealing schedule which decreases the temperature according to $T(k) \sim 1/\ln(k)$ would in principle evolve the system to its ground state. However, such a slow annealing schedule is difficult to achieve in practice. Thus, we will adopt the more popular and faster annealing schedule $(k)/T(0) = \lambda^k$, where constant λ must be less than but close to one. This may yield suboptimal results, but, for practical purposes, will be sufficient. The convergence to an optimum is no longer guaranteed, and the system is likely to freeze in one of the local minima if the thermalization and annealing rate are not adequately chosen. The two-point correlation function of a statistically homogeneous and isotropic medium is the focus of this dissertation. In this case, equation reduces to

$$E = \sum_i [S_2(r_i) - \widehat{S_2}(r_i)]^2 \tag{2.9}$$

Since for every configuration (structure), the corresponding two-point correlation function needs to be computed, the efficiency of the construction or reconstruction is mainly determined by the efficiency of the S2-sampling algorithm. Furthermore, the properties of generated configurations (structures), i.e., isotropy of the medium, is also affected by the S2-sampling algorithm. One of the most commonly used and efficient S2-sampling algorithms is the orthogonal-sampling algorithm introduced by Yeong and Torquato [1, 2]. Due to the isotropic nature of the medium, every sampling direction should be equivalent. For simplicity, two orthogonal directions (usually the horizontal and vertical directions of a square lattice) are chosen and the two-point correlation function is sampled along these directions and averaged.

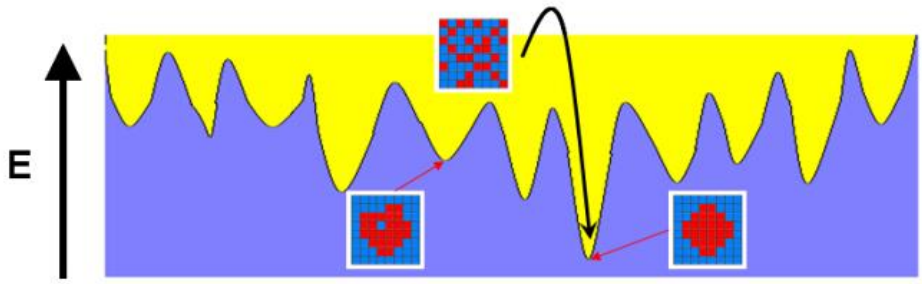

Fig. 2.2 Schematic illustration of the simulated annealing reconstruction procedure. The acceptance of energy-increasing trial microstructure allows the system to escape from local energy minima and thus, increases the probability of convergence to the global minimum.

At each pixel interchange, only the values of S2(r) sampled along the rows and columns that contain the interchange pixels are changed. Thus, the complexity of the algorithm is O(N), where N is the linear size of the system. However, for certain media with long-range correlations, the generated media have microstructures with two orthogonal anisotropic directions due to the biased sampling. Modifications of the orthogonal-sampling algorithm to preserve the isotropy of the underlying medium have been proposed, such as adding more sampling directions and using more isotropic lattices [3, 4]. Cule and Torquato introduced a new isotropy-preserving fast Fourier transform (FFT) algorithm [3]. At each pixel interchange step, the two-point correlation function S2(r) containing angle information is calculated in momentum space using an efficient FFT algorithm. Since information of all directions is considered, the generated media always have the required isotropy structures. However, since the complexity of FFT is O(N log2 N), the algorithm is relatively time consuming. We have developed an efficient and isotropy-preserving algorithm, namely, the LatticePoint algorithm by considering the black pixels as hard “particles” on a particular lattice. The two-point correlation function is then computed in a similar way of obtaining the pair correlation function g2(r) for an isotropic point process [1]. At each Monte-Carlo step, the randomly selected “particle” (or we can think the black pixel in the binary image, the white pixels represent the background) is given a random displacement subjected to the

nonoverlapping constraint and the distances between the moved “particle” and all the other “particles” need to be recomputed. Thus, the complexity of the algorithm is O(N). Since all directions are effectively sampled, constructions based on the angle-averaged S2(r) well preserve isotropy of the media. A detailed discussion and applications of the algorithm will be included in the next few chapters and provide several illustrative examples generated from this algorithm.

3. LATTICE PARTICLE METHOD

3.1 Overview

Numerical simulation has been one of the most powerful tools of the solutions for solid mechanical analysis of materials and has two generally groups: the continuum-based approach and the discontinuous approach. Continuum-based model, such as finite element method, extended finite element method, and etc., provides a good analysis performance in elasticity and plasticity. However, difficulties are often encountered to simulate the crack or fracture problem. This kind of method is based on solving the approximate solution of differential equation and the most common problem in continuum-based model is the singularity related issues when dealing with discontinuity. Many numerical models have been proposed to overcome these problems, such as setting up pre-existed crack or remeshing. But they bring other issues like dramatically increasing the computational cost.

The problem becomes much more complicated when random cracking occurs in the simulation domain and tracking of arbitrary crack initiation and propagation is very difficult in the conventional continuum-based simulation framework. Discrete-based approach, represented by a combination of a great number of discrete material points, introduce the interaction among a material point itself and all its neighbors instead of differential form in continuum model and simulate the underlying physics on the level of micro-mechanical rules. The governing law of the dynamics of particles is Newton's equations of motion and this basic idea is very similar to the molecular dynamics but with constrain among neighbor material points or even further. These equations are usually discretized in time and involve calculation of the integral expression, in which the spatial derivatives that require the hypothesis of continuity of the material have been replaced. Hence, lattice particle method, which has discontinuous formulations of solid, can accurate describe the interaction between particle and are especially suitable for the simulation of crack initiation, propagation, and branching, etc.

Many existing particle-based studies have been proposed for the simulation of dynamic fracture of heterogeneous materials, such as rock, concrete, ceramics, and refractory metals [12]. However, the only normal springs employed in the conventional particle-based models, which can be treated as the

axial constraint between particles, bring the fixed Poisson ratio issue (e.g. 1/3 in 2D and 1/4 in 3D cases) for both regular and irregular particle packing [12]. And this intrinsic problem has been overcome by the proposed novel Volume-Compensated Particle method (VCPM), which can handle the arbitrary Poisson's ratio effect and the plastic deformation which does not rely on the classical plasticity theories. The key idea of this lattice particle model is to introduce two potential descriptors, local pair-wise potential U_S, and non-local deformation potential U_V [12]. In this dissertation, this model proposed by H. Chen has been modified for mechanical analysis in our three complex material systems.

3.2 Particle packing types

Similar to all particle-based simulation methods, particle packing also directly affects the formulation and model parameter determination in VCPM [13]. Several possible packing types could be employed in the model, e.g., the hexagonal packing and the square packing, and square packing has been used in our research because of the simplicity and more efficient computation cost. As shown in Fig.3, the microstructure can be imagined as discretized into square packing "particles" and each particle is connected to its first nearest neighbors and second nearest neighbors by spring. In classical lattice models, square packing (Fig. 1) has been investigated and the restriction on Poisson's ratio exists in these cases (Wang et al., 2009). For the square packing, there is no shear contribution from the nearest neighbors.

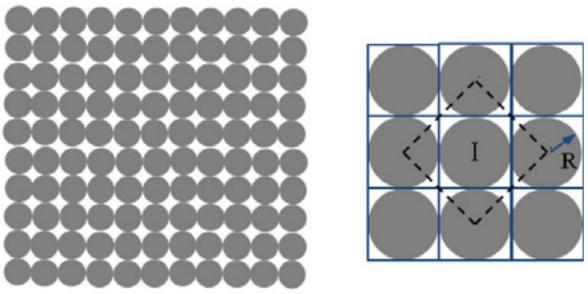

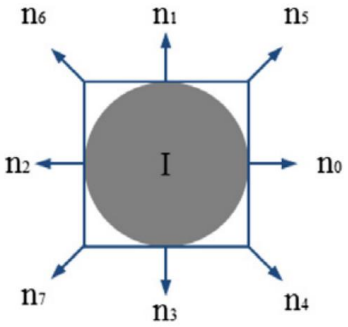

Fig. 3.1 Schematic illustration for 2D particle packing

By taking the second nearest neighbors into consideration, shear can be introduced into the square packing. Once the particle packing is selected, a unit cell that periodically repeating in the discrete model is chosen to calculate the potential energy. The strain energy of a unit cell can be calculated based on the classical lattice theory, in which the normal vectors of each pair of particles are required. A normal vector is the direction vector between a centered particle and its neighboring particles.

3.3 Model coefficients

The key idea of the proposed VCPM is that two potential terms are used to describe the strain energy U_{cell} stored in a unit cell: the energy stored in the local pair-wise neighboring springs Us and the energy associated with the volume change of a unit cell U_v . Note that only a half spring is used in each unit cell while calculating the strain energy, which avoids overlapping. Mathematically, the above hypothesis can be expressed as

$$\mathrm{U}_{cell} = U_s + U_v \tag{3.1}$$

The strain energy stored in the springs has a different form from the hexagonal packing since two types of spring is adopted in square packing. The strain energy Us s is

$$\mathrm{U}_s^{square} = \frac{1}{2}\sum_{J=0}^{3} k_1^{square}(\delta l_{ij})^2 + \frac{1}{2}\sum_{J=4}^{7} k_2^{square}(\delta l_{ij})^2 \tag{3.2}$$

where superscript s indicated the square packing, $\mathrm{k}_1^{\mathrm{s}}$ and $\mathrm{k}_2^{\mathrm{s}}$ are the spring stiffness parameters for springs connecting a center particle with the nearest and the second nearest neighbors, respectively.

The strain energy with the volume change of a unit cell is the same as that of the hexagonal packing, except the volume of a unit cell is $\mathrm{V}^s = 4\mathrm{R}^2$ for square packing. For plane strain case, the strain energy of volume change of a unit cell is

$$\mathrm{U}_v^{square} = \frac{1}{2} V^s T^s (\varepsilon_v^s)^2 = 2R^2 T^s (\varepsilon_{11}^2 + 2\varepsilon_{11}\varepsilon_{22} + \varepsilon_{22}^2) \tag{3.3}$$

Using the characteristic of elastic material that the strain energy is conservative, the stiffness tensor can be obtained in the Voigt form as

$$C_{ijkl} = \frac{1}{V^s} \frac{(\partial^2 \mathrm{U}_{cell}^{square})}{\partial \varepsilon_{ij} \partial \varepsilon_{kl}} \tag{3.4}$$

the stiffness matrix for square packing under plane strain assumption is

$$C = \begin{bmatrix} \frac{(k_1^S + k_2^S)}{2} + T^s & \frac{k_1^S}{2} + T^s & 0 \\ \frac{k_2^S}{2} + T^s & \frac{(k_1^S + k_2^S)}{2} + T^s & 0 \\ 0 & 0 & \frac{k_2^S}{2} \end{bmatrix} \tag{3.5}$$

Comparing the components with the stiffness matrix of 2D isotropic homogeneous materials, the potential coefficients can be determined uniquely as

$$k_1^s = \frac{2E}{1+v}, k_2^s = \frac{E}{1+v}, T^s = \frac{E(4v-1)}{2(1+v)(1-2v)} \tag{3.6}$$

By definition, the volumetric strain of a unit cell in square packing can be approximated as

$$\varepsilon_v^s = \frac{\Delta V}{V} \approx \frac{(\sqrt{2}-1)\sum_{J=0}^{7} \delta l_{ij}}{2R} \tag{3.7}$$

Thus, the total strain energy of a unit cell in square packing can be rewritten in terms of the length change of a half spring as

$$\mathrm{U}_{cell}^{square} = \frac{1}{2}\sum_{J=0}^{3} k_1^{square} (\delta l_{ij})^2 + \frac{1}{2}\sum_{J=4}^{7} k_2^{square} (\delta l_{ij})^2 + (\frac{3-2\sqrt{2}}{2}) T^s (\sum_{J=0}^{7} \delta l_{ij})^2 \tag{3.8}$$

From equation above, the interaction force within half spring can be obtained as

$$f_{ij} = \begin{cases} k_1^{square}\delta l_{ij} + (\frac{2\sqrt{2}-3}{2})\, T^s(\sum_{J=0}^{7}\delta l_{ij}), & J = 0,1,2,3 \\ k_2^{square}\delta l_{ij} + (\frac{2\sqrt{2}-3}{2})\, T^s(\sum_{J=0}^{7}\delta l_{ij}) & J = 4,5,6,7 \end{cases} \tag{3.9}$$

As a short summary, the model parameters under 2D elastic cases have been derived for square packing. The three-dimensional coefficients can be derived in the equivalent way [13].

4. HYPERUNIFORM HETEROGENEOUS MATERIAL

4.1 Introduction

The concept of hyperuniformity was first introduced by Torquato and Stillinger for many-particle systems [1] and was subsequently generalized by Zachary and Torquato to heterogeneous materials [2]. Specifically, a hyperuniform point pattern (e.g., a collection of particle centers in a many-body system) is one in which the local number density fluctuations grow slower than the volume of an observation window as the window size increases, implying that the infinite-wavelength number density fluctuations completely vanish. Similarly, a hyperuniform random heterogeneous material is one in which the local volume fraction fluctuations in an observation window decay faster than the reciprocal window volume as the window size increases and the infinite-wavelength local volume fraction fluctuations are

completely suppressed.

The property of hyperuniformity has been identified in many physical and biological systems, including the density fluctuations in early universe [3], maximally random jammed packing of hard particles [4][5][6][7], certain exotic classical ground states of many-particle systems, jammed colloidal systems [8][9][10][11][12][13][14][15] , driven non-equilibrium systems, certain quantum ground states, avian photoreceptor patterns, organization of adapted immune systems, and amorphous silicon, to name but a few. It has been suggested that hyperuniformity can be considered as a new state of matter [14], which possesses a hidden order in between of that of a perfect crystal and a totally disordered system (e.g., a Poisson distribution of points). In addition, it has been shown that hyperuniform heterogeneous materials can be designed to possess superior physical properties including large isotropic photonic band gaps and optimized transport properties. Very recently, the notation of hyperuniformity has been further generalized to vector fields, anisotropic and inhomogeneous systems. In addition, materials with hyperuniform structures have also been successfully fabricated or synthesized using different techniques.

A hyperuniform many-particle system with a specific degree of spatial order can be reconstructed using the collective coordinate approach (CCA). Specifically, in CCA an initial random configuration of

particles is evolved using stochastic optimization to a final state possessing a prescribed structure factor $S(k)$ with the small-wavenumber limit $\lim_{k\to 0} S(k) = 0$ to ensure hyperuniformity. The degree of order in the system can be controlled by imposing different forms of $S(k)$, satisfying the condition $\lim_{k\to 0} S(k) = 0$. This approach has recently been generalized to reconstruct hyperuniform heterogeneous materials possessing a prescribed spectral density $\hat{\chi}(k)$ with $\lim_{k\to 0} \hat{\chi}(k) = 0$. In this case, an initial random distribution of pixels representing the phase of interest is evolved using stochastic optimization to a final microstructure with the prescribed $\hat{\chi}(k)$. The hyperuniform condition $\lim_{k\to 0} \hat{\chi}(k) = 0$ for heterogeneous materials is discussed in detail in chapter 4.2.

In this chapter, we devise an alternative procedure to systematically generate realizations of hyperuniform heterogeneous materials with controllable short-range order. Instead of evolving the material microstructure to achieve a prescribed spectral density $\hat{\chi}(k)$, in our reconstruction the final microstructure is required to match a set of prescribed spatial correlation functions (e.g., the two-point correlation function S_2) for the phase of interest while simultaneously satisfying the hyperuniform condition $\lim_{k\to 0} \hat{\chi}(k) = 0$. This is achieved by generalizing the Yeong-Torquato reconstruction procedure to introduce an additional energy term for the hyperuniform constraint besides the energy terms for the prescribed correlation functions. To control the short-range order in the system, we allow one to only constrain the prescribed correlation function up to a certain cut-off distance γ in the reconstruction. By systematically increasing the γ value, one can produce a spectrum of hyperuniform heterogeneous materials with varying degrees of short-range order compatible of the specified correlation function. For purpose of comparison, the corresponding non-hyperuniform materials with the same correlation function and the constraint cut-off value γ are also generated, which possess a microstructure that are statistically indistinguishable from that of the corresponding hyperuniform materials on small length scales.

We also study the mechanical performance of the generated hyperuniform and corresponding non-hyperuniform materials, including both elastic and failure behaviors using a volume-compensated lattice-particle method. Although the hyperuniform materials are softer than their non-hyperuniform

counterparts, i.e., with a smaller Young's modulus, the hyperuniform materials generally possess a superior brittle fracture behavior, including both a higher resistance to crack initiation and a larger fracture strength. We find this superior mechanical behavior is attributed to the lower degree of stress concentration in the material resulting from the hyperuniform microstructure, which is crucial to crack initiation and propagation.

The rest of this chapter is organized as follows: In 4.2, we provide definitions of quantities that are relevant to hyperuniform heterogeneous materials. In 4.3, we present the stochastic reconstruction procedure for generating hyperuniform heterogeneous materials with varying degrees of short-range order. In 4.4 and 4.5, we respectively provide detailed analysis on the structural and mechanical properties of the generated hyperuniform materials and their non-hyperuniform counterparts. In 4.6, we make concluding remarks.

4.2 Definitions for hyperuniform heterogeneous materials

4.2.1 n-Point Correlation Function

In general, the microstructure of a heterogeneous material can be uniquely determined by specifying the indicator functions associated with all of the individual phases of the material [21,22]. Without loss of generality, we focus on two-phase materials (binary medium) in this work. We note that the generalization of the subsequent discussion to a multiple phase system is straightforward.

Consider a statistically homogeneous material M occupying the region $\mathcal{V}$ in $\mathbb{R}^d$ $(d = 1,2,3)$ which is partitioned into two disjoint phases: phase 1, a region $\mathcal{V}_1$ of volume fraction $\emptyset_1$ and phase 2, a region $\mathcal{V}_2$ of volume fraction $\emptyset_2$. It is obvious that $\mathcal{V}_1 \cup \mathcal{V}_2 = \mathcal{V}$ and $\mathcal{V}_1 \cap \mathcal{V}_2 = 0$. The indicator function $I^{(i)}(x)$ of phase i is given by

$$I^{(i)}(x) = \begin{cases} 1, & x \in \mathcal{V}_i \\ 0, & x \in \widehat{\mathcal{V}}_i \end{cases} \tag{4.1}$$

for $i = 1,2$ with $\mathcal{V}_i \cup \widehat{\mathcal{V}}_i = \mathcal{V}$ and

$$I^{(1)}(x) + I^{(2)}(x) = 1 \tag{4.2}$$

The n-point correlation function $S_n^{(i)}$ for phase i is defined as follows:

$$S_n^{(i)}(x_1, x_2, \cdots, x_n) = \langle I^{(i)}(x_1) I^{(i)}(x_2) \cdots I^{(i)}(x_n) \rangle \tag{4.3}$$

where the angular brackets $\langle \cdots \rangle$ denote ensemble averaging over independent realizations of the random medium.

The two-point correlation function $S_2^{(i)}$ for phase i, the focus of this study, is defined by

$$S_2^{(i)} = \langle I^{(i)}(x_1) I^{(i)}(x_2) \rangle \tag{4.4}$$

As pointed out in Sec. I, for a statistically homogeneous medium, $S_2^{(i)}$ is a function of the relative displacements of point pairs, i.e.,

$$S_2^{(i)}(\boldsymbol{x_1}, \boldsymbol{x_2}) = S_2^{(i)}(\boldsymbol{x_1} - \boldsymbol{x_2}) = S_2^{(i)}(|\boldsymbol{r}|) \tag{4.5}$$

where $\boldsymbol{r} = \boldsymbol{x_1} - \boldsymbol{x_2}$. In the infinite volume limit, if the medium is also ergodic the ensemble average is equivalent to the volume average, i.e.,

$$S_2^{(i)}(\boldsymbol{r}) = \lim_{V \to \infty} \frac{1}{V} \int_V I^{(i)}(\boldsymbol{x}) I^{(i)}(\boldsymbol{x} + \boldsymbol{r})\, dx \tag{4.6}$$

If the medium is also statistically isotropic, $S_2^{(i)}$ is a radial function, depending on the separation distances of point pairs only, i.e.,

$$S_2^{(i)}(\boldsymbol{x_1}, \boldsymbol{x_2}) = S_2^{(i)}(|\boldsymbol{r}|) = S_2^{(i)}(r) \tag{4.7}$$

Interested readers are referred to Ref. [22] for a detailed discussion of $S_2^{(i)}$ and other higher order $S_n^{(i)}$. Henceforth, we will drop the superscript i in $S_2^{(i)}$ for simplicity. Without further elaboration, S_2 is always the two-point correlation function of the phase of interest.

The two-point correlation function S_2 can be efficiently computed from given digital images of a material, in which the microstructure is represented as a 2D (or 3D) array of pixels (or voxels), in which value of each pixel indicates the local state (e.g., phases) of that pixel. For a binary system, the array is simply a collection of black and white pixels on a regular lattice. The probabilistic interpretation of the correlation functions enable us to develop a general sampling method for the reconstruction of statistically homogeneous and isotropic digitized textures based on the ``lattice-gas'' formalism, which is introduced in Refs [23, 24] and generalized in Ref [25]. In the generalized formalism, pixels with different values (occupying the lattice sites) correspond to distinct local states and pixels with the same value are considered to be ‘’molecules’’ of the same “gas” species. In the case of S_2, all ‘’molecules’’

are of the same species. We denote the number of lattice-site separation distances of length r by $N_s(r)$ and the number of molecule-pair separation distances of length r by $N_p(r)$. Thus, the fraction of pair distances with both ends occupied by the phase of interest, i.e., the two-point correlation function, is given by $S_2(r) = N_P(r)/N_S(r)$.

4.2.2 Hyperuniformity in heterogeneous materials

A hyperuniform heterogeneous material has the property that the variance in the volume fraction of the phase of interest in an observation window Ω decays more quickly than the reciprocal volume of that window [15]. In the case of a spherical observation window, this definition implies that the variance $\sigma_\tau^2(R)$ in the local volume fraction $\tau(x)$ decays more quickly than R^{-d} in d dimensions, where R is the radius of the observation window.

In particular, the local volume fraction $\tau(x)$ of the phase of interest is defined as:

$$\tau_i(x;R) = \frac{1}{v(R)} \int I(z)\omega(z-x;R)dz \tag{4.8}$$

where $v(R)$ is the volume of the observation window, ω is the corresponding indicator function, and I is the indicator function of the phase of interest. Using this definition, the variance σ_τ^2 in the local volume fraction is given by:

$$\sigma_\tau^2 = \frac{1}{v(R)} \int \chi(\boldsymbol{r})\alpha(\boldsymbol{r};R)d\boldsymbol{r} \tag{4.9}$$

where $\chi(\boldsymbol{r})$ is the autocovariance function, i.e $\chi(\boldsymbol{r}) = S_2(r) - \phi^2$, and $\alpha(\boldsymbol{r};R)$ is the scaled intersection volume which has the support [0,2R], the range [0,1], and the following integral representation:

$$\alpha(r;R) = c(d) \int_0^{\cos^{-1}[\frac{r}{2R}]} \sin^d(\theta)d\theta \tag{4.10}$$

where $c(d)$ is a *d*-dimensional constant given by

$$c(d) = \frac{2\Gamma\left(1+\frac{d}{2}\right)}{\pi^{\frac{1}{2}}\Gamma\left[\frac{d+1}{2}\right]} \tag{4.11}$$

The variance in the local volume fraction admits the asymptotic expansion [15]:

$$\sigma_\tau^2 = \frac{\rho}{2^d\phi}\left\{A_\tau\left(\frac{D}{R}\right)^d + B_r\left(\frac{D}{R}\right)^{d+1} + o\left[\left(\frac{D}{R}\right)^{d+1}\right]\right\} \tag{4.12}$$

$$\mathrm{A}_\tau = \int_{\mathbb{R}^d} \chi(r)dr = \lim_{||k||\to 0} \hat{\chi}(k) \tag{4.13}$$

$$\mathrm{B}_\tau = -\frac{k(d)}{D}\int_{\mathbb{R}^d} ||r||\chi(r)dr = \frac{1}{\pi v(1) D}\int_{\mathbb{R}^d} \frac{\hat{\chi}(k)}{||k||^{d+1}}dk \tag{4.14}$$

The coefficients A_τ and B_τ in above equation control the asymptotic scaling of the fluctuations in the local volume fraction. By definition, a hyperuniform heterogeneous material possesses a local volume fraction variance $\sigma_\tau^2 \sim \mathrm{R}^{-(\mathrm{d}+1)}$ as $R \to +\infty$, which requires the coefficient A_τ of the leading term in the asymptotic expansion vanishes, i.e.,

$$\mathrm{A}_\tau = \lim_{||k||\to 0} \hat{\chi}(k) = 0 \tag{4.15}$$

In other words, for a hyperuniform material, its spectral density $\hat{\chi}$ goes to zero in the zero wave-vector limit. For statistically homogeneous and isotropic materials, the hyperuniform condition reduces to

$$\mathrm{A}_\tau = \lim_{||k||\to 0} \hat{\chi}(k) = \int_r [S_2(r) - \phi^2]\Omega_d(r)dr = 0 \tag{4.16}$$

where $\Omega_d(r)$ is the surface area of a sphere with radius r in *d* dimensions.

4.3 Generating realizations of hyperuniform materials using stochastic optimization

Generating realizations of heterogeneous materials from limited morphological information is a topic of great interest [23, 24, 25, 26, 27, 28, 29, 30, 31, 32, 33, 34, 35, 36, 37, 38, 39, 40, 41, 42]. Our procedure for reconstructing hyperuniform heterogeneous materials is developed within the Yeong-Torquato (YT) stochastic reconstruction framework, in which an initial random microstructure is evolved to minimize an energy function that measures the difference between the target correlation functions and the corresponding functions of the simulated microstructure.

In the YT procedure, the reconstruction problem is formulated as an ``energy'' minimization problem, with the energy functional E defined as follows

$$E = \sum_r \sum_\alpha [f_n^\alpha(r) - \widehat{f_n^\alpha}(r)]^2 \tag{4.17}$$

where $\widehat{f_n^\alpha}(r)$ is a target correlation function of type α and $f_n^\alpha(r)$ is the corresponding function associated with a trial microstructure. The simulated annealing method [43] is usually employed to solve

the aforementioned minimization problem. Specifically, starting from an initial trial microstructure (i.e., old microstructure) which contains a fixed number of pixels (voxels) for each phase consistent with the volume fraction of that phase, two randomly selected pixels (voxels) associated with different phases are exchanged to generate a new trial microstructure. Relevant correlation functions are sampled from the new trial microstructure and the associated energy is computed, which determines whether the new trial microstructure should be accepted or not via the probability:

$$p_{\mathrm{acc}} = \min\{\exp\left(-\frac{\Delta E}{T}\right), 1\} \tag{4.18}$$

where ΔE is the energy difference between the new and old trial microstructure and T is a virtual temperature that is chosen to be initially high and slowly decreases according to a cooling schedule. An appropriate cooling schedule reduces the chances that the system gets trapped in a shallow local energy minimum. In practice, a power law schedule $T(\mathrm{n}) = \alpha^{\mathrm{n}} T_0$ is usually employed, where T_0 is the initial temperature, n is the cooling stage and $\alpha \, \epsilon \, (0,1)$ is the cooling factor. The simulation is terminated when E is smaller than a prescribed tolerance (e.g., 10^{-8}). Generally, a large number of trial microstructures need to be searched to generate a successful reconstruction. Therefore, highly efficient sampling methods [23, 24, 25] are used that enable one to rapidly obtain the prescribed correlation functions of a new microstructure by updating the corresponding functions associated with the old microstructure, instead of completely re-computing the functions.

Here, we generalize the YT procedure by introducing an additional constraint for hyperuniformity and allowing one to constrain the given two-point correlation function only up to a certain cut-off distance γ for controlling the short-range order in the system. Specifically, the ``energy'' for the reconstruction now contains two terms, i.e.,

$$E = E_1 + E_2 \tag{4.19}$$

where E_1 and E_2 are respectively associated with the target correlation function $\widehat{S_2}$ and the hyperuniform constraint, i.e.,

$$E = \sum_{r=0}^{\gamma} [S_2(r) - \widehat{S_2}(r)]^2 \tag{4.20}$$

where γ in [0, L/2) (L is the linear system size) and

$$E_2 = |\sum_{r=0}^{L/2} [S_2(r) - \phi^2] \Omega_d(r)|^2 \tag{4.21}$$

where $\Omega_d(r)$ is surface area of a sphere with radius r in d dimensions. For $d = 2$, the main focus of this topic, $\Omega_2(r) = 2\pi r$.

We note that the ground state of the reconstruction requires $\mathrm{E}_1 = \mathrm{E}_2 = 0$. The summation in equation above is the discrete form of the integral, and thus, the condition $\mathrm{E}_2 = 0$ also implies $\mathrm{A}_\tau = 0$. In addition, we employ periodic boundary condition in the reconstructions and the largest distance in S_2 is given by half of the linear system size $\mathrm{L}/2$. However, the constraints imposed by $\mathrm{E}_1 = 0$ and $\mathrm{E}_2 = 0$ are not independent of one another. For example, for an arbitrary given S_2, there is no guarantee that the hyperuniform condition can be met. Therefore, we will only constrain S_2up to the cut-off distance γ to require the system possess a certain degree of short-range order specified by the short range values of S_2 and always require $\mathrm{E}_2 = 0$ to ensure hyperuniformity is achieved.

4.4 Microstructure of hyperuniform heterogeneous materials

4.4.1 Correlation functions for controlling short-range order

Two types of 2-point correlation functions are employed here to control the short-range order of the reconstructed hyperuniform materials, i.e., the exponential decay function $\mathrm{S}_2^{ED}$and the hard sphere function S_2^{HS}.It is also convenient to introduce the scaled autocovariance function, i.e.,

$$f(r) = (S_2(r) - \phi^2)/(\phi(1-\phi)) \tag{4.22}$$

where ϕ is the volume fraction of the phase of interest. Different from S_2, the scaled autocovariance function is independent of the reference phase and phase volume fraction, and characterizes the intrinsic spatial correlations in the material system.

The exponential decay function is given by

$$f^{ED} = \exp(-r/a) \tag{4.23}$$

where a is a characteristic correlation length of the material and we use $\mathrm{a} = 10$ pixels for the subsequent reconstructions. This monotonic decreasing correlation function, as shown in Fig. 4.1, is also referred to as the Debye random medium function [23], which corresponds to materials containing random clusters of arbitrary sizes and shapes. The hard sphere function f^{HS} does not possess an

analytical expression. Therefore, we compute f^{HS} from an ensemble of 2D hard sphere packings sampled from a Monte Carlo simulation of an equilibrium 2D hard sphere fluid [22]. As shown in Fig. 4,1, f^{HS} contains significant oscillations for small distances, indicating the spatial correlations among the spheres due to the non-overlapping constraint. The diameter of the sphere, which corresponds to the r value associated with first minimum of the oscillating function, is $\mathrm{D} = 10$ pixels. For the subsequent reconstructions, we will consider two values of volume fraction, $\phi = 0.3$ and $\phi = 0.5$, which are respectively below and above the percolation threshold for the corresponding materials. The two-point function $S_2(r)$ can be readily obtained from the corresponding $f(r)$.

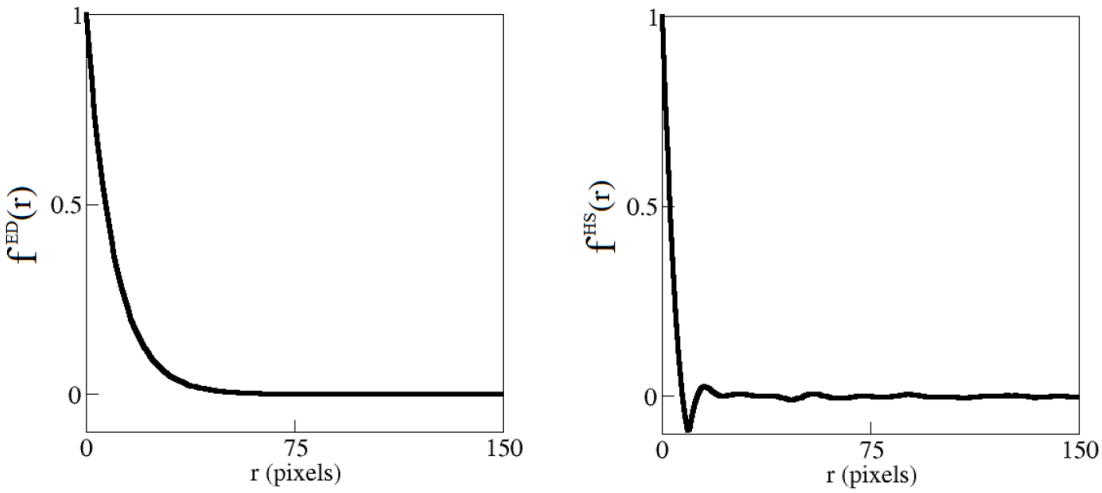

Fig. 4.1 Correlation functions employed to control the short-range order in the reconstructed hyperuniform materials. Left panel: The exponential decay function f^{ED}. Right panel: The hard sphere function f^{HS}.

The choice of aforementioned correlation functions is inspired by Refs. [44, 45]. Specifically, since the exponential function $f^{ED}(r)$ is always positive, it is not possible for hyperuniform equation to hold for this function (i.e., the integral is always greater than zero for all volume fractions). This implies that the short-range order imposed by $f^{ED}(r)$ will be competing with the global hidden order imposed by the hyperuniformity constraint, and hyperuniformity is successively more difficult to achieve as the

constraint cut-off distance γ increases. On the other hand, the oscillating hard sphere function $f^{HS}(r)$ is more compatible with the hyperuniform condition, suggesting that it is easier to achieve hyperuniformity in system with such $f^{HS}(r)$. As we will show in Sec. IV, the reconstructed hyperunfiorm materials associated with these two different correlation functions can possess distinct properties compared to their non-hyperuniform counterparts.

4.4.2 Realizations of hyperuniform materials

The realizations of hyperuniform materials with a linear size of 300 pixels associated with the aforementioned correlation functions $f^{ED}(r)$ and $f^{HS}(r)$ with increasing constraint distance $\gamma = 5,10,15,25,50,80,100$ and 120 pixels as well as their non-hyperuniform counterparts are generated using the generalized stochastic reconstruction procedure described in Sec. III. For all of the reconstructions, we require that the final energy $\mathrm{E} < 10^{-8}$. In the case of hyperuniform materials, this implies that the hyperuniform constraint $\mathrm{E}_2 < 10^{-8}$ and the degree of hyperuniformity is also independently verified by directly computing the local volume fraction fluctuations as a function of observation window size.

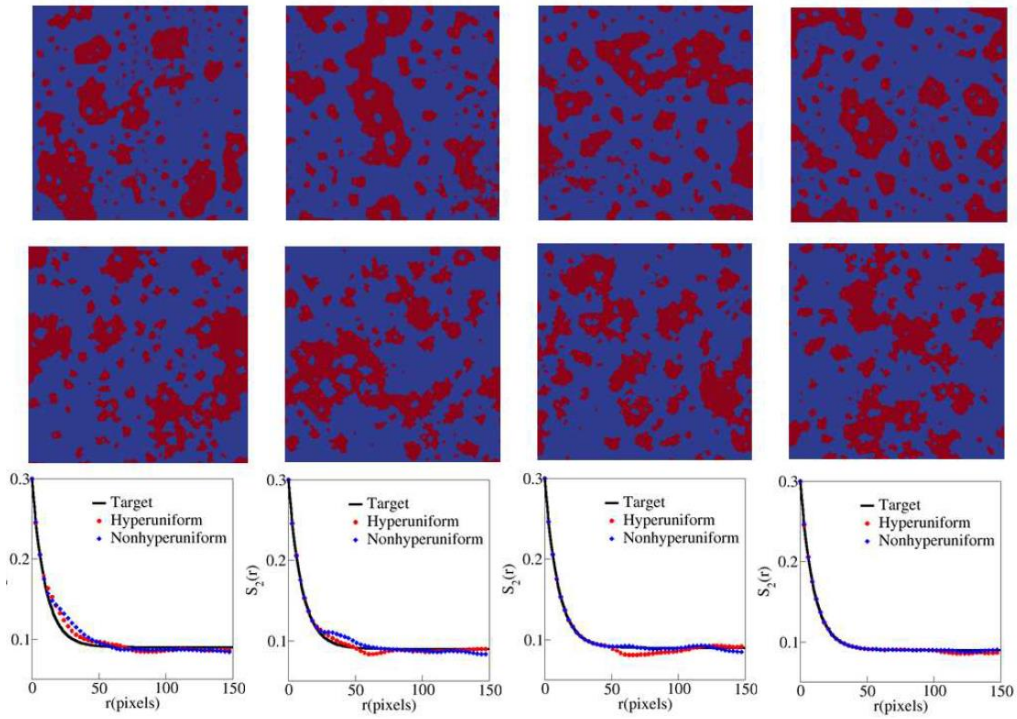

Fig. 4.2 Realizations of the hyperuniform materials (upper panels) and the corresponding non-hyperuniform materials (middle panels) associated with the exponential decay function f^{ED} for different constraint cut-off distances γ with φ = 0.3 for the inclusion phase. The associated target and reconstructed correlation functions are shown in the lower panels. The constraint distances γ from left to right are 15, 25,50 and 100 pixels.

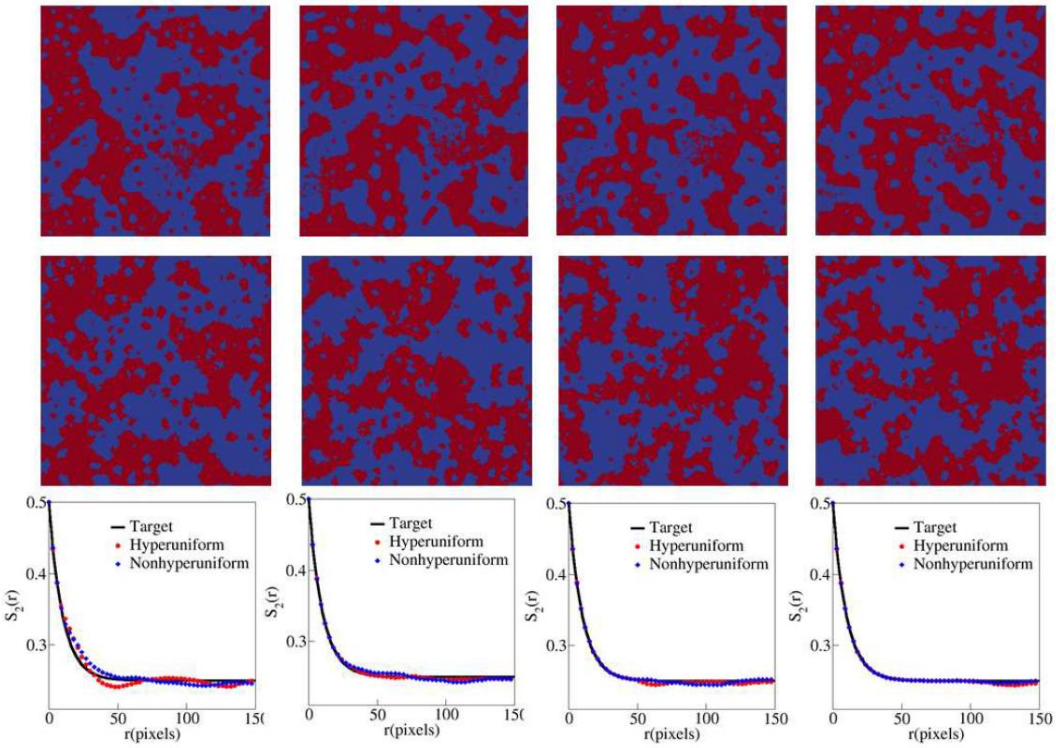

Fig. 4.3 Realizations of the hyperuniform materials (upper panels) and the corresponding non-hyperuniform materials (middle panels) associated with the exponential decay function f^{ED} for different constraint cut-off distances γ with φ = 0.5 for the inclusion phase. The associated target and reconstructed correlation functions are shown in the lower panels. The constraint distances γ from left to right are 15, 25,50 and 100 pixels.

Figures 4.2 and 4.3 respectively show the reconstructed microstructures associated with $f^{ED}(r)$ at volume fractions $\phi = 0.3$ and 0.5 for selected γ values (i.e., 15, 25, 50 and 100 pixels). For all γ values, the constraint is satisfied to a high degree for the hyperuniform systems with $\mathrm{E}_2 \sim 10^{-8}$,in contrast to the large $\mathrm{E}_2 \sim 10^{2}$ for the non-hyperuniform systems. It can be seen that for both ϕ values, the reconstructed microstructures contain ``clusters of arbitrary sizes and shapes'', which is a well-known structural feature of the so called Debye random media [23] associated with the exponential decay S_2. Also shown are the target and reconstructed correlation functions for different constraint cut-off distance γ.

In the case of $\phi = 0.3$, it can be clearly seen that for small γ values (i.e., 15 and 25 pixels), the reconstructed correlation functions for both the hyperuniform and non-hyperuniform cases deviate significantly from the corresponding target functions. Specifically, the reconstructed S_2 values for r immediately beyond γ are significantly larger than the corresponding values of the target function, indicating the existence of clusters with characteristic sizes comparable to such r values. For intermediate γ values (e.g., 50 pixels), the reconstructed S_2 for the non-hyperuniform case well matches the target function even for r values beyond the constrained distance. However, for the hyperuniform case, the reconstructed S_2 starts to exhibit a significant decay immediately beyond γ, indicating a strong suppression of the spatial correlations on such length scales. We note that this behavior is necessary to achieve the hyperuniformity imposed by the constraint. For large γ values (e.g., 100 pixels), the reconstructed S_2 for both the hyperuniform and non-hyperuniform cases match the target function well. However, a closer inspection reveals that the hyperuniform S_2 still exhibits weak yet non-vanishing oscillations beyond the constrained distance. Again, these oscillations are required by the hyperuniform constraint.

The behaviors of the reconstructed systems with $\phi = 0.5$ for both hyperuniform and non-hyperuniform cases as γ increases are very similar to the corresponding systems with $\phi = 0.3$. However, the relative deviation of the reconstructed functions from the target function for a specific γ value is much smaller in systems with $\phi = 0.5$ and the systems contain almost percolating clusters of the inclusion phase. We note that for both $\phi = 0.3$ and 0.5, the reconstructed hyperuniform systems and their non-hyperuniform counterparts are almost visually indistinguishable in a statistical sense. This is because by construction these systems possess the same short- and even intermediate-range spatial correlations. Yet the two types of systems possess distinctly different structural characteristics on large length scales as indicated by the distinct E_2 values.

Figures 4.4 and 4.5 respectively show the reconstructed systems associated with $f^{HS}(r)$ at volume fractions $\phi = 0.3$ and 0.5 for selected γ values (i.e., 15, 25, 50 and 100 pixels). In the reconstructed hyperuniform systems, the constraint is satisfied to a high degree for all γ values with $E_2 \sim 10^{-8}$. Interestingly, the non-hyperuniform systems associated with the hard-sphere function $f^{HS}(r)$

possess a much smaller $\mathrm{E}_2 \sim 10^{-3}$compared to that for non-hyperuniform systems associated with the exponential function $f^{ED}(r)$, although this value is still much larger than that for the hyperuniform systems. As we discussed in Sec. IV.A, the oscillatory feature of $f^{HS}(r)$makes it naturally possess a smaller E_2. In addition, the target$f^{HS}(r)$ is associated with the equilibrium hard sphere system, which is already in a state close to hyperuniformity [17].

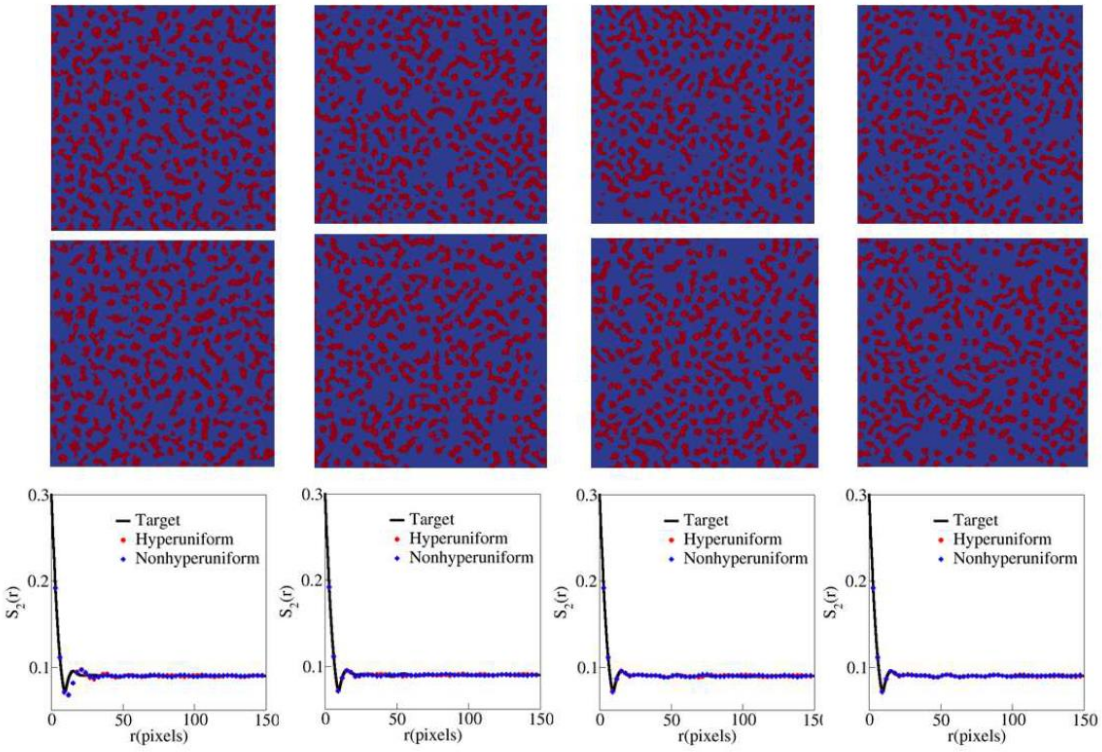

Fig. 4.4 : Realizations of the hyperuniform materials (upper panels) and the corresponding non-hyperuniform materials (middle panels) associated with the hard sphere function f^{HS} for different constraint cut-off distances γ with φ = 0.3 for the inclusion phase. The associated target and reconstructed correlation functions are shown in the lower panels. The constraint distances γ from left to right are 15, 25, 50 and 100 pixels.

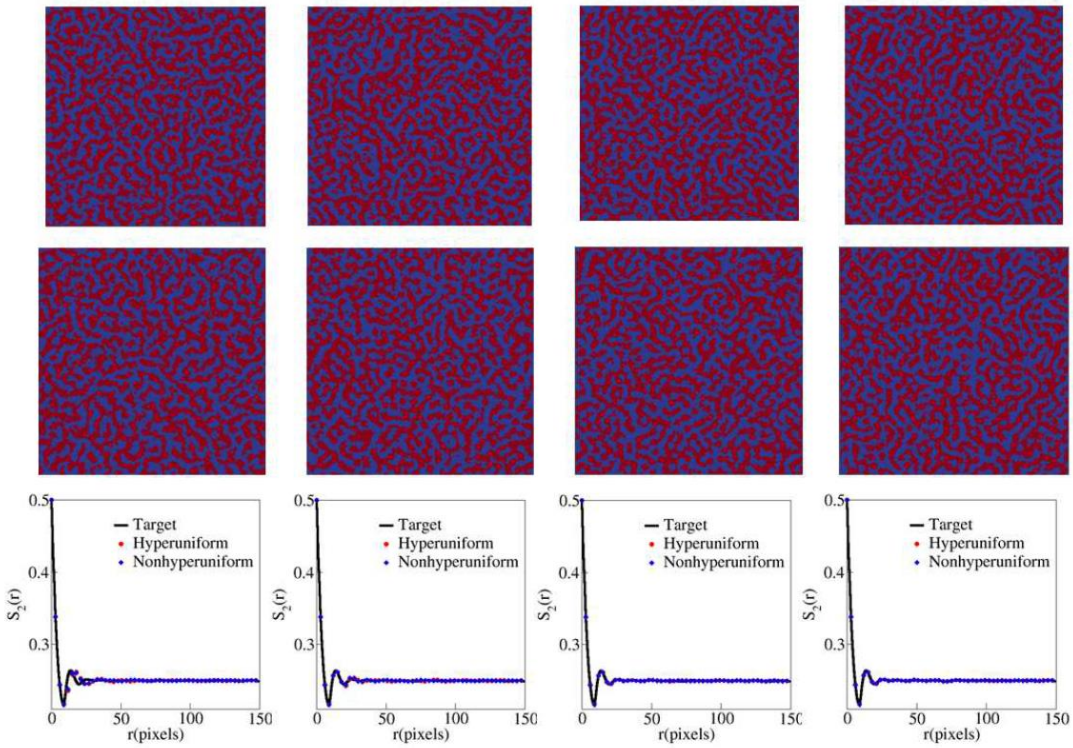

Fig. 4.5 Realizations of the hyperuniform materials (upper panels) and the corresponding non-hyperuniform materials (middle panels) associated with the hard sphere function f^{HS} for different constraint cut-off distances γ with φ = 0.5 for the inclusion phase. The associated target and reconstructed correlation functions are shown in the lower panels. The constraint distances γ from left to right are 15, 25, 50 and 100 pixels.

For $\phi = 0.3$, the reconstructed microstructures contain statistically homogeneous dispersions of compact clusters (i.e. ``hard particles'') with relatively small aspect ratios. It has been shown that the original spherical particles cannot be perfectly reproduced in the reconstructions using S_2 alone since critical topologically connectedness information of the system is missing. Specifically, the elongated particles in the reconstructions correspond to local clustering configurations of non-overlapping spheres in the original system. For $\phi = 0.5$, the strong local spatial correlations manifested as the strong oscillations in the target function are realized by the interconnected stripe-like local structures with well-defined characteristic width λ that resemble those in a typical Eutectic microstructure. A closer

inspection reveals that $\lambda = \mathrm{D}$, where D is the distance associated with the first local minimum in $f^{HS}(r)$, roughly corresponding to the diameter of the spheres in the original system.

Different from the systems associated with the exponential decay function, neither the reconstructed correlation functions nor the realizations significantly vary as the constraint distance γ increases in the current systems for both $\phi = 0.3$ and 0.5. We note that the oscillations in the hard sphere function $f^{HS}(r)$ stems from the strong short-range correlations in the original hard sphere system due to the hard-core repulsion between the particles. A direct manifestation of the hard-core repulsion in $f^{HS}(r)$ is the deep first local minimum (valley) and the first local maximum (peak), which respectively corresponds to the size of the hard spheres (i.e., exclusion shell) and the size of the nearest neighbor shell. Once these two crucial short-range correlations are set, the remaining intermediate-range correlations (i.e., oscillations) are also determined. In our reconstructions, even the smallest cut-off distance $\lambda = 15$ pixels constrains the correlation function beyond the first valley at $r \approx \mathrm{D} = 10$ pixels. This only leaves very limited room for the system to further adjust the intermediate and long range correlations, leading to small deviations of the reconstructed correlation functions from the target. For other cut-off values (i.e., $\gamma \geq 25$ pixels), both the first valley and peak are constrained and thus, the system has virtually no freedom to adjust the longer range correlations beyond the constrained distance. This leads to the good agreement of the reconstructed and target correlation functions for all distances beyond the constraint cut-off γ.

In addition, the reconstructed hyperuniform systems for both volume fractions are visually indistinguishable from the corresponding non-hyperuniform systems in a statistical sense. This is again because by construction these systems possess the same short- and intermediate-range spatial correlations, which are most sensitive to eyeball tests. On the other hand, the large scale structural characteristics are more difficult to be picked up via visual inspection. We note that in this case, the distinction between the hyperuniform and non-hyperuniform systems on large length scales is less dramatic than in the systems associated with the exponential decay function. This also leads to a less dramatic difference in the mechanical properties of the hyperuniform and corresponding non-hyperuniform systems as shown in Sec. V.

4.5 Superior mechanical properties of hyperuniform heterogeneous materials

4.5.1 Lattice-particle method for micromechanical analysis

The elastic and fracture behaviors of the generated hyperuniform heterogeneous materials are analyzed using the volume-compensated lattice-particle method (LPM) [46, 47]. In the LPM, the continuum is treated as an ordered network of interacting material points (consistent with the reconstruction grid), which obeys a cohesive law directly obtained from basic constitutive relationships with analytical solutions. The interactions among the material points include both local pair-wise potential between two particles $\mathrm{U_{pair}}$ and a multi-body potential among non-local particles $\mathrm{U_V}$, i.e., $\mathrm{U = U_{pair} + U_V}$. Accordingly, the force field between two neighboring particles only depends on their relative displacements (i.e., pair-wise potential), but also includes a contribution from all the neighboring particles surrounding them (i.e., non-local multi-body potential). The unique advantage of the LPM formulation is that material fracture can be naturally simulated by breaking the bonds between material points based on critical bond length or force. The LPM has been successfully applied to study the mechanical performance of a variety of heterogeneous material systems [48, 49, 50]. Interested readers are referred to Refs. [46, 47] for details of this method.

4.5.2 Elastic behavior

We now apply the LPM to study the mechanical properties of the reconstructed hyperuniform materials. Specifically, we consider the inclusion phase serves as the reinforcement for the matrix, and both phases are isotropic. The Young's modulus and Poisson's ratio for the inclusion and matrix phase are respectively $\mathrm{E_I} = 100$ GPa, $\mu_\mathrm{I} = 0.33$ and $\mathrm{E_M} = 10$ GPa, $\mu_\mathrm{M} = 0.32$. We note that the exact values of the mechanical properties of individual phases do not affect the conclusions of our study, yet the contrast between the Young's moduli of the inclusion and matrix phases does affect the degree of contrast between the effective moduli of the hyperuniform and the corresponding non-hyperuniform materials. A uniaxial load is applied to the top and bottom boundary of the square representative volume

element (RVE) reconstructed in Sec. IV, which leads to an overall axial elastic strain $\epsilon = 0.002$. The remaining two boundaries of the RVE are force free. In the subsequent LPM simulations, we will focus on the systems with $\phi = 0.3$ for which the inclusion phase forms a dispersion of compact clusters and particles, in contrast to the nearly percolating morphology of the inclusion phase for the systems with $\phi = 0.5$. Thus, we expect to observe more significant contrast between the mechanical behaviors of the hyperuniform and non-hyperuniform systems with $\phi = 0.3$.

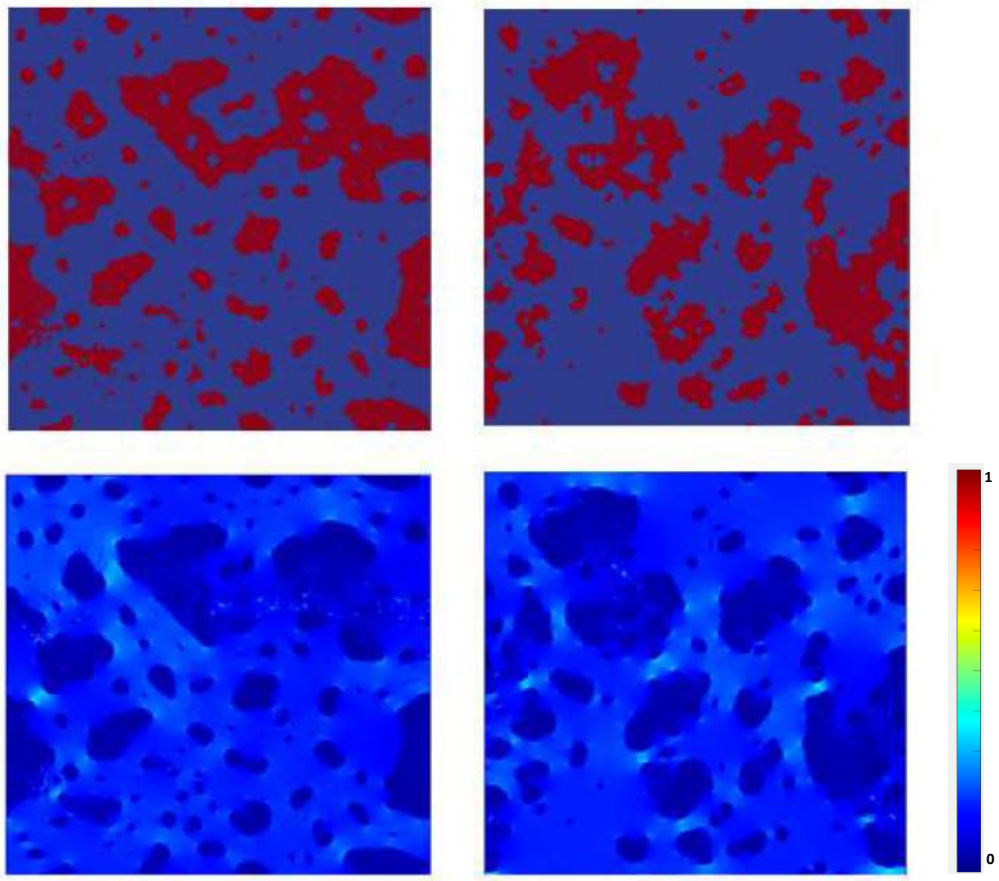

Fig. 4.6 Microstructure and corresponding normalized elastic strain energy density distribution $\Omega(x)$ in a hyperuniform material (left panels) associated with the exponential decay function (with γ = 50) and its non-hyperuniform counterpart (right panels).

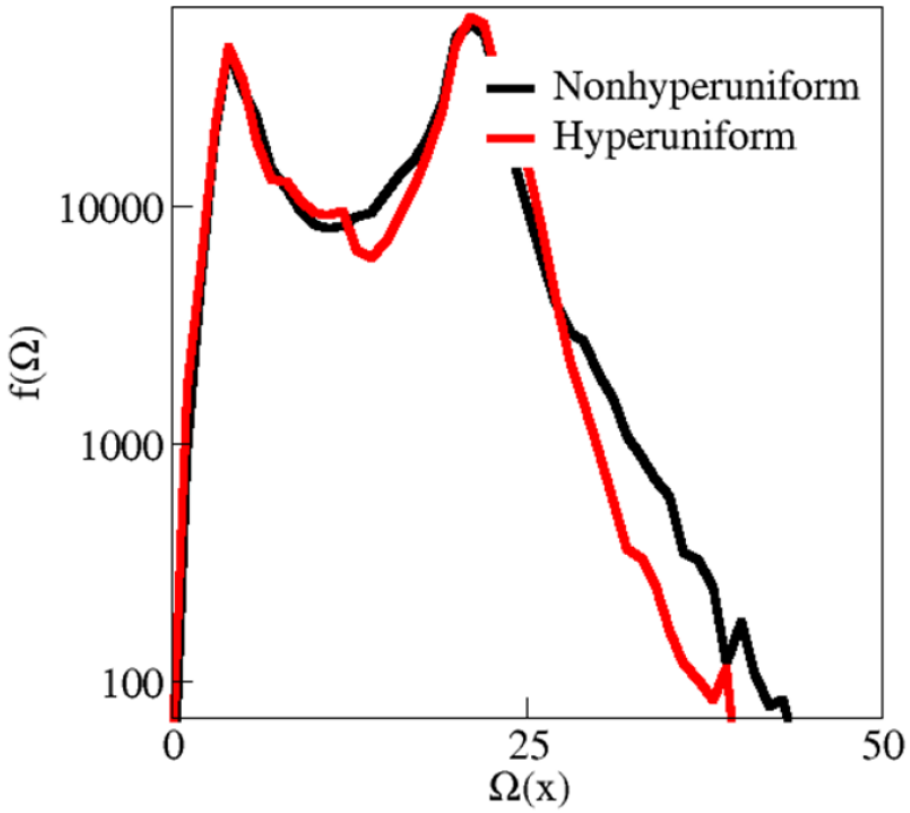

Fig. 4.7 Statistics of the strain energy density distribution $f(\Omega)$ in the hyperuniform system (left) and non-hyperuniform system (right).

Figure 4.6 shows an example of the elastic strain energy density distribution $\Omega(\mathrm{x})$ in a hyperuniform material associated with the exponential decay function (with $\gamma = 50$) and its non-hyperuniform counterpart. Figure 4.7 shows the associated statistics of the strain energy density distribution $f(\Omega)$ in both systems. It can be seen that the high strain energy densities usually occur in regions with a high degree of clustering of the inclusion phases in both systems. In addition, the quantitative statistics indicate that the non-hyperuniform system possesses a significantly larger population of high strain energy density values compared to its hyperuniform counterpart, which would be due to the distinct large-scale structural characteristics of the two systems.

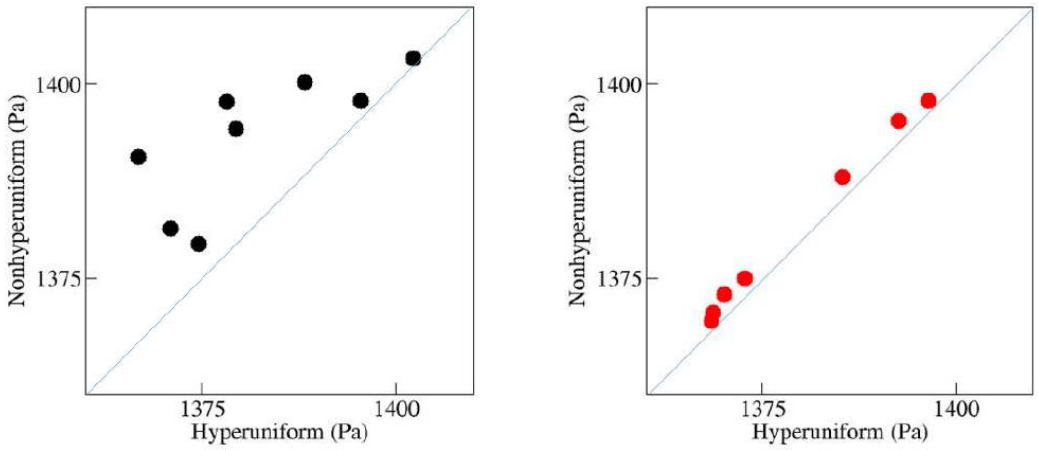

Fig. 4.8 Averaged elastic strain energy density $\bar{\Omega}$ in the reconstructed materials associated with the exponential decay function $f^{ED}(r)$ (left panel) and the hard sphere function $f^{HS}(r)$ (right panel) for different γ values.

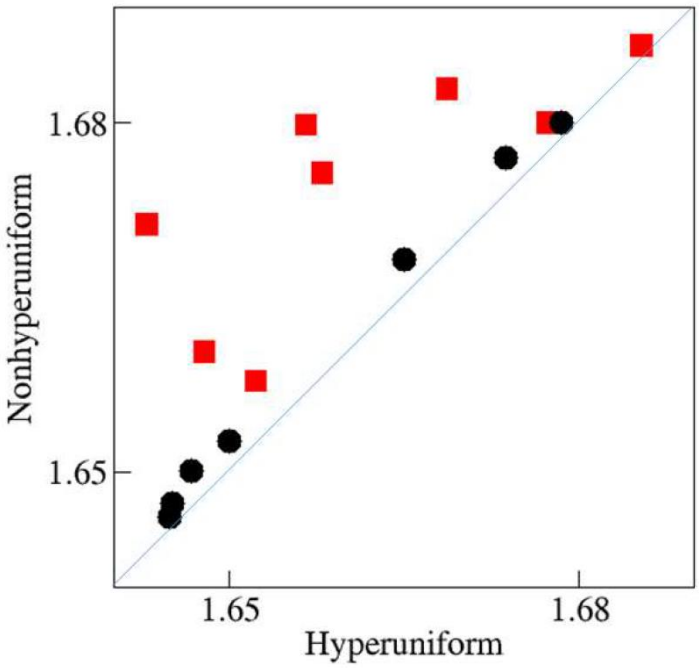

Fig. 4.9 Normalized effective Young's modulus $\bar{E}/E_M$ of the reconstructed heterogeneous materials associated with the exponential decay function $f^{ED}(r)$ (red square) and the hard sphere function $f^{HS}(r)$ (black circle) for different γ values.

Figure 4.8 shows the averaged local strain energy density $\overline{\Omega}$ defined as

$$\overline{\Omega} = \frac{1}{\mathrm{V}} \int \Omega(x) dx \tag{4.24}$$

where V is the volume of the system, for systems associated with both the hard sphere function $f^{HS}(r)$ and the exponential decay function $f^{ED}(r)$ for different cut-off distances γ. It can be seen that for both correlation functions, the non-hyperuniform systems generally possess a larger $\overline{\Omega}$ compared to the corresponding hyperuniform systems, which would mainly due to the excessive number of high Ω states in the former. Figure 4.9 shows the normalized effective Young's modulus $\bar{E}/E_M$ of the reconstructed heterogeneous materials, i.e., $\bar{E} = \bar{\sigma}/\epsilon$, where $\bar{\sigma}$ is the average tensile stress in the system and ϵ is the applied tensile strain. Consistent with the trends in $\overline{\Omega}$, we see again that the non-hyperuniform systems generally possess a higher $\bar{E}$ compared to the corresponding hyperuniform systems. A possible reason for the observed smaller $\overline{\Omega}$ and $\bar{E}$ in hyperuniform systems is the higher degree of uniformity in the distribution of clusters on large length scales. This would effectively lead to a lower degree of stress concentration in such systems and thus, an overall lower elastic energy and smaller modulus.

It is interesting to note that the contrast between $\bar{E}$ of the hyperuniform and non-hyperuniform systems associated with the exponential decay function $f^{ED}(r)$ is significantly stronger than that for systems associated with the hard sphere function $f^{HS}(r)$. As discussed in Sec. IV, due to the nature of $f^{HS}(r)$ and the associated original equilibrium hard sphere system that is close to hyperuniformity, the structural distinctions between the hyperuniform and non-hyperuniform systems associated with $f^{HS}(r)$ are much smaller on both small and large length scales. This has led to a weaker contrast between $\overline{\Omega}$ of the hyperuniform and non-hyperuniform systems and thus, a weaker contrast between $\bar{E}$.

4.5.3 Brittle fracture analysis

We now study the brittle fracture behavior of the reconstructed systems. As briefly discussed in chapter 4.5.2, in the LPM the continuum is modeled as a regular array of material points interacting with near neighbors and thus, fracture is naturally captured via breaking of bonds between the material points. The same Young's modulus and Poisson's ratio for the inclusion and matrix phases as in Sec. V.B are also used here. In addition, the critical stress for bond breaking is set to be $\sigma_c = 950$ MPa. We note

that similar to the elastic analysis, although the exact value of the fracture strength σ_f depends on the choice of σ_c, the conclusions drawn here are not affected by σ_c. A uniaxial load is applied to the square RVE of the reconstructed materials under the quasi-static loading condition, with a strain rate $d\epsilon/dt = 10^{-7}$per loading step and a total of $N = 40{,}000$ loading steps are used. After each loading step, the stress and strain distributions in the RVE are computed and each bond is checked for possible breaking. If the stress in a bond is greater than the critical stress σ_c, this bond (i.e., the connection between two materials points) is removed from the system, which corresponds to the nucleation of a micro-void. This will lead to a significant change of the stresss/strain distributions in the next loading step. The reaction force F (and the uniaxial tensile stress) is computed at each loading step. The material is consider to fail when a abrupt drop is observed in F. The fracture strength is then computed from the maximum reaction force, i.e., $\sigma_f = F_{max}/A$, where A is the cross-sectional area of the RVE.

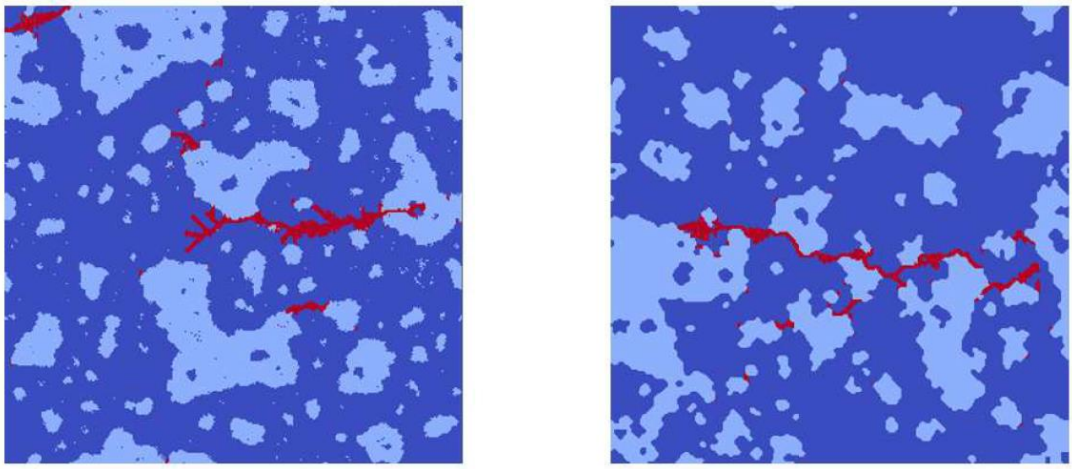

Fig. 4.10 Growing cracks in the reconstructed hyperuniform material (left) and its non-hyperuniform counterpart (right) associated with $f^{ED}(r)$ and γ = 50 pixels generated using LPM simulations.

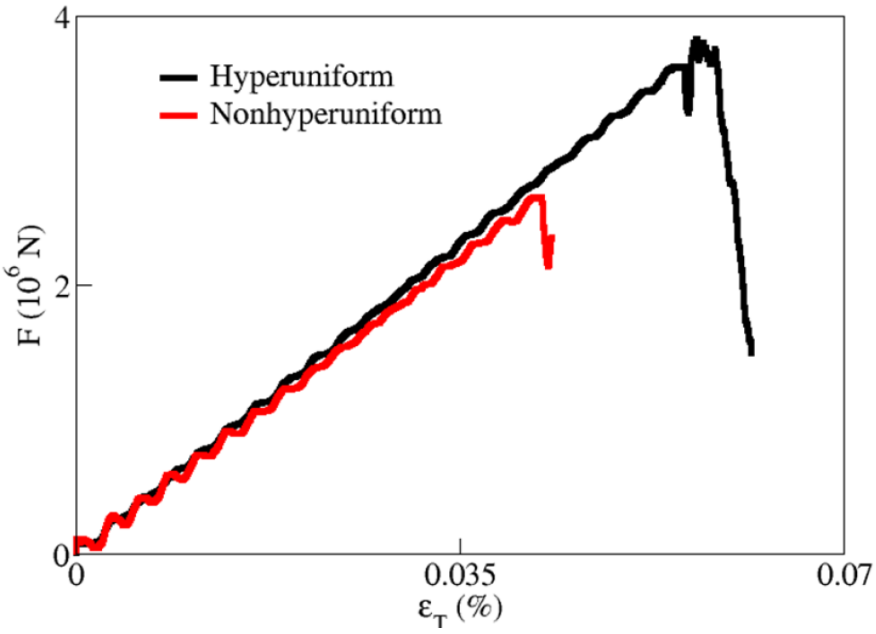

Fig. 4.11Reaction forces as a function of tensile strain ϵ_T in the two materials shown in Fig. 4.10 under quasi-static uniaxial loading condition.

Figure 4.10 shows an example of our brittle fracture simulations of the reconstructed hyperuniform material and its non-hyperuniform counterpart associated with $f^{ED}(r)$ and $\gamma = 50$ pixels. The corresponding reaction forces as a function of tensile strain ϵ_T is shown in Fig. 4.11, which is overall an increasing function of ϵ_T. We note that the small oscillations in the $F - \epsilon_T$, which are due to dynamic method for solving the LPM equations and will vanish in the limit of zero strain rate, do not affect the calculation of the fracture strength. It can be clearly seen in Fig. 4.11 that the hyperuniform material possesses a much higher maximal reaction force F_{max} and thus, a higher fracture strength σ_f than the corresponding non-hyperuniform material.

The same analysis is applied to all systems with $\phi = 0.3$ reconstructed in Sec. IV, and the obtained fracture strengths of the hyperuniform materials vs. the corresponding non-hyperuniform materials are shown in Fig. 4.12. We can see that for the systems associated with the exponential decay function $f^{ED}(r)$, the hyperuniform systems generally possess a higher fracture strength σ_f than the corresponding non-hyperuniform systems. Specifically, σ_f of the hyperuniform materials can be larger

than that for the corresponding non-hyperuniform materials by as large as 20%. However, for systems with the hard sphere function $f^{HS}(r)$, the hyperuniform systems possess similar and even slightly smaller σ_f compared to their corresponding non-hyperuniform counterparts. We note that this observation is also consistent with the trend observed in the effective Young's modulus, i.e., the contrast between the hyperuniform and non-hyperuniform systems associated with the exponential decay function is generally larger than that for systems associated with the hard sphere function. This again is attributed to the smaller structural distinctions between the hyperuniform and non-hyperuniform systems associated with $f^{HS}(r)$ on both small and large length scales.

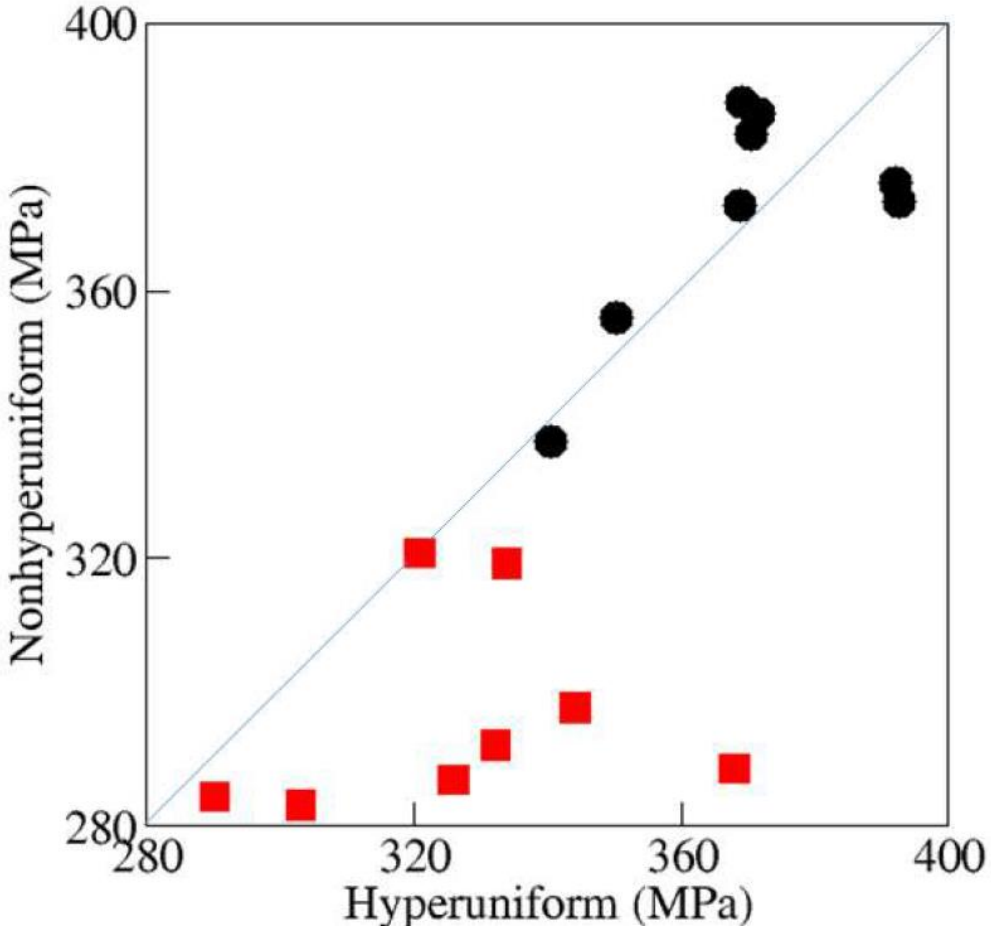

Fig. 4.12 Fracture strengths of the hyperuniform materials vs. the corresponding non-hyperuniform materials associated with the exponential decay function $f^{ED}(r)$ (red square) and the hard sphere function $f^{HS}(r)$ (black circle).

To understand why hyperuniform materials generally possess superior fracture behavior, we further examine the mechanisms for the nucleation and growth of the cracks in the reconstructed systems. Specifically, due to the larger population of local high strain energy states in the non-hyperuniform materials, it is expected that a larger number of cracks are nucleated in such systems compared to their hyperuniform counterparts at the same loading level. This is evident from Fig. 4.10, which shows the distribution of cracks before the overall material failure occurs. It can be seen that the hyperuniform material contains a single major crack in the matrix phase, which indicates the failure is mainly due to the continuous growth of individual dominant cracks in the system. In contrast, the non-hyperuniform material contains a large number of smaller cracks, which start to connect to one another and form a percolating large crack across the entire system. Therefore, the major failure mechanism in the non-hyperuniform materials is the fast growth and percolation of many small cracks, which under the same loading condition leads to a lower fracture strength than that of the corresponding hyperuniform materials.

4.6 Conclusions and discussions

In this chapter, we have employed a stochastic optimization procedure to systematically generate realizations of hyperuniform heterogeneous materials associated with two distinct two-point correlation functions, i.e., the exponential decay function $f^{ED}(r)$ and the hard sphere function $f^{HS}(r)$, which control the short-range order in the reconstructed materials. For purpose of comparison, corresponding non-hyperuniform materials possessing the same short-range order have also been reconstructed and analyzed. We found that the short-range correlations imposed by the oscillating hard sphere function $f^{HS}(r)$ are compatible with the constraint on large-scale local volume fraction fluctuations and thus, hyperuniformity is more easily achieved in the systems associated with $f^{HS}(r)$. On the other hand, the monotonic decaying function $f^{ED}(r)$ is not automatically compatible with the hyperuniform constraint and the reconstructed hyperuniform and non-hyperuniform materials associated with this function possess distinct structural characteristics on large length scales.

In addition, we have investigated the mechanical performance of the reconstructed hyperuniform materials and their non-hyperuniform counterparts including both elastic and failure behaviors using the LPM simulations. We found that the hyperuniform materials generally possess a smaller Young's modulus than their non-hyperuniform counterparts. However, the hyperuniform materials are found to be more resistant to brittle fracture, with a significantly higher fracture strength compared to the corresponding non-hyperuniform materials. This superior mechanical behavior is attributed to the lower degree of stress concentration in the material resulting from the hyperuniform microstructure, which results in different failure mechanisms in different systems. Although we have focused on 2D systems, we expect that the conclusions drawn here also hold for 3D hyperuniform materials, as the general mechanisms for observed mechanical performance do not depend on spatial dimensions.

Designing heterogeneous materials with superior mechanical properties especially failure resistance is a topic of great interest. Our study here suggests a possible avenue to achieving this goal, i.e., by imposing hyperuniformity in the system. The realizations of the hyperuniform materials can be easily fabricated using 3D printing. It is also interesting to see whether existing materials with a high fracture resistance such as certain natural and synthesized composites would possess a nearly hyperuniform microstructure.

5. COLLECTIVE CELLULAR DYNAMICS IN ECM

5.1 Introduction

Collective cellular dynamics in three-dimensional extracellular matrix (ECM) plays a central role in many physiological processes including morphogenesis, wound healing and particularly tumor metastasis[51-53]. These processes, such as the formation of tubular structures during the development of branched organs [54], the repair of epithelial wounds [55, 56] and the growth of vessels during tumor angiogenesis [57], involve highly orchestrated multicellular dynamics over large spatial and temporal scales. Quantitative measurement of these length and time scales provides key information that allows us to distinguish individual from emergent multicellular cellular behaviors.

Coordination between cells requires efficient cell–cell communications in the forms of chemical [58], electrical [59] or mechanical signals [60, 61]. The need to overcome physical barriers during 3D migration [62] and the excellent force transmission within the ECM [63, 64] strongly suggest a role for mechanical cues in orchestrating collective cancer invasion.

The mechanical interaction between cells involves force generation, propagation and sensation. The three steps do not occur in sequence but rather are coupled dynamically to maintain tissue homeostasis [65]. In particular, traction force from one cell will remodel the local geometry and elasticity of the ECM [66] therefore modulating the force generation of nearby cells [67]. The presence of direct or ECM-mediated intercellular feedback mechanisms has suggested the notion of collective force generation, especially in the context of tumor metastasis [68]. Indeed, it has been observed that tumor organoids exert highly organized traction forces [69], while isolated individual cells generate fluctuating forces that vary significantly from one cell to another [70].

To further investigate collective force generation during cancer cell migration, here we present a phenomenological model in FIG. 5.1 based on the recently developed tumor diskoid in geometrically micropatterned ECM (DIGME) system which is a mechanical-based strategy that allows easy engineering of the shape of 3D tissue organoid, the mesoscale ECM heterogeneity, and the fiber alignment of collagen-based ECM all at the same time by only setup a dish-like cell-collagen solution within three-dimensional ECM [71]. In our model, cell–cell communication is characterized by a single

parameter that quantifies the correlation length of cellular migration cycles. Specifically, we consider that each tumor cell undergoes a series of periodic contraction cycles from its migration machinery. For simplicity, the contraction cycles of all of the cells are considered to possess the same periodicity. Each cell is also characterized by a unique contraction phase, which is spatially correlated with that of other cells via an inverse exponential function with the correlation length a (i.e. exp(-r/a)). We devise a stochastic reconstruction method to generate realizations of contracting cell colonies with specific phase correlation functions and correlation length a. The deformation field resulting from collective cell contraction with different a values is then computed and quantitatively compared with the experimentally measured deformation field in the breast cancer DIGME system in order to identify the correlation length a for the system.

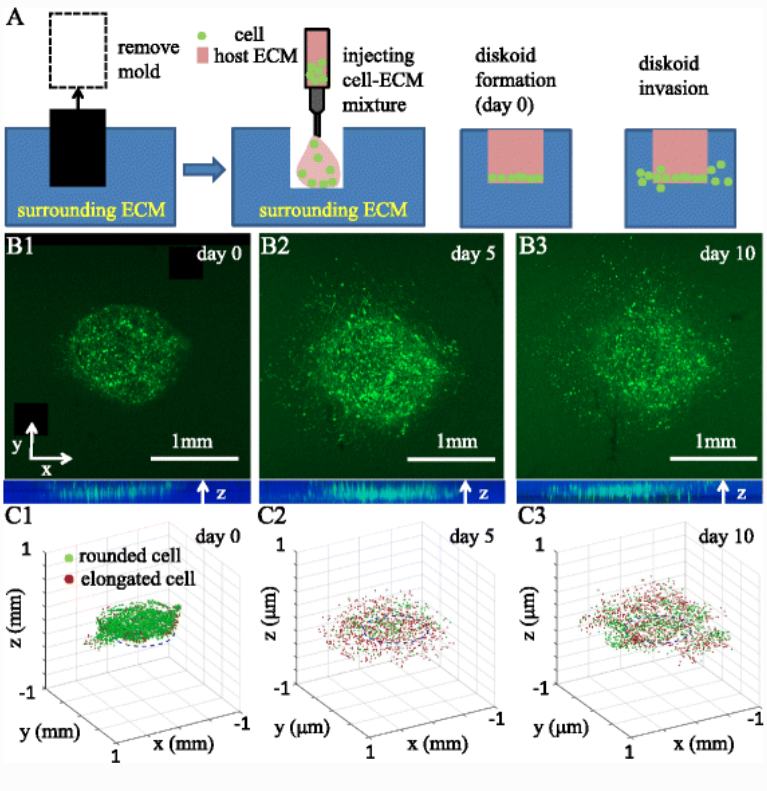

Fig. 5.1 Preparation and collective migration of a circular DIGME. A Schematics showing the steps of forming a DIGME device. B1-B3 Top views of a diskoid in 3D ECM. C1-C3Manually identified 3D cell centers and morphological phenotypes corresponding to B1-B3

Our study shows that as the correlation length increases from 0 (i.e. the case where the cell contractions are completely random), the size of the region of cells with similar contraction phases also increases. In the limit $a \rightarrow \infty$, the entire cell colony is completely synchronized and all cells contract simultaneously. For small a values, the large fluctuations in individual cell contraction phases smooth out the temporal fluctuations in the time-dependent deformation field in the ECM. On the other hand, for large a values, the periodicity of individual cell contraction cycles is clearly manifested in the temporal variation of the overall deformation field in the ECM. This generic dependence of temporal variation of the deformation field on a is utilized to identify the correlation length in DIGME. Through quantitative comparisons of the simulation results and experimental data, we find that the correlation length for collective force generation in the breast cancer DIGME system is $a \approx 25\,\mu\mathrm{m}$, which is roughly twice the linear size of a single cell. One possible mechanism for this intermediate cell correlation length is fiber-mediated stress propagation in the 3D ECM network in DIGME [64].

5.2 Methods

5.2.1 Cell culture and 3D patterning

First, we need to thank A.Alobaidi and B.Sun, etc., for efforts in the experimental part. High-concentration type I rat tail collagen (9.95 mg m −l 1 ,Corning) was diluted with Dulbecco's modified Eagle's medium, phosphate-buffered saline (PBS, 10×) and sodium hydroxide (NaOH, 0.1M) to a concentration of $2\mathrm{mgml}^{-1}$ with pH 7.4. All solutions were held and mixed at 4 °C, prior to the gelation process at 37 °C. To create 3D patterned cell disks, we employed the DIGME method described previously [71]. Briefly, a stainless-steel cylinder was used to mold a well in the collagen gel. Then high-density human breast carcinoma cells (MDA-MB-231/GFP, Cell Biolabs) were mixed with neutralized collagen solution and used to fill the molded well. The sample was placed in a tissue culture incubator at 37 °C with 5% CO_2 for 3 h then moved to an on-stage incubator for imaging.

5.2.2 Micromechanical model for tumor DIGME

Here we develop a 2D micromechanical model for the tumor DIGME. Specifically, the ECM is modeled as a nonlinear elastic continuum with strain hardening behavior and elastic moduli $\mathrm{K} = 150\ \mathrm{Pa}$ (bulk modulus) and $\mu = 100\ \mathrm{Pa}$ (shear modulus) [72], which has been shown to correctly capture the mechanical behavior of ECM. As we will show below, the exact values of the elastic moduli do not affect the determination of the cell correlation length in the system. In addition, we note although a collagen network generally exhibits viscous behavior we believe it is legitimate to model it as a nonlinear elastic medium in the current work. This is because the characteristic periodicity for cellular contraction (~220 min) in our DIGME system is generally much larger than the relaxation time scale for the viscous behavior of collagen gels (~30s).

The cells, which are embedded in the ECM, are modeled as equal-sized 2D circular disks. Initially, a fixed number of non-overlapping disks are randomly placed in a square simulation domain with periodic boundary conditions. The disk packing is subsequently densified by repeatedly shrinking the size of the simulation domain while randomly displacing the disks via the Monte Carlo method. Once a desirable cell packing density has been achieved, a circular region representing the tumor diskoid is 'cut out' from the resulting packing configuration and embedded in the middle region of the ECM. In our simulations, the diskoid contains ~1000 cells with a covering fraction of ~0.55, consistent with the experimentally measured cell density.

Once the geometrical model for DIGME has been established, the volume-compensated lattice-particle method (VCLP) [49] is employed to study the mechanical behavior of DIGME due to cell contraction. In the VCLP, the continuum is treated as an ordered network of interacting material points, which obeys a cohesive law directly obtained from basic constitutive relationships with analytical solutions. The interactions among the material points include both the local pair-wise potential between two particles U_{pair} and the multi-body potential among non-local particles U_V, i.e.$U = U_{pair} + U_v$. Accordingly, the force field between two neighboring particles only depends on their relative displacement (i.e. pair-wise potential), but it also includes a contribution from all the neighboring particles surrounding them (i.e. non-local multi-body potential). The VCLP has been successfully applied to study nonlinear failure

properties of heterogeneous materials such as particle-reinforced composites, which possesses a similar microstructure to the DIGME.

In our DIGME model we consider each cell to be perfectly bonded with the ECM, and when a cell contracts periodically it pulls the ECM bonded to its perimeter inwardly. This is to mimic the effect of the pulling forces generated via the contraction of actin filaments and transmitted to ECM fibers through focal adhesion during cell migration. During the initial phase of the invasion (the focus of this chapter) most cells possess a rounded morphology and the slightly elongated cells do not appear to show any patterns of alignment. Therefore, we believe that isotropic contraction is a good approximation for studying collective force generation in our DIGME system. In addition, the contraction process occurs much faster than the focal motion of the cells, so that the cell positions are considered stationary for a few contraction cycles. We consider the cell contraction to be characterized by a sinusoidal function, i.e.

$$\delta(t) = \delta_0 |sin(2\pi\omega t + \phi)| \tag{5.1}$$

where $\delta(t)$ is shrinkage of the cell diameter due to contraction with module δ_0 chosen to be 15% of the cell diameter, $\omega = 1/T$ is the individual cell contraction frequency (T is the corresponding period) and φ is the phase for cell contraction with respect to a global reference time. It is important to note that in our current model possible fluctuations of the individual cell contraction frequency ω are not explicitly considered, i.e. we assume that all cells possess identical ω. In general, there are other possible sources for the fluctuations, such as variation of ω among different cells and variation of ω in a single cell over time. To quantify the effects of these possible dephasing mechanisms we carry out a systematic sensitivity analysis by considering a random variation in the single cell contraction frequency across different cells or in a single cell over time. The implications of the analysis are provided in Chapter 5.4.

As we will discuss in the following section, the correlation of φ between different cells quantifies the degree of collectivization of cell contraction (migration) in the system. For the subsequent micromechanical analysis, the contraction of each cell is applied as a time-dependent displacement boundary condition for the ECM; and the fixed zero displacement boundary conditions are applied to

the external boundaries of the square simulation domain for the ECM. Due to the symmetry of the tumor diskoid, the overall effect of cell migration leads to isotropic growth of the diskoid, which can be mimicked in the model by isotropically expanding the circular cell packing region (i.e. re-scaling the intercellular distances).

5.2.3 Stochastic phase construction for modeling collective cell contraction

In our system, the tumor cells in the diskoid can migrate and invade the surrounding ECM. During the migration, a cell pulls the collagen fibers via contraction of actin filaments to generate locomotion. In our model we consider the collective nature of the cell migration to be manifested as the coordinated contraction of cells. As described in section 1, we consider that each tumor cell undergoes a series of periodic contraction cycles with the same periodicity. In particular, each cell i at position r_i possesses an intrinsic contraction phase $\phi_i(r_i)$ (see equation (5.1)). The degree of collectivization is then quantified via the following contraction phase correlation function:

$$S(r) = \langle \phi_i(r_i) \cdot \phi_j(r_j) \rangle \tag{5.2}$$

where $r = |r_i - r_j|$ and $\langle \cdot \rangle$ denotes the ensemble average. Without loss of generality, we use an exponential correlation function, i.e.

$$S(r) = (\phi_1 - \phi_2)\exp(-r/a) + \phi_2 \tag{5.3}$$

where $\phi_1 = \frac{1}{\pi}\int_0^\pi \phi^2 d\phi = \pi^2/3$ and $\phi_2 = \left(\frac{1}{\pi}\int_0^\pi \phi d\phi\right)^2 = \pi^2/4$. The parameter a is the correlation length that characterizes the degree of collectivization in the system. For example, for $a = 0, S(r) = \pi^2/4$, indicating that the contraction (migration) of the cells in the system is completely uncorrelated (asynchronized). On the other hand, for $a \to \infty$, $\mathrm{S(r)} = \pi^2/3$, indicating that cell contraction (migration) is fully synchronized (i.e. all cells contract simultaneously). The major task of our modeling effort is to estimate the a value in the DIGME from the experimentally measured ECM displacement field profile in order to assess the degree of collectivization in such system.

Collective cell contraction characterized by the phase correlation function equation (5.3) with a specific correlation length a can be realized using inverse reconstruction using stochastic optimization. Initially, each cell is assigned a phase φ that is randomly selected from $[0, \pi]$. The phase correlation

$S(r)$ is then computed from this initial configuration. We define an 'energy' as the squared difference between the computed and target correlation function $S^*(r)$, i.e.

$$\mathrm{E} = \sum_r [S(r) - S^*(r)]^2 \tag{5.4}$$

Then simulated annealing is employed to evolve the phase distribution in a tumor diskoid. Specifically, at each step the phase ϕ_i of a randomly selected cell i is varied by a random amount $\delta\phi$, leading to a change in the computed $S(r)$ and thus an energy change ΔE. This variation of ϕ_i is accepted with a probability $p = min[1, (exp - \Delta E/T)]$. The parameter T is a fake temperature which is chosen to be high initially and gradually decreases during the simulation, in order to improve the convergence of the algorithm to the global optimum.

5.3 Results

5.3.1 Experimental results

In order to study collective cancer invasion and force generation in three dimensions, we have previously developed a mechanical-based strategy for micropatterning 3D in vitro tumor models, namely DIGME [71]. DIGME allows one to control the micro to mesoscale geometry of the ECM surrounding cell aggregates. In this study we take advantage of DIGME to create circular diskoids consisting of MDAMB-231 cells, a highly invasive breast cancer cell line. We note that although tumor spheroids have been widely used as invasion models in previous studies, the diskoid geometry employed here leads to a plane strain deformation of the ECM and allows us to more accurately capture the cell contraction-induced deformation field in both experiments and subsequent 2D simulations.

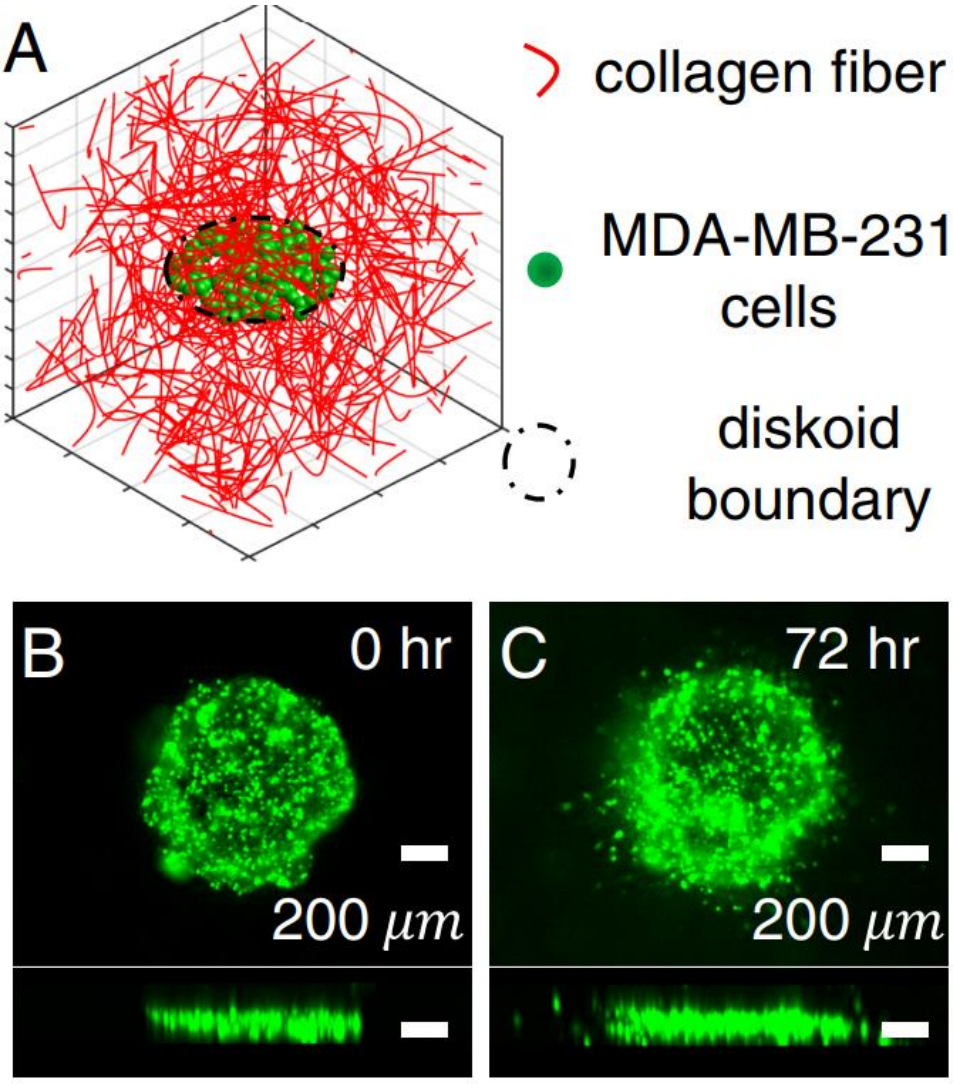

Fig. 5.2 The 3D tumor diskoid setup. (A) Schematics of the circular diskoid embedded in 3D reconstituted type-I collagen matrix. (B), (C) Top views (upper panels) and side views (lower panels) of the tumor diskoid immediately after seeding the cells (B) and after 3 d (C).

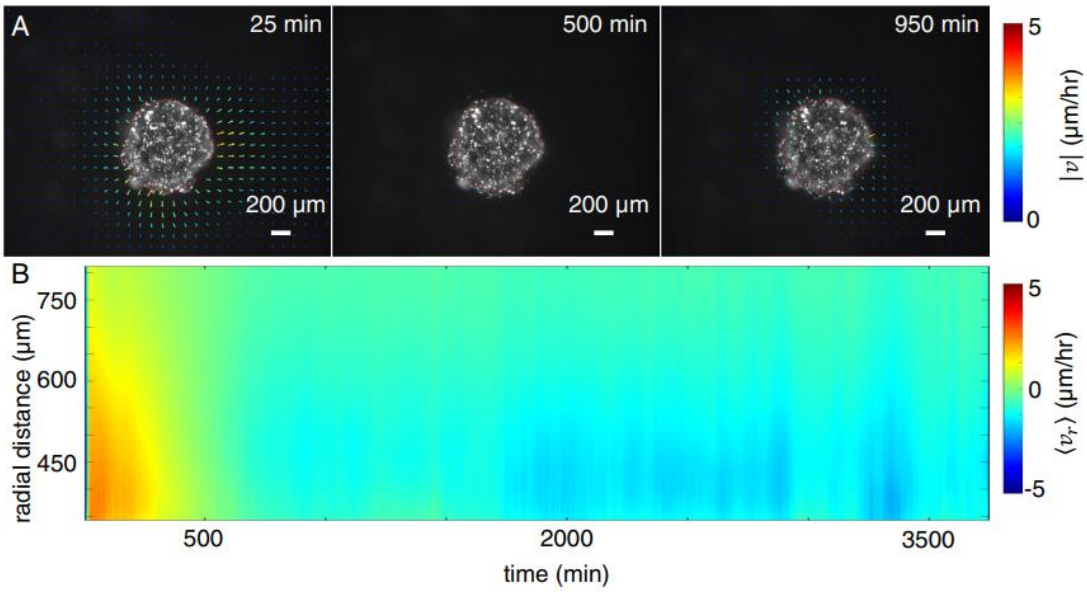

Fig. 5.3 The velocity field of the collagen matrix driven by the tumor diskoid. (A) The velocity field at three different time points indicating pushing, transition and pulling phases of the diskoid force generation. (B) The spatial–temporal map of the average radial velocity.

As shown in figure 5.2, a circular diskoid is a cylindrical cell aggregate confined in a 3D collagen matrix. The diskoid has a high aspect ratio, with a diameter of approximately 920 μm and thickness of 150 μm. Within 3 d of seeding the cells, collective invasion only slightly changes the initial shape of the diskoid. Over the longer term, the invasion is more pronounced in the radial than the vertical direction [71]. The morphological distribution and density evolution of the cells resemble the middle plane of tumor spheroids [18].

In order to probe the effects of the mechanical forces generated by the cells, we embedded 1 μm red fluorescent particles in the collagen matrix so that the GFP-labeled cells and the matrix deformation could be monitored at the same time. In particular, we recorded images at the middle plane of the diskoid where such deformation is most significant. For each experiment, we imaged continuously for 3 d at 5 min intervals, employing particle image velocimetry (PIV) to obtain the velocity field of the ECM by comparing images taken 5h apart.

We find that there are three distinct phases in collective force generation (figure 5.2(A)). Immediately following seeding into the diskoid mold, the tumor diskoid pushes the matrix outward. This is due to the initial spreading of the cells and because the cells are closely packed in the diskoid. The pushing phase is followed by a period of almost zero velocity, after which the diskoid starts to generate a contractive force that pulls the matrix radially inward.

To better visualize the three different phases, we have calculated the average radial velocity $\langle v_r \rangle(t, r)$ over the angle 2π, as shown in figure 5.2(B). The spatial–temporal map shows that the matrix velocity field decays at a larger distance, and that the initial stable pushing force is gradually replaced by a fluctuating pulling force generated by the diskoid.

With the time-dependent velocity field highlighting three different phases in the collective force generation of the cells, we have also computed the strain field in order to further elucidate the stress distribution in the ECM. In particular, we obtain the infinitesimal strain tensor $(t, \boldsymbol{r})$, which is a 2 × 2 matrix that varies in space and time. Equivalently, the strain tensor can be characterized by its two orthogonal principal directions— eigenvectors $v_1(t, \boldsymbol{r})$ and $v_2(t, \boldsymbol{r})$ and the corresponding eigenvalues $\lambda_1(t, \boldsymbol{r})$ and $\lambda_2(t, \boldsymbol{r})$.

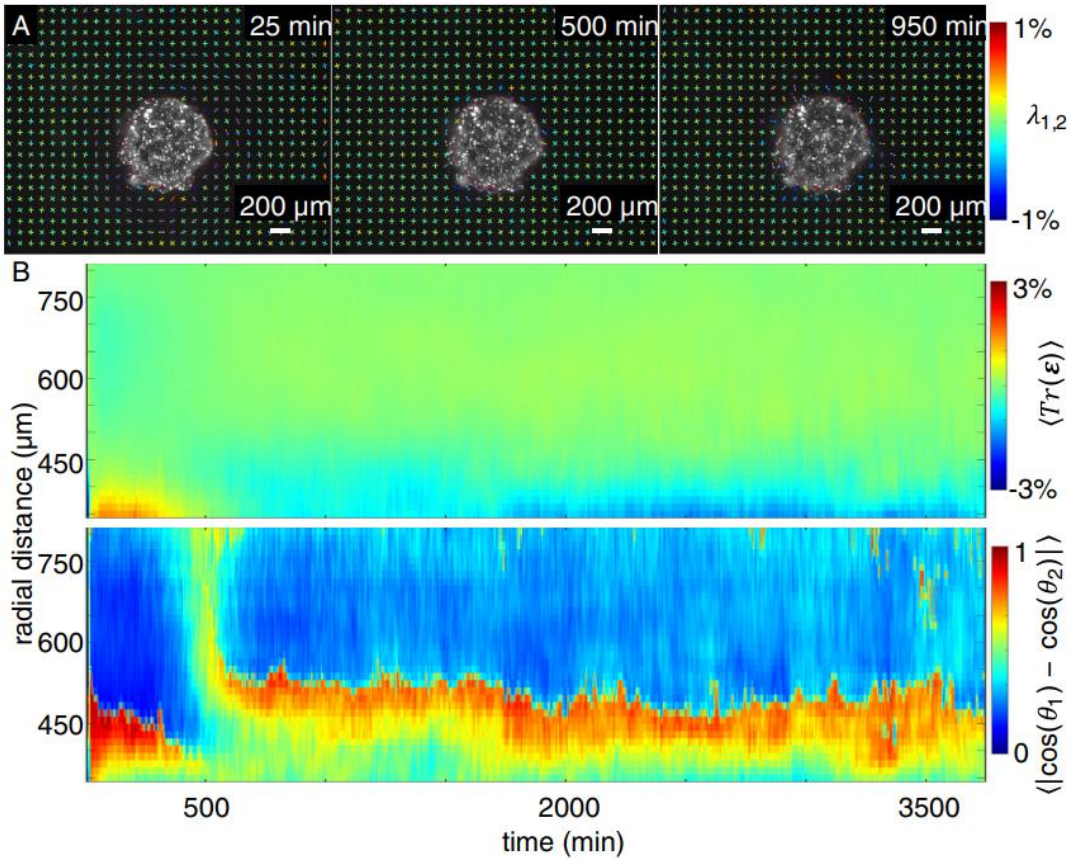

Fig. 5.4 The strain field of the collagen matrix driven by the tumor diskoid. (A) The strain field at three different time points indicating pushing, transition and pulling phases of the diskoid force generation. The lines represent the two orthogonal directions at each location, and their colors represent the corresponding eigenvalues. (B) The spatial–temporal profile of the strain tensor. Top: the spatial–temporal map of the trace of the strain tensor obtained by circularly averaging the trace of the strain field at fixed distance from the center of the diskoid at a given time. Bottom: the spatial–temporal map of the principal directions of the strain tensor with respect to the radial direction obtained by circularly averaging $S = < cos\theta_1 - cos\theta_2 >$ os at fixed distance from the center of the diskoid at a given time. Here θ_1 and θ_2 are the angles between the radial direction and the two principal axes of the strain tensor. The quantity $|cos\theta_1 - cos\theta_2|$ reaches a maximum of 1 if one of the principal axes is in the radial direction, and reaches a minimum of 0 if both principal axes form angles of $45°$ with respect to the radial direction. For both top and bottom panels ⟨·⟩ indicates circular average.

As shown in figure 5.4(A), in the pushing phase the two principal directions are strongly aligned with the radial and tangential directions. The matrix is compressed radially, and extended in the tangential direction. On the other hand, during the pulling phase the strain decomposition has much larger fluctuations, but overall the matrix is extended in the radial direction and compressed in the tangential direction. To further illustrate the quantitative variations of the strain field, we have calculated the angular averaged trace of the strain field $\langle Tr(\epsilon)\rangle(t,\boldsymbol{r}) = \langle \lambda_1(t,\boldsymbol{r}) + \lambda_2(t,\boldsymbol{r})\rangle_{|\boldsymbol{r}|=r}$ at fixed radial distances from the center of the diskoid. As shown in figure 5.3(B), near the boundary of the tumor diskoid the ECM is expanded during the pushing phase and compressed during the pulling phase. The angular averaged trace of the strain field decays rapidly away from the diskoid center. Also consistent with the velocity field, we find that in regions where significant strain is observed, the principal axis of the strain tensor aligns with the radial direction. To further decipher the patterns in the spatial–temporal evolution of the deformation field in figure 5.3(B), we perform a Fourier analysis which clearly shows periodicity in the temporal domain.

After characterizing the collective traction field of a tumor diskoid, we take advantage of computational modeling to address the central question of the report: to what extent do the cells coordinately apply traction force to the extracellular matrix.

5.3.2 Simulation results

In this section, we present our simulation results including the reconstruction of contraction phase distributions with specific correlations in the tumor diskoid as well as the subsequent micromechanical analysis. Figure 5.5 shows the distribution of the contraction phase in tumor cell aggregates (modeled as packings of non-overlapping congruent circles) associated with different phase correlation length a obtained via the stochastic reconstruction method described in section 2.3. In the figure, red indicates large φ values (~π) and blue indicates small φ values (~0). Figure 5.5 shows the scaled target and reconstructed phase correlation functions (see equation (5.3)), i.e.

$$f(r) = = (S(r) - \phi_2)/(\phi_1 - \phi_2) \; = exp(-r/a) \tag{5.4}$$

associated with different correlation lengths a. The final squared error (i.e. the energy; see equation(5.4)) between the target and reconstruction is smaller than 10^{-6} for all cases. It can be seen from figure 5.5 that the reconstructed correlation functions are virtually identical to the corresponding target functions.

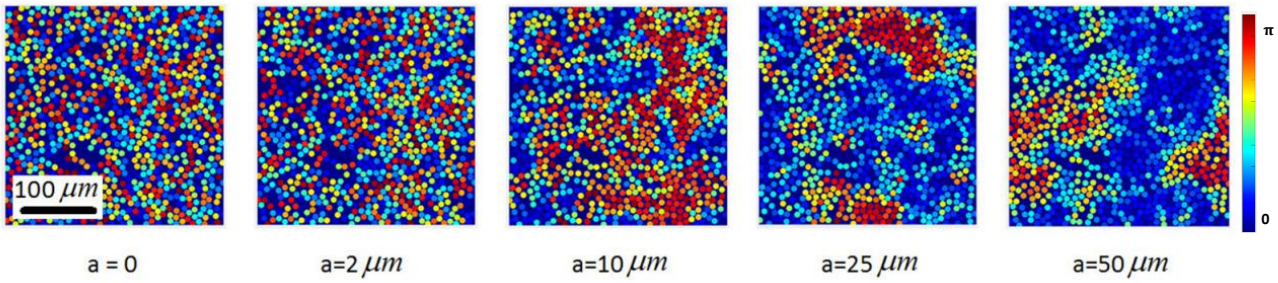

Fig. 5.5 Simulated contraction phase distributions of closely packed tumor cells (with a covering fraction ~0.55). Cells are modeled as non-overlapping congruent circles. The color of each circle (blue to red) linearly scales with the contraction phase (0 to π). A stochastic reconstruction method is employed to realize configurations of varying phase correlation length a.

It can be clearly seen in figure 5.5 that as the correlation length a increases, the regions with similar colors are growing in size, i.e. regions in which the cells possess similar φ values. This indicates that regions containing collectively contracting cells are also growing, which is consistent with the imposed stronger spatial correlations. In addition, as the correlation length increases, the distribution of the φ values also shifts from a uniform distribution (as in the case of a = 0 m) to a bimodal distribution (i.e. for a = 50 μm). The reconstructed cell packings with specific phase correlations are then mechanically coupled with a continuum ECM model to study collective force generation in circular diskoid tumor invasion.

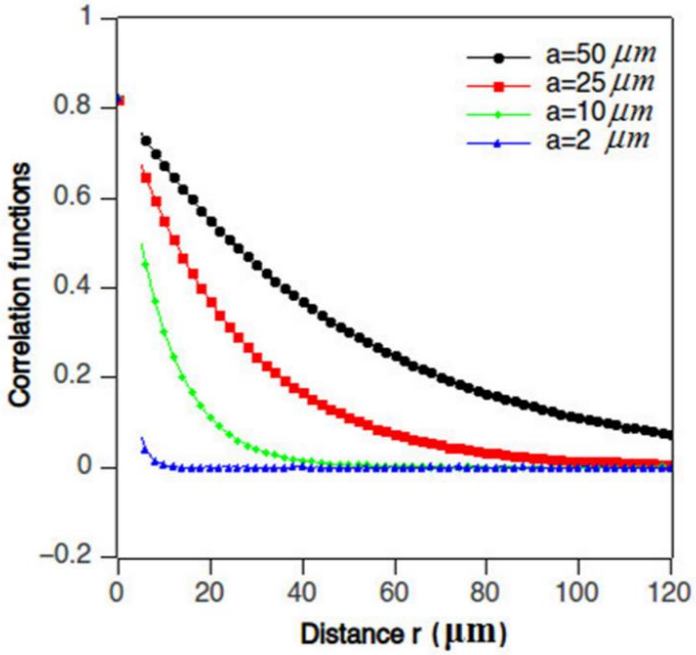

Fig. 5.6 Scaled phase correlation functions equation (5.4) associated with different correlation lengths a. The reconstructed functions (solid symbols) are virtually identical to the corresponding target functions (solid lines).

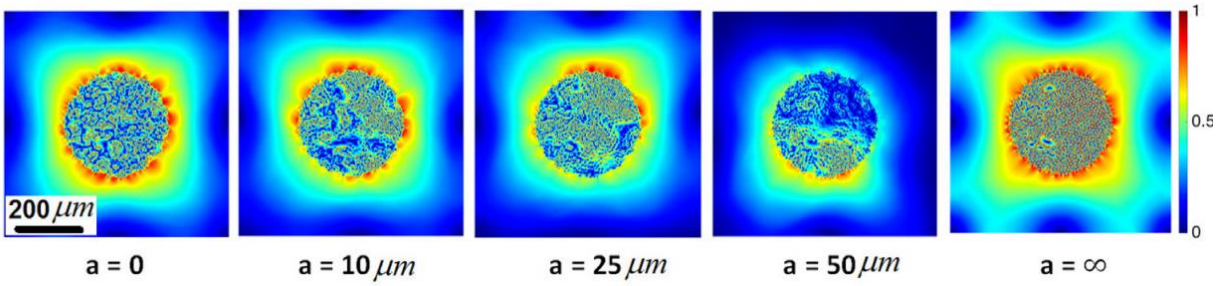

Fig. 5.7 Spatial maps showing the magnitude of the radial displacement from simulated tumor diskoids. One typical snapshot is shown for each phase correlation length. The color scheme linearly scales with the radial displacement magnitude (0 to 1) normalized with respect to the peak displacement value.

We now investigate the deformation of the ECM surrounding the tumor diskoid due to collective cell contraction. In particular, each cell is allowed to contract and deform the ECM according to equation

with its specific phase φi with respect to a global reference time t0 = 0. The contraction of the cells imposes time-dependent displacement boundary conditions at the cell–ECM interfaces, while the outer surface of the ECM is considered to be fixed (i.e. with zero displacement). The VCLP method is subsequently employed to solve the displacement field in the ECM with the aforementioned boundary conditions.

Figure 5.7 shows snapshots of the displacement field, i.e. the distribution of the magnitude of the radial component of the local displacement vector, for different phase correlation lengths. It can be clearly seen that as the correlation length increases, the magnitude of displacement at fixed distance r from the center of the tumor diskoid increases. This is due to the larger pulling forces generated by more collective cell contraction (i.e. with larger phase correlations). In addition, the displacement fields for all cases are almost circularly symmetric, which is due to the isotropy of the tumor diskoid.

Figure 5.8 shows the temporal evolution of the circularly averaged trace of the strain tensor field $\langle Tr(\epsilon)\rangle(t,\boldsymbol{r}) = \langle \lambda_1(t,\boldsymbol{r}) + \lambda_2(t,\boldsymbol{r})\rangle_{|\boldsymbol{r}|=r}$ normalized with respect to $\langle Tr(\epsilon)\rangle_{max}$ in the system for different phase correlation lengths, where λ_1 and λ_2 are the eigenvalues of the local strain tensor. The quantity $\langle Tr(\epsilon)\rangle$ characterizes the local volumetric deformation (i.e. the volume strain) of the ECM due to the contraction of cells in the tumor diskoid, which results in a state of bi-axial tension in the ECM. Consistent with the experimental observation, the principal axis of the local strain tensor is aligned with the radial direction.

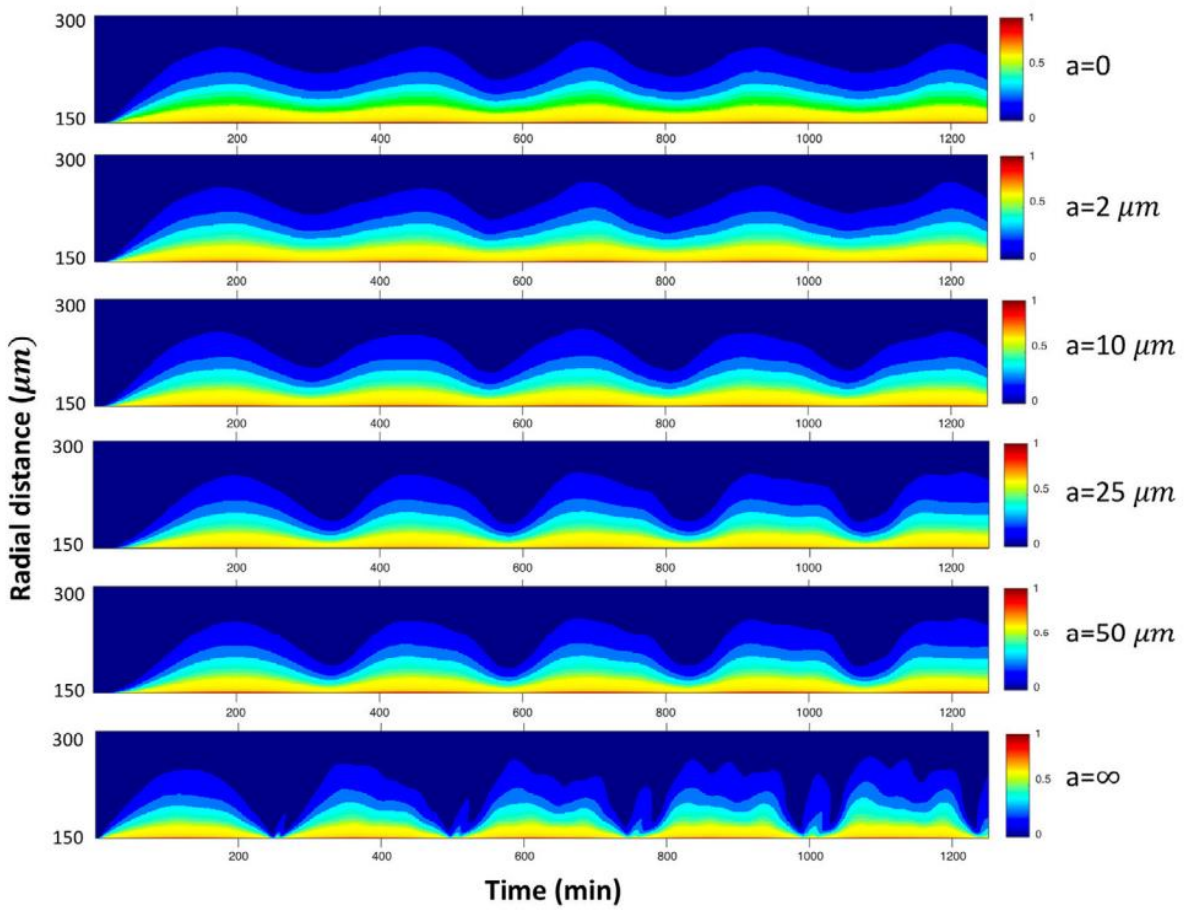

Fig. 5.8 Temporal evolution of the circularly averaged trace of the strain tensor field $\langle Tr(\epsilon)\rangle(t,\boldsymbol{r})/\langle Tr(\epsilon)\rangle_{max}$ normalized with respect to the peak value $\langle Tr(\epsilon)\rangle_{max}$ for different phase correlation length values.

In addition, we note that increasing the correlation length, i.e. the degree of collectivization in cell contraction (force generation), also directly affects the temporal evolution of the circularly averaged volume strain profile. Specifically, for the totally uncorrelated case (i.e. with a = 0 indicating a random distribution of the contraction phase among the cells), the random fluctuations in the contraction phase distribution significantly smooth out the temporal variation in the strain profile. For example, the maximum fluctuation of the strain field at the same location but different time points is about 50% and the deformation of ECM never vanishes. On the other hand, for the fully synchronized case (i.e. with

$a \rightarrow \infty$, indicating the ideal case that all cells contract simultaneously), a significant temporal variation of the volume strain profile that is consistent with the cell contraction period can be identified. It can be clearly seen that the deformation field in ECM almost completely vanishes at t ≈ 250n min (where n = … 1, 2, 3,) and reaches peak values at $t \approx 125 + 250n$ min (where n = … 0, 1, 2,). For intermediate correlations (i.e. intermediate a values), as the correlation length increases, the temporal variation in the strain profile is more significant. We note that this intrinsic dependence of the temporal variation of the deformation field on the spatial correlation length a is sensitive to neither the individual cell contraction magnitude nor the exact values of ECM mechanical properties, and thus this property is sufficiently robust to be utilized to identify the correlation length in DIGME.

5.3.3 Probing the collectivization in DIGME

We now utilize the correlation length-specific timedependency feature of the volume strain profile to identify the correlation length, i.e. to quantify the degree of collectivization in force generation from the experimental data for the DIGME system. We first note that the experimentally obtained volume strain profile contains a bi-axial compression state during the initial stage of tumor diskoid evolution, which is mainly due to the volumetric expansion of the entire tumor cell colony when seeded in the ECM. Since this strain state is not associated with the forces generated via cell contraction during collective migration, we exclude this part when comparing with our simulation results.

For quantitative comparison of the experimental and simulation results, we first normalize the volume strain profile with respect to the corresponding peak value and the large-distance asymptotic value, i.e.

$$\langle Tr(\epsilon)\rangle^*(t,\boldsymbol{r}) = \frac{\langle Tr(\epsilon)\rangle(t,\boldsymbol{r}) - \langle Tr(\epsilon)\rangle(t,\boldsymbol{r}\rightarrow\infty)}{\langle Tr(\epsilon)\rangle_{max}} \tag{5.5}$$

For each a value, we shift the phase Φ and re-scale the time with factor γ for the entire volume strain profile to minimize the squared error between the simulated and smoothed experimental data, i.e.

$$E = min[\textstyle\sum_{r,t}\left|\langle Tr(\epsilon)\rangle^*_{sim}(\gamma t + \Phi, r|a) - \langle Tr(\epsilon)\rangle^*_{exp}(t,r)\right|^2] \tag{5.6}$$

Then the a value associated with the smallest *E* will be identified, and considered as the phase correlation length for the experimental DIGME system.

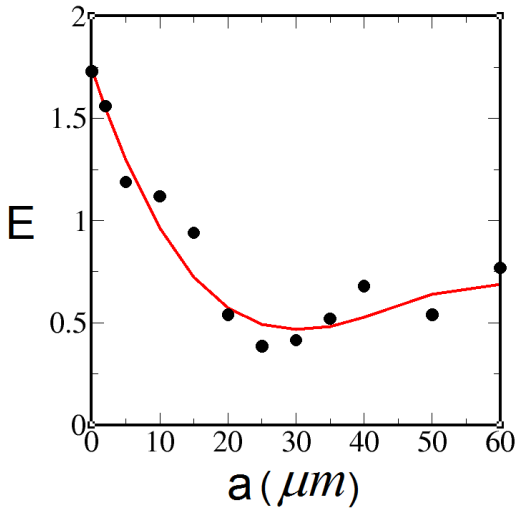

Fig. 5.9 normalized square error E between the simulated and experimental strain profiles as a function of correlation length a.

Figure 5.9 shows the normalized square error E as a function of correlation length a. The normalized square error effectively measures the averaged relative difference of the volumetric strain in the ECM obtained from experiments and simulations. The solid symbols show the calculated E values (5 realizations were used for each a) and the solid line is the corresponding nonlinear fitting result (using a cubic polynomial). Through the aforementioned analysis, we find that the strain profile associated with a correlation length a ≈ 25μm minimizes the squared error (see equation above) among all a values examined. In our model, the cell size (i.e. the diameter of the circles) is set to be 10 μm. Thus, the identified correlation length corresponds to the size of about two to three cells. We note that our analysis mainly emphasizes the intrinsic dependence of the temporal variation of the deformation field (e.g. strain profile) on the correlation length, instead of trying to match the exact values of the simulated and experimental deformation fields. Therefore, the obtained correlation length is not affected by the different reference states that are used to define the strain field in the simulation and experiment (e.g. a global stress/strain free state for the simulation and local reference states taken every 5h for the experiment). It is also important to note that the scaling parameter γ in equation is related to the individual cell contraction frequency, i.e. $\gamma = 2\pi\omega = 2\pi/T$. The obtained γ

value that minimizes the error corresponds to T = ≈ 1/ω 220 min. We also verify our estimated individual cell oscillation periodicity (~220min) by comparing the experimental value (~230 ± 30 min) obtained by observing individual cells randomly dispersed in an ECM with lower cell density. However, it is important to note the oscillation periodicity could also depend on the cellular microenvironment, which could lead to the observed discrepancy.

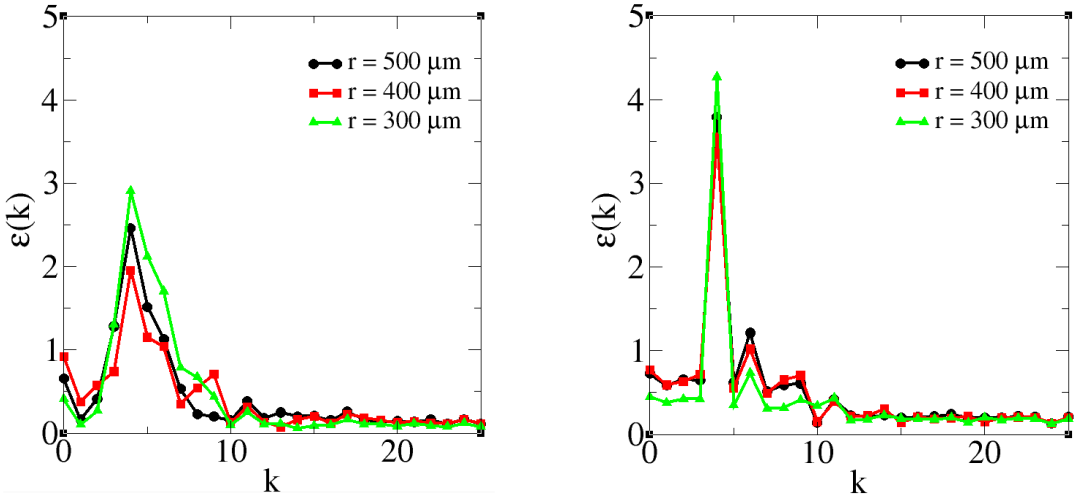

Fig. 5.10 Direct comparison of the Fourier transform of experimentally measured spatial-temporal profile of the deformation field (left) and the simulation results (right) for a = 25 μm. Results for angularly averaged local deformation at 300 μm, 400 μm and 500 μm away from the center of the cell aggregate are shown.

In figure 5.10, the plot shows a direct comparison of the Fourier transform of experimentally measured spatial-temporal profile of the deformation field and the simulation results. It can be clearly seen that both the experimental and simulation data show clear periodicity, indicated by the significant peaks associated with a narrow range of k values. In addition, as the distance from the aggregation center increases, the magnitude of the peak decreases, indicating the periodicity gets weaker as one moves away from the center. We note that the peaks in both experimental and simulation data correspond to roughly the same values of k, verifying that the obtained correlation length a ≈ 25 μm leads to good agreement of simulation and experimental results. However, the magnitude of the peaks

in the simulation data is significantly larger than that in the corresponding experimental data. This implies that the periodicity of the simulation data is stronger, possible due to the fact that we have used a uniform cell contraction periodicity (frequency) while in the actual DIGME system the individual cell contraction periodicity may fluctuate among different cells. The effects of these possible fluctuations on the overall spatial-temporal evolution of the deformation field are discussed in the previous section on sensitivity analysis.

5.4 Discussion and conclusions

In this chapter we have presented a phenomenological model to probe coordinated force generation during collective migration of breast cancer cells. In our model, cell–cell communication is characterized by a single parameter that quantifies the correlation length of cellular migration cycles, without explicitly considering the detailed mechanisms of the communication. Realizations of contracting cell colonies with different correlation lengths are generated using a stochastic reconstruction method. We find that the time-dependent ECM strain profile possesses an intrinsic dependence on the cell correlation length a. This feature is subsequently utilized to identify the correlation length in experiments on cancer diskoid invasion, which leads to a ≈ 25 μm. This intermediate correlation length is roughly twice the linear size of the cells in the system. Interestingly, such intermediate correlation lengths have also been observed for 2D cell monolayers where the cells are either communicating chemically through gap junctions or mechanically through direct contacts.

It is not surprising that an intermediate correlation length arises from our analysis. The tumor diskoid possesses a fairly high cellular density. Thus, it can be expected that the biochemcial and biomechanical mechanisms giving rise to long-range cell–cell communications might be suppressed by the strong nearest-neighbor screening effects. In 3D collective cell migration, one of the possible mechanisms for coordinating collective force generation is collagen fibermediated stress transmission. In particular, it has been shown recently that the actomyosin-generated contraction force of a migrating cell can propagate to the ECM fibers via focal adhesion sites, leading to a heterogeneous quasi-long-

range stress network in the ECM [64]. This implies that the local stress state near a particular cell may result from the pulling of a distant cell, which in turn biases focal adhesion formation for the current cell and its migratory behavior. We expect this mechanism to be important in the tumor diskoid system where cells are embedded in a 3D, albeit thin, block of ECM. Another important mechanism for collective force generation involves the mechanosensitivity of individual cells. For example, it was shown in that cells can adjust their contractile forces according to the forces they experience from other cells, which in turn could lead to collective contraction of the entire colony.

An important question is whether the identified correlation length is intrinsic to breast cancer cells or is dependent on the specific system. Based on the aforementioned analysis, we believe the near-neighbor screening effects could play an important role in the densely packed DIGME system and effectively reduce the correlation length among cells. In a more spreadout cell configuration with a much lower cellular density we expect to observe a longer correlation length for the tumor cells. Nonetheless, this also illustrates the importance of the heterogeneous microenvironment in determining collective tumor cell behavior.

Finally, we note that in our model we have assumed that all cells possess the same contraction periodicity (or equivalently frequency) and we ignored any possible fluctuations in these quantities. As shown in the supporting information, increasing fluctuations in the contraction periodicity or frequency of individual cells will result in less coherent cell contraction and force generation, which would further smooth out the temporal variation in the deformation field. This in turn would result in an effectively smaller correlation length in the tumor diskoid. This analysis suggests that ignoring the possible fluctuations in individual cell contraction frequency and periodicity would lead to an underestimate of the correlation length in the system. Therefore, the obtained a = 25 μm from the current study should be considered as a lower bound on the correlation length in a rigorous sense. In addition, the possible plastic behavior of the collagen network is also not explicitly considered in our current model. The plastic behavior of the ECM due to the permanent remodeling of the collagen network by cellular forces will result in accumulated plastic strain in the ECM. However, we expect that the temporal variation of the overall strain profile still strongly depends on the contraction correlation length, which can be utilized to

determine the correlation length. We will investigate these issues in future work using a similar procedure to that introduced here.

6. LOW-MELTING-POINT ALLOY (LMA)/ POLYMER COMPOSITES FOR DYNAMICAL DRY ADHESION TUNING IN SOFT GRIPPING

6.1 Introduction

Applications of rapid and reversible change in mechanical rigidity are common in nature. Examples range from muscle-powered motor tasks and sexual reproduction, to spontaneous change in shape for predator evasion[101]. Organisms typically perform rigidity tuning with striated muscle tissue or hydrostatic skeletons. In echinoderms, such as the sea cucumber, mechanical rigidity can also be controlled with catch connective tissue, which is composed of a network of relatively inextensible collagenous fibers in a soft protoglycemic gel. These natural composites and structures are lightweight and require ~0.1-1 s to change their tensile rigidity by 1-2 orders of magnitude. Such properties are essential in order for an organism to perform mechanical work, support heavy loads, and control internal stress distributions while still preserving their mechanical versatility.

Rigidity tuning is also important in engineered systems, such as robotics where control of actuation and mechanical response is often of paramount importance. There has been growing interest and activity in ‘soft’ robotics composed almost entirely of soft matters such as elastomers, gels, fluids and colloidal suspensions[182]. These soft machines exhibit similar elastic and rheological properties to biological systems. This leads to engineered systems and machines with significantly different properties and applications than systems composed of highly stiff materials such as metals, hard plastics and silicon. Many soft robotic systems seek to exploit rigidity tuning for unique function similar to the examples from nature mentioned above. Specifically, multifunctional composite materials as one of the soft robotic systems in application, especially those with tunable stiffness, have broad applications in biomimetic and soft robotics for manufacturing, healthcare, and aerospace industries [101][102].

Some common engineering materials used to control stiffness make use of smart fluids or shape memory materials. Smart fluids, such as magnetorheological (MR) or electrorheological (ER) fluids, rely on stimulus-induced ordering of nano or micrometer-sized particles to change their viscosity. In order to use this effect to create controllable stiffness materials, smart fluids must be encapsulated to

allow the application of mechanical loads without loss of fluid. When confined, the MR- or ERfluids can be used to change the mechanical properties of the supporting material. However, these materials can suffer from high mechanical losses, and in fact, one of their main applications is in tunable dampers. Furthermore, the particles can settle out of solution over time and lose functionality[102].

Shape memory materials, such as shape memory polymer (SMP) and shape memory alloy (SMA), are able to change stiffness through stimulus-induced changes in molecular structure. SMPs have been produced that can change states by exposure to chemical or photo stimuli. 12 However, the majority of shape memory materials operate through temperature changes, where the material softens as it heats up, undergoing a large change in stiffness once a critical temperature is reached. SMPs can have a large relative stiffness change and a wide range of possible rest stiffness but must be applied indirectly through the use of external heaters. SMPs can be mixed with electrically conducting particles to remove the need for a separate heater, but the addition of particles decreases the range of stiffness and loss some functionality[106].

Conductive propylene-based elastomer (cPBE), as another tunable composite, can rapidly and reversibly changes its mechanical rigidity when powered with electrical current. When powered with electrical current, the cPBE heats up and softens when the temperature exceeds a critical softening point. With certain supplied electrical power, the effective elastic modulus of the composite reversibly changes between 1.5 and 37 MPa. This approximately corresponds to the difference in rigidity between human cartilage and skin. A central feature of the composite is the resistance of the embedded cPBE to fracture. While LMPA and carbon-filled thermoplastics or waxes can also be directly heated with electrical current, they are susceptible to brittle failure when in their rigid state and this can prevent initial activation. While such materials may be appropriate for reversibly changing flexural rigidity [101], they cannot be used in applications that require changes in tensile rigidity.

In addition, other current generations of multifunctional composite materials often suffer from slow actuation, low robustness, poor reversibility, or sometimes a combination of these, which can be attributed to the nonsystematic, trial-and-error approaches for the development of such composites [103][104][105][106].

Hence, a controllable stiffness material based on the combination of a conductive, phase-change-material (low-melting-point alloy (LMPA/LMA)), and a soft, stretchable encapsulation layer (poly(dimethylsiloxane) (PDMS)) has been introduced and studied in this chapter to resolve those limitations. Compared to previous elastomer-based multifunctional materials, such as Conductive Propylene Based Elastomers (CPBEs) [101], the use of LMA as the conducting phase increases the electrical conductivity of the composite, and allows for drastic rigidity change when LMA is melted quickly under Joule heating, while the encapsulating PDMS allows the microstructure to maintain its pre-molten shape in order to preserve its intended electrical and mechanical properties. The LMPA also reduces the density of the composite, reduces the overall stiffness of the composite, and most importantly, makes possible the dynamical tuning of the thermal expansion of the overall composite before and after the melting of the LMA phase. This new feature might hold the key to achieve very high on/off ratio soft dry adhesives, which has ample applications in compliant gripping of delicate objects.

In this chapter, we investigate the structure-property relationships and provide systematically simulation analysis for a novel class of binary-phase conductive composites with optimized properties including tunable stiffness and thermal expansion for soft robotics applications. To realize this new concept of soft multifunctional composites, we propose to integrate computational material modeling and optimization seamlessly with advanced manufacturing and experimental characterization. Specifically, our procedure generalized the widely-used Yeong-Torquato reconstruction procedure by including a damped oscillation exponential two-point correlation function, i.e., $S_2(r) = \exp(-r/a)\cos(wr)$, for quantitatively represent the LMA composite microstructure. By systematically tuning the characteristic correlation length, a, and the spatial correlations within the inclusion phase, w, one can produce a spectrum of three-dimensional binary-phase composite with various morphology. Also for the purpose of quantify the phase variation, thermal expansion behavior has been modeled dynamically without considering specific thermos-mechanical coupling since the study more focus on the crack distribution effect instead of evolution of the exactly process of the Joule heating.

We also study the mechanical performance of the generated binary-phase composite microstructure including both elastic and failure behaviors using a volume-compensated lattice-particle method. By comparing the composite sample with different gripped materials, we find although the stress distribution on the interface is more balanced if the gripped sample is harder, the stress concentration still locates on the intersection of the harder LMPA and the bottom gripped sample. In addition, we find the composite without any phase changed has significant differences on the rigidity than its counterpart, the pre-existed crack microstructure induced by thermal expansion, up to 6 times.

The rest of the chapter is organized as follows: In 6.2, we provide definitions of correlation functions, the quantities that are relevant to microstructure reconstruction and method we are using for mechanical analysis. In 6.3, we present the stochastic reconstruction procedure for generating LMPA composite and respectively provide detailed analysis on the structural and mechanical properties of the generated materials. In Sec.6.4, we make concluding remarks.

6.2 Simulation Methods

6.2.1 Microstructure quantification via spatial correlation functions

In general, the microstructure of a heterogeneous material can be determined by specifying the indicator functions associated with all of the individual phases of the material [3]. Without loss of generality, we focus on two-phase materials (binary medium) in this work. The generalization of the subsequent discussion to a multiple-phase system is straightforward.

Consider a two-phase heterogeneous material with volume V in either two- or three-dimensional space. This material contains two disjoint phase regions: phase 1 with a total volume V_1 and volume fraction φ_1 , and phase 2 with a total volume V_2 and volume fraction φ_2. Based on the nature of the two-phase material, it is clear that $V_1 \cup V_2 = V$ and $V_1 \cap V_2 = 0$. In the following discussions, we consider phase 1 as our phase of interest, and the indicator function $I^{(1)}(x)$ of phase 1 is given by

$$I^{(1)}(x) = \begin{cases} 1, x \in V_1 \\ 0, x \in V_2 \end{cases} \tag{6.1}$$

The indicator function $I^{(2)}(x)$ for phase 2 can be defined in a similar fashion, and it is obvious that

$$I^{(1)}(x) + I^{(2)}(x) = 1 \tag{6.2}$$

The n-point correlation function (or n-point probability function) $S_n^{(1)}$ for phase 1 is then defined as:

$$S_n^{(1)}(\boldsymbol{x_1}, \boldsymbol{x_2}, \dots, \boldsymbol{x_n}) = \left\langle I^{(1)}(\boldsymbol{x_1}) I^{(1)}(\boldsymbol{x_2}) \dots I^{(1)}(\boldsymbol{x_n}) \right\rangle \tag{6.3}$$

where the angular brackets "⟨…⟩" denote ensemble averaging over independent realizations of the random material. The two-point correlation (probability) function $S_2^{(1)}$ can be directly derived from Eq. (3), i.e.,

$$S_2^{(1)}(\boldsymbol{x_1}, \boldsymbol{x_2}) = \left\langle I^{(1)}(\boldsymbol{x_1}) I^{(1)}(\boldsymbol{x_2}) \right\rangle \tag{6.4}$$

If the material system is statistically homogeneous, i.e., the joint probability distributions describing the random microstructure are invariant under a translation (shift) of the space origin, $S_2^{(1)}$ is a function of the relative displacements, i.e.,

$$S_2^{(1)}(\boldsymbol{x_1}, \boldsymbol{x_2}) = S_2^{(1)}(\boldsymbol{x_1} - \boldsymbol{x_2}) = S_2^{(1)}(\boldsymbol{r}) \tag{6.5}$$

where $\boldsymbol{r} = \boldsymbol{x_2} - \boldsymbol{x_1}$. If the material system is further statistically isotropic, i.e., the joint probability distributions for the microstructure are invariant under rigid-body rotation of the spatial coordinates, $S_2^{(1)}$ becomes a radial function, depending only on the scalar separation distances,

$$S_2^{(1)}(\boldsymbol{x_1}, \boldsymbol{x_2}) = S_2^{(1)}(|\boldsymbol{r}|) = S_2^{(1)}(r) \tag{6.6}$$

In the ensuing discussions, we will drop the superscript denoting the phase index in $S_2^{(1)}$ for simplicity. Without further elaboration, S_2 always denotes the two-point correlation function for the phase of interest. Based on its definition, we can easily obtain the limiting values of S_2, i.e.,

$$\lim_{r \to 0} S_2(r) = \varphi_1 \text{ and } \lim_{r \to \infty} S_2(r) = \varphi_1^2 \tag{6.7}$$

Eq. (6.7) can also be derived from the probability interpretation of S_2, i.e., the probability of two random chosen points separate by distance r, both falling into the phase of interest. In general, the n-

point correlation function S_n provides the probability that a randomly selected n-point configuration with all of the points falling into the phase of interest.

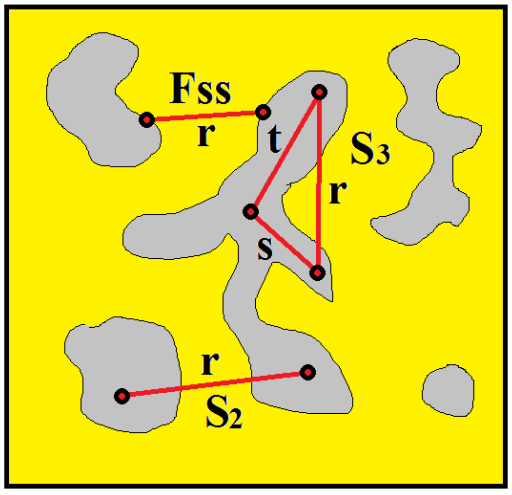

Fig. 6.1 Schematic illustration of the probability interpretation of the correlation functions employed in this work. The line segments (two-point configurations) and triangles (three point configurations) illustrate the events that contribute to the corresponding correlation functions.

6.2.2 Stochastic 3D microstructure reconstruction

In this section, we will introduce the general simulated annealing reconstruction procedure originally developed by Yeong and Torquato[39][40]. In the original YT framework, the reconstruction problem is formulated as an "energy" minimization problem, in which the energy E is defined as the sum of the squared difference between a set of target correlation functions $f^*(r)$ computed from the microstructure of interest and the corresponding functions $f(r)$ computed from an intermediate microstructure, i.e.,

$$E = \sum_{r=0}^{\infty}[f(r) - f^*(r)]^2 \tag{6.8}$$

The energy minimization problem is then solved using the simulated annealing method [54]. Specifically, starting from a random initial trial microstructure which contains a fixed number of voxel for each phase, the positions of two randomly selected voxels with different phases are switched, which results in a new trial microstructure. The tomographic radiographs and the correlation functions for the

old and new trial microstructures are computed to obtain the associated energy E_{old} and E_{new}. The probability that the new trial microstructure will be accepted to replace the old trial microstructure is given by,

$$P_{acc}(old \rightarrow new) = min\left\{1, \exp(\frac{E_{old}}{T})/\exp(\frac{E_{new}}{T})\right\} \quad (6.9)$$

where T is an effective temperature used to control the acceptance rate for energy-increasing trial microstructures. In the beginning of the simulated annealing process, the parameter T is chosen to be relatively high in order to achieve an acceptance probability of approximately 0.5. Then T is gradually reduced according to a prescribed cooling schedule as the simulation proceeds in order to allow the energy to converge to a very small value if not zero. In the current work, we choose an exponential cooling schedule, i.e., $T(t)/T_0 = \gamma^t$, where $0.95 < \gamma < 0.99$. As T gradually decreases, the acceptance probability for energy-increasing trail microstructure will also decrease. Eventually the energy converges to a (local) energy minimum, which is associated with microstructure that is very close to the actual material structure. In practice, the global energy minimum is extremely difficult to reach, and we claim the reconstruction is successfully accomplished if the energy E drops below a prescribed tolerance value (e.g., 10-6).

During the reconstruction process, after a new trial microstructure is generated, the energy E given in Eq. (21) needs to be computed to determine whether the new microstructure should be accepted or not based on the probability (18). In a typical reconstruction, a large number of trial microstructures (e.g., several millions) will be generated and thus, it is crucial that E can be computed efficiently for the procedure to be computational feasible. We have developed highly efficient algorithms to compute E_1 and E_2, by re-using the information stored for the old trial microstructure [33]. The basic idea is based on the fact that the new and old trial microstructures only differ from one another by a pair of switched pixels. The majority of the two-point statistics and attenuated intensity in the tomographic radiographs are not affected by such pixel swapping. Therefore, there is no need to re-compute these data from the new microstructure from scratch, and only the affected values should be identified and updated in order to compute the energy of the new microstructure using Eqs. (19)-(21). The detailed procedures for updating various correlation functions and simulated projections after a

pixel swapping are respectively discussed in detail in Refs. [46] and [33], which will not be repeated here.

6.2.3 Volume-compensated lattice-particle (VCLP) method for dynamic fracture simulations

VCLP with first two nearest neighbor square packing is also used in the LMPA/polymer composite system. The key idea of the proposed VCLP as aforementioned is that two potential terms are used to describe the strain energy U_{cell} stored in a unit cell: the energy stored in the local pair-wise neighboring springs Us and the energy associated with the volume change of a unit cell U_v [62][63][64][65]. Note that only a half spring is used in each unit cell while calculating the strain energy, which avoids overlapping. Mathematically, the above hypothesis can be expressed as

$$\mathrm{U}_{cell} = U_s + U_v \tag{6.10}$$

The strain energy stored in the springs has a different form from the hexagonal packing since two types of spring is adopted in square packing. The strain energy Us is

$$\mathrm{U}_s^{square} = \frac{1}{2}\sum_{J=0}^{3} k_1^{square}(\delta l_{ij})^2 + \frac{1}{2}\sum_{J=4}^{7} k_2^{square}(\delta l_{ij})^2 \tag{6.11}$$

where superscript s indicated the square packing, $\mathrm{k}_1^{\mathrm{s}}$ and $\mathrm{k}_2^{\mathrm{s}}$ are the spring stiffness parameters for springs connecting a center particle with the nearest and the second nearest neighbors, respectively. For plane strain case, the strain energy of volume change of a unit cell is

$$\mathrm{U}_v^{square} = \frac{1}{2}V^s T^s(\varepsilon_v^s)^2 = 2R^2 T^s(\varepsilon_{11}^2 + 2\varepsilon_{11}\varepsilon_{22} + \varepsilon_{22}^2) \tag{6.12}$$

Comparing the components with the stiffness matrix of 2D isotropic homogeneous materials, the potential coefficients can be determined uniquely as

$$k_1^s = \frac{2E}{1+v}, k_2^s = \frac{E}{1+v}, T^s = \frac{E(4v-1)}{2(1+v)(1-2v)} \tag{6.13}$$

Thus, the interaction force within half spring can be obtained as

$$f_{ij} = \begin{cases} k_1^{square}\delta l_{ij} + (\frac{2\sqrt{2}-3}{2})\, T^s(\sum_{J=0}^{7}\delta l_{ij}), & J = 0,1,2,3 \\ k_2^{square}\delta l_{ij} + (\frac{2\sqrt{2}-3}{2})\, T^s(\sum_{J=0}^{7}\delta l_{ij}) & J = 4,5,6,7 \end{cases} \quad (6.14)$$

As a short summary, the model parameters under 2D elastic cases have been derived for square packing. The three-dimensional coefficients can be derived in the equivalent way.

In the fracture model, the failure behavior of materials is governed by a spring-based critical stretch criterion. The crack initiation and propagation are the natural outcome of the spring breakage. No additional external criteria are required. The failure parameter is defined as

$$s_j^{critical} = \alpha_j \cdot R \quad (6.15)$$

Where $s_j^{critical}$ and α_j is the critical stretch and failure parameter for the jth spring, respectively. R is the particle radius.

The spring connected each pair of particle can be treated as permanently broken whenever the stretch length of the bond is longer than the criterion. However, within the effective length, there's no any plastic constrain here but only elastic properties.

6.3 Microstructure reconstruction and simulation Results

6.3.1 Composite microstructure modeling and reconstruction

LMA-polymer composites consist of nanoscale LMA particles and the polymer. In order to quantitatively describe the material structure in the mesoscale, coarse-grained binary microstructure representation of the multi-phase composite has been generated. In the microstructure, since all the nano-particles are too small to be captured in the reconstruction length scale, the continued inclusion with a volume fraction of 30%, a set of effective mechanical, thermal properties and matrix phase in Fig.6.1 would be sufficient to present the porous LMA (air bubbles) and polymer (with voids), respectively.

Four types of 2-point correlation functions shown in the Fig.6.2 are employed here to control the LMA-polymer composites material microstructure.

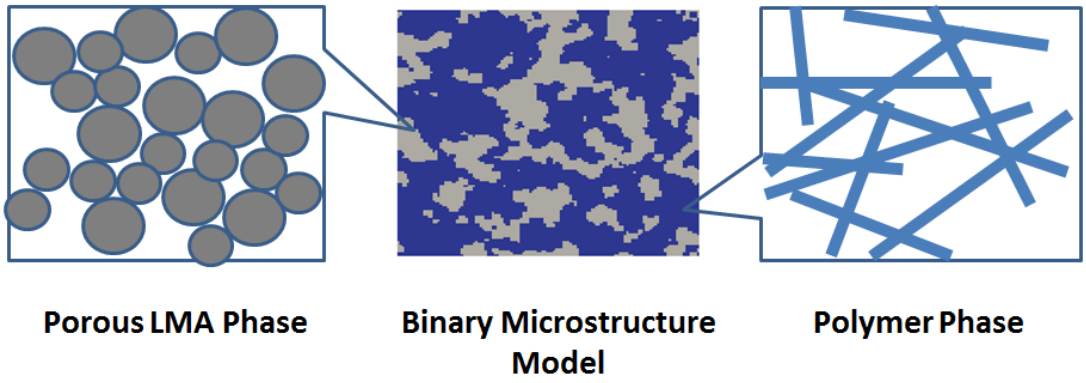

Fig. 6.2 The microstructure model of LMA/polymer composite

The damped oscillation exponential function is given by

$$S_2 = \exp\left(-\frac{r}{a}\right)\cos(wr) \tag{6.15}$$

Where a is a characteristic correlation length of the material and w determines the spatial correlations within the inclusion phase. Here we fix $a = 20\mu m$ and consider various correlation parameter w. Three dimensional virtual microstructures associated with the obtained correlations are then generated using stochastic reconstruction technique(Fig.6.3)

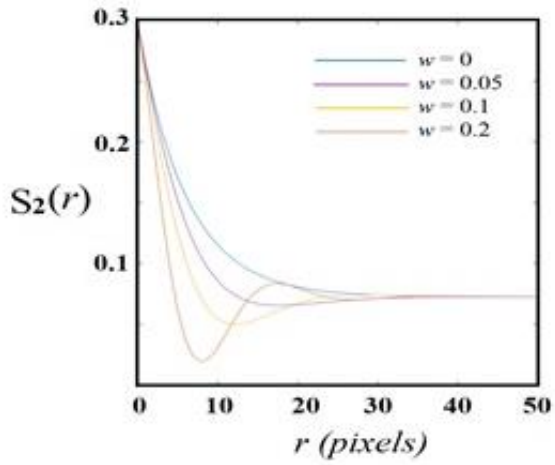

Fig. 6.3 Four damped oscillation exponential function with different spatial correlations w of LMA

Four different parameters of w have been chosen as 0, 0.05, 0.1 and 0.2 in this study to generate various microstructure of the composites. As shown in the two-point correlation function plot, the small

cluster will be more easily to distinguish when the parameter w is getting larger. Since the correlation function describe the probability to find the phase of interest under certain pixel distance, the sharper valley in the function will provide a more separable phase structure. A better idea can be delivered from the figure of top view of the three-dimensional reconstruction result.

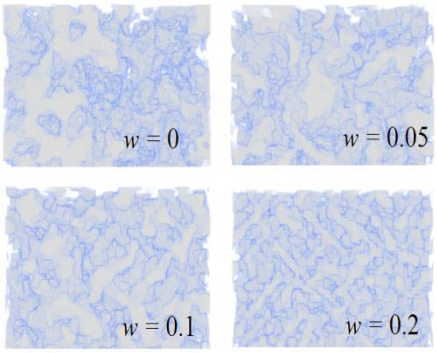

Fig. 6.4 The top view of 3D microstructure reconstruction results with four different spatial correlations of LMA

6.3.2 Tuning maximal pulling force via heat-softening of LMA

A Representative Volume Element (RVE) containing the virtual composite material, a homogeneous gripped sample and their interface are constructed, which mimics the situation where the composite, the low-melting-point alloy (LMA) and polymer, is used in a gripper to hold the sample by dry adhesion (Fig.6.5).

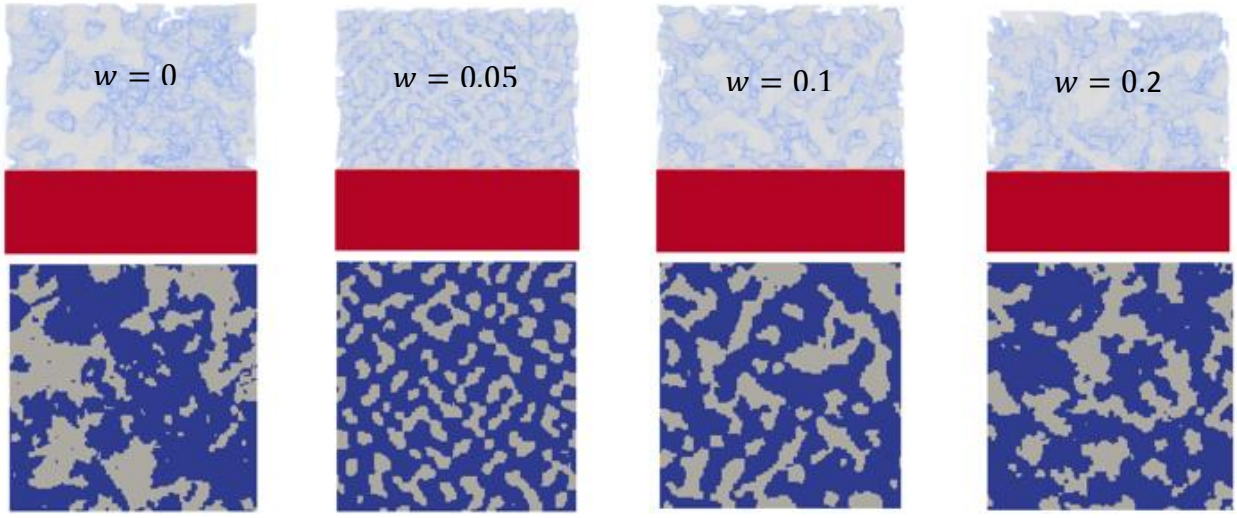

Fig. 6.5 The side view of the soft griping system with different spatial correlation w including LMA/polymer composite on the top and homogeneous gripped sample on the bottom (upper panel), and the top view of the LMA/polymer composite (lower panel)

Uniaxial tensile force has been applied to obtain the elastic strain field (example on figure 6.6) and maximal pulling forces F_{max} associated with different composite microstructures as well by using VCLP method. Specifically, when a pulling force is applied, the composite-glass interface tends to fracture in a brittle fashion, mainly determined by the initial stress concentration distribution on the surface, which in turns depends on the composite microstructure.

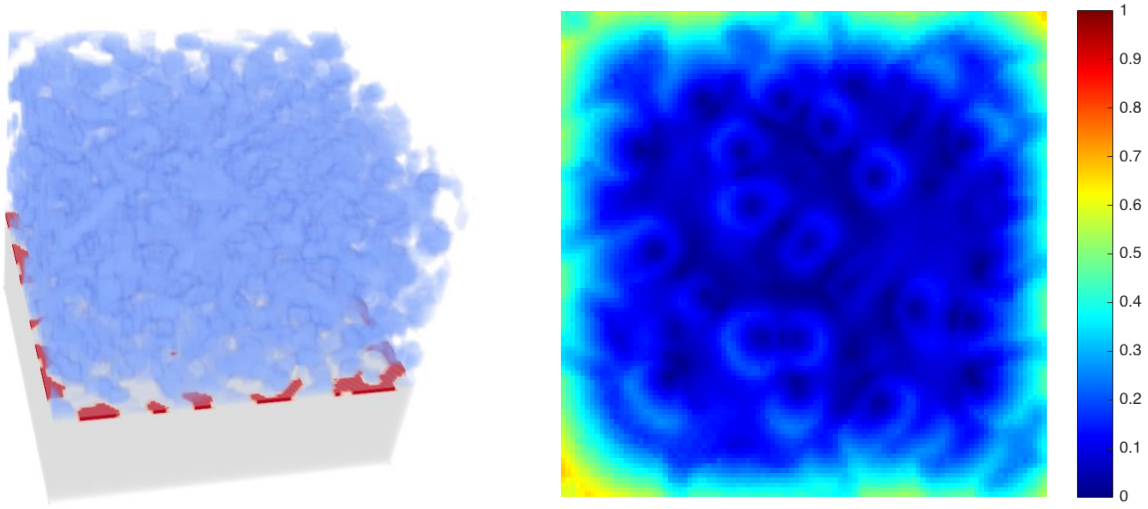

Fig. 6.6 The Representative Volume Element system for the interface of composite and material to be gripped (left) and the example of normalized strain field on the interface

At this stage, four different properties of gripped materials have been used for interface study in which the elastic modulus varies from 1MPa (PDMS) to 1GPa (thermoplastic) as shown in the Fig.6.7. The elastic properties of the gripped material can affect the stress distribution on the interface. The softer bottom gripped sample, the more relatively uniform stress distribution but still concentrate on the interface between LMA and the bottom sample obviously. When tensile test is applied, the bond failure on the surface tends to occur from the high stress concentration on the edge. Also, the PDMS polymer in matrix has also been used as gripped material for simplicity in next simulation comparison and the elastic modulus of polymer, LMA and the gripped material are 1MPa, 2GPa, 1MPa and Poisson ratio 0.3, 0.49, 0.3, respectively. However, the interface bond between bottom gripped sample and the top composites is much weaker because of the small dry adhesion which comes from van der Waals' force. As aforementioned, bond strength is depending on the critical strength and the elastic modulus in which the failure parameter a in Eqa.6.14 is 0.1% and elastic modulus is 1MPa.

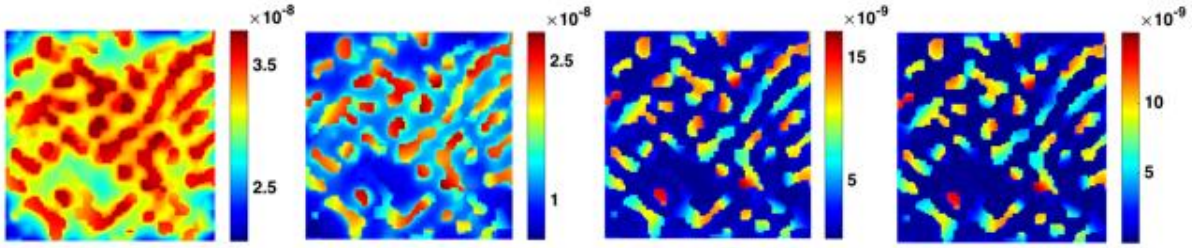

Fig. 6.7 Displacement field on the interface for the gripped sample with different elastic modulus (1e6,1e7,1e8 and 1E9 from the left to right plot, respectively)

Next, an isotropic volumetric eigen strain δ has been applied (0.01% to 0.03%) to the inclusion (LMA/void) phase, to mimic the thermal expansion of the LMA due to Joule heating, which affects the stress distribution on the interface and induces crack nucleation. In the crack initiation part, only the thermal expansion dynamically behavior of the LMA had been simulated instead of thermos-mechanical

coupling since the study more focus on the tensile force sensitivity about the crack distribution. Hence, all the surface of the inclusion phase tries to expand along the normal direction on the edge dynamically until the certain eigen strain has been achieved as show in the figure 6.8.

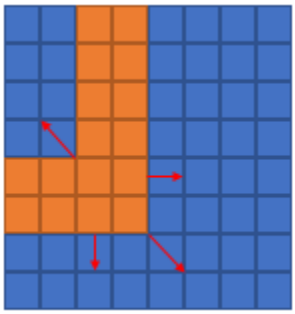

Fig. 6.8 Illustration of thermal expansion model. The inclusion LMA phase (orange) will expand along the normal direction of surface during heating and cracks initiation occurs during extrusion process

During the thermal expansion process, cracks are generated step by step. As the result, few different crack initiation patterns are obtained. Although any magnitude eigen strain applied will lead to an unbalance strain/stress field, small strain of the inclusion phase is not able to have enough extrusion force to its neighbors for cracks initiation. Therefore, final structure of the interface between soft robotic system and gripped sample including perfect interface and crack interface is show in the figure 6.9.

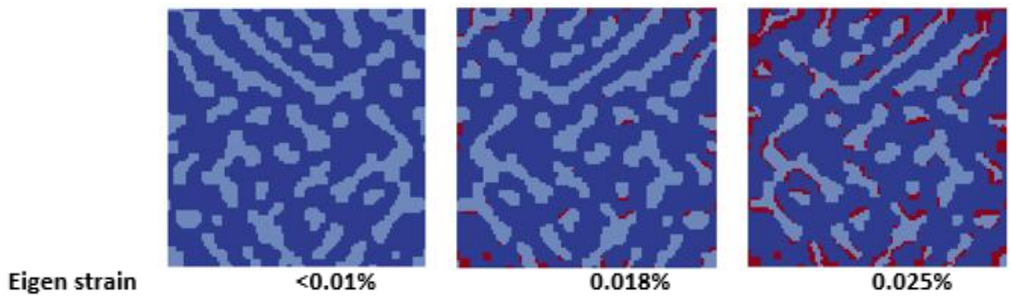

Fig. 6.9 The crack initiation patterns under thermal expansion process. The interface between LMA/polymer composite and gripped sample of crack nucleation from the left to the right corresponds to the eigen strain less than 0.01%, equals 0.018% and 0.025%, respectively

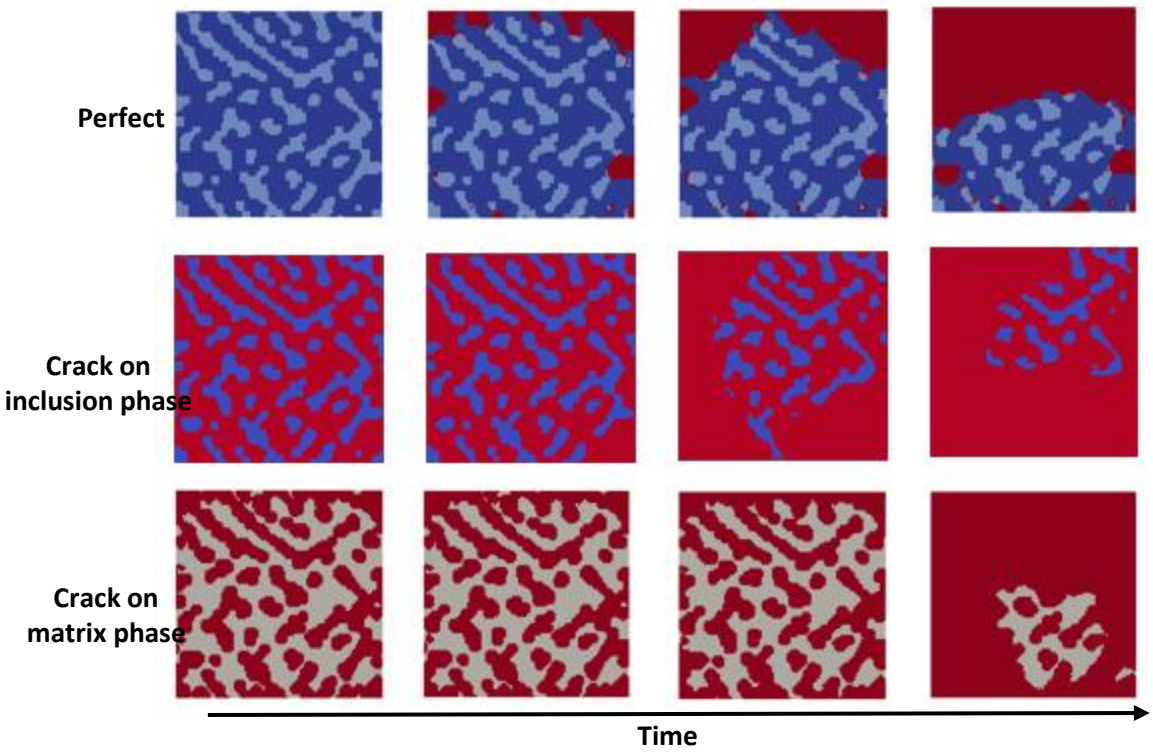

Fig. 6.10 The dynamic surface fracture evolution for three crack nucleation patterns. The light blue, deep blue and red represents the LMA phase, polymer phase and cracks, respectively

Few different patterns of the crack initiation based on the applied eigen strain have been used for further tensile test. As we discussed in chapter 4.5.3, the LPM the continuum is modeled as a regular array of material points interacting with near neighbors and thus, fracture is naturally captured via breaking of bonds between the material points. The critical stress for bond breaking is set to be $\sigma_c = 30$ MPa according to the data in experiments. We note that similar to the elastic analysis, although the exact value of the fracture strength σ_f depends on the choice of σ_c, the conclusions drawn here are not affected by σ_c. A uniaxial load is applied to the square RVE of the reconstructed materials under the quasi-static loading condition, with a strain rate $d\epsilon/dt = 10^{-7}$per loading step and up to $N = 40{,}000$ loading steps are used. After each loading step, the stress and strain distributions in the RVE are computed and each bond is checked for possible breaking. If the stress in a bond is greater than the critical stress σ_c, this bond (i.e., the connection between two materials points) is removed from the

system, which corresponds to the nucleation of a micro-void. This will lead to a significant change of the stress/strain distributions in the next loading step. The reaction force F (and the uniaxial tensile stress) is computed at each loading step. The material is considered to fail when an abrupt drop is observed in F. The fracture strength is then computed from the maximum reaction force, i.e., $\sigma_f = F_{max}/A$, where A is the cross-sectional area of the RVE.

In order to identify the maximal pulling force ratio, two structures of largest eigen strain and the strain-free are mainly discussed. The strain-free structure has a perfect dry adhesion interface without any pre-existed crack and the largest applied strain leads to bonds failure of all the interface between inclusion and the gripped sample. Fig.6.10 shows us the dynamic evolution of the crack propagation in these three interface structures with different crack distribution. In addition, one of the extreme case in which all the bonds of the interface between matrix and the gripped sample are failed has also been investigated so that we can have a better understanding of the tunability of the pulling force depending on the microstructure and pre-existed crack distribution. The pulling force curves of the three aforementioned crack induced structure have been shown on the Fig.6.11 .

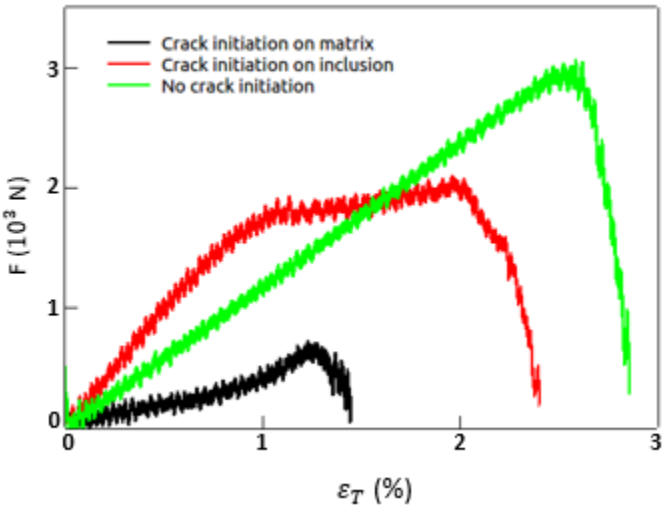

Fig. 6.11 Reaction force as a function of tensile strain ε_T in three crack initiation patterns

Obviously, the strain-free one has the largest pulling force since all of the interfaces are perfect and higher external force is needed to break the dry adhesion. However, the largest strain structure

performs plasticity-like behavior with 1.5 times less pulling force. The interesting point is there's no any pre-designed plasticity in the model. The reason is all of the bonds are broken on the interface between hard inclusion phase and gripped sample and the only connected soft matrix portion can balance the stress concentration. At the meantime, the soft matrix is able to absorb more input force by elongating their bond length which is easier for the soft phase rather than the hard inclusion. Hence, longer bonds length on the force applied surface particle will provide higher reaction force that shown in the plot. On the contrary, if all the bonds are failed on the soft matrix interface, then connected hard inclusion will take more stress concentration and break easier, which we can find clearly that the pulling force 6 times less than the strain-free structure. Therefore, the pre-existed crack distribution induced by the thermal expansion of the low-melting alloy affects the pulling force significantly and exhibits the huge tunability potential of this kind of composite material.

6.3.3 Effects of composite microstructure with coating

Encapsulating PDMS with various thickness coating on the interface which allows the material to maintain its pre-molten shape has also been studied based on the generated composite microstructure as shown in the Fig. 6.12. The range of encapsulating layers is from 0.2 to 0.6 mm and the inclusion PDMS varies from harder to softer through electric current heating. In Fig.6.12, the top panel shows us the effect of the thickness of buffer layer before the LMPA getting melted. When the elastic stretch is applied, the stress concentrates at the PDMS area which is similar to aforementioned result but reflects on the buffer interface instead of LMPA intersection. In addition, the strain concentration is getting more blur and relatively uniform if more layers are coated on the interface, which means the PDMS coating can provide a strain balancing functionality and decrease the strain strength occurred on the interface.

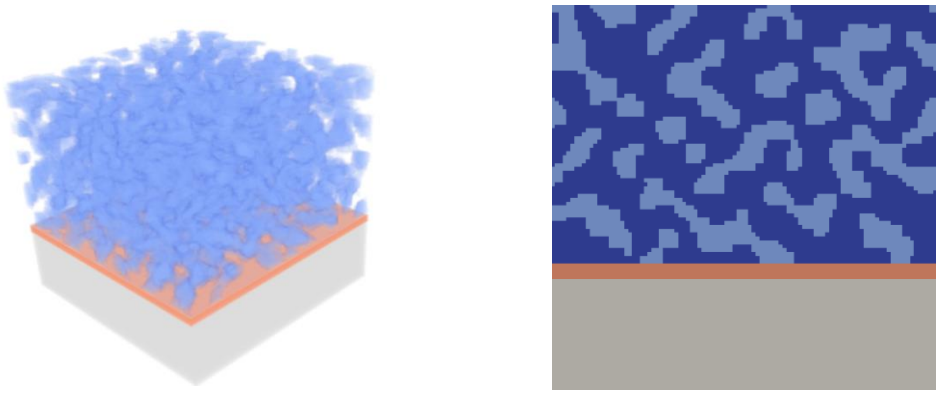

Fig. 6.12 Schematic illustration of the PDMS coating sample. On the left side view of 3D microstructure, orange region is the thin coating of PDMS on the interface between soft robotic composite (upper part) and gripped sample (lower part). 3D view is shown on the right

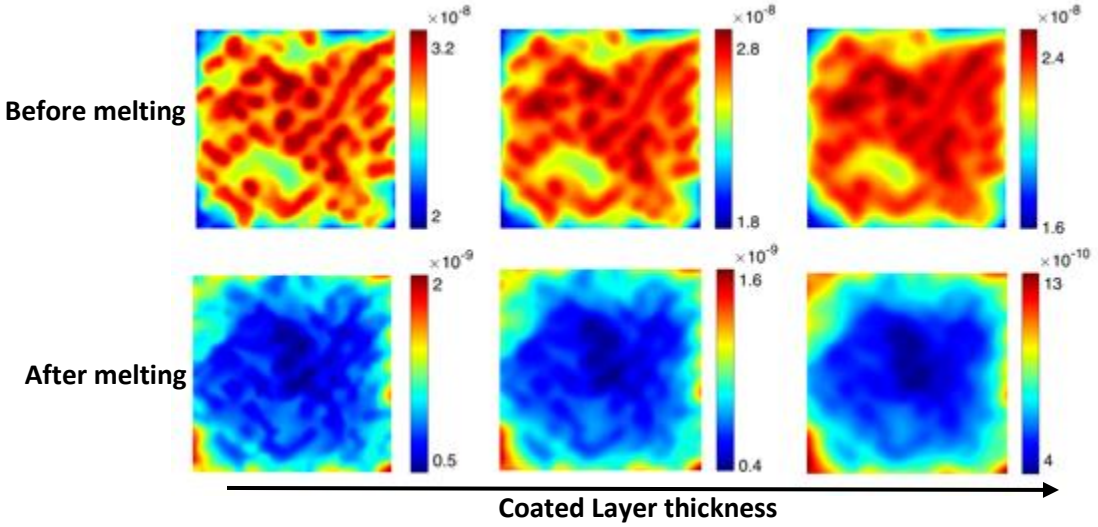

Fig. 6.13 Strain field on interface of PDMS coated sample with different coated layers and elastic modulus of the inclusion LMPA phase. The plots from left to the right is showing the result with the coated layer from 0.2 to 0.6 mm, and top panel shows the hard inclusion and lower panel shows composite with melted inclusion.

The lower panel shows the same agreement when more layers are adding. However, the strain distribution has significantly change when the LMPA is getting melted. Once the rigidity of LMPA is getting lower, all the PDMS on the interface would take the stress applied from the external source and

balance them since PDMS is much softer than the normal LMPA. Therefore, the magnitude of the strain on the buffer layer is much less up to 1.5 times.

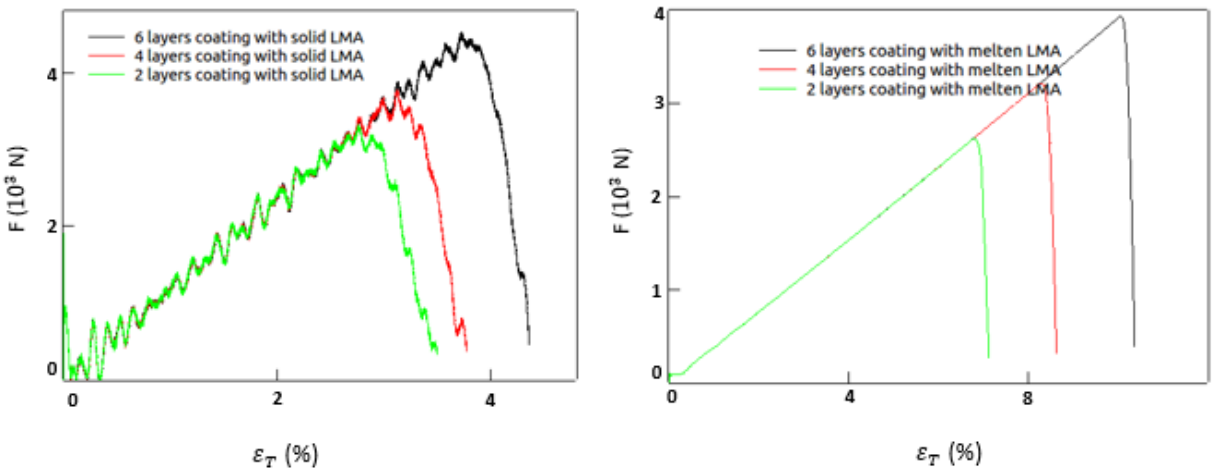

Fig. 6.14 Reaction force as a function of tensile strain ε_T in different coating and inclusion structures. The left one shows the force response of the structure with coating in relatively low electric current in which the LMA inclusion is still solid and the structure with coating and molten LMA is shown on the right.

Uniaxial tensile test is applied in both scenarios including solid LMA and molten LMA with different coating layers. Within the same state of the LMA inclusion phase, more number of coating layers lead to higher fracture strength which has the same agreement on the discussion above since the thicker coating layer is a contributing factor in balancing the strain. By comparing the fracture strength of two different states of inclusion phase, we can easily find out the molten LMA structure possess lower fracture pulling force. In addition, the pulling force ratio of two different states of LMA for 2, 4 and 6 coating layers are 1.43, 1.47 and 1.58, respectively, which means the thinner coating layer could have larger range of tunable rigidity.

6.4 Conclusions and Discussion

In this chapter, we have employed a stochastic optimization procedure to systematically generate realizations of three-phase composites here consist of a soft elastomer matrix, typically polydimethylsiloxane (PDMS), a Low Melting-point Alloys (LMAs) component, and gripped sample as the third component, whose structure controlled by different correlation length of correlation functions. For the purpose of pulling force sensitivity study depending on different electrical current induced LMA heating and expansion, different eigen strain crack patterns have also been generated and analyzed. We found that the damped oscillation correlation function can control the morphology and clustering size of the inclusion phase which affects the stress distribution and concentration on the interface between composite and gripped material. Also, the softer elastic properties of gripped material provide more balanced stress distribution than the harder one. However, if the inclusion phase is the relatively harder phase in the composite material, then the stress on the interface between the inclusion and gripped sample would always be the higher stress area which is the higher potential location for crack initiation and propagation.

In addition, we have investigated the mechanical performance of the reconstructed composite material and their crack induced structure including both the elastic and failure behaviors using the VCLP simulations. From the dynamic pattern of the crack propagation, we can easier to identify the crack growing mechanism which will initiation on the edge no matter for the strain-free structure without any pre-existed crack or for the highest eigen strain structure. However, the highest eigen strain structures are found to be easier failed with 1.5 times less fracture strength. The most interesting part is this structure has plastic behavior in the tensile simulation without any pre-designated plasticity. The harder inclusion phase can be expected as a scaffold in the composite and if their bonds connected on the interface all failed, then all the input force will be directly balanced by the softer matrix which absorb the energy by elongating their bond length. Eventually, the longer bond length on the edge surface of the composite provides higher pulling force under the same displacement boundary condition. On the other hands, the bond length is similar on the particles of interface between the composite and the gripped sample since the softer matrix balance the stress concentration. Therefore, the plasticity-like

behavior induced. While the most force sensitive structure is the one whose bond between matrix and gripped sample is all failed. Since this crack distribution pattern avoid any stress balance factors and all the stress concentration locates on the inclusion interface which result in the fracture strength is 6 times less than the strain-free structure.

The other mechanism is the melted LMPA when high electric current is applied. Another thin film of PDMS is coated on the interface to encapsulate the liquidized inclusion. As the results, the thicker coating layer would decrease the stress/strain concentration magnitude and balance the distribution at the same time. Hence, the fracture pulling force would be relatively small if the coating layer is thicker and this provide us an option for tuning rough range of the soft gripper for specific applications. However, we still recommend the thinner layers since it could provide larger range of rigidity tuning which will be more efficient in real application.

We emphasize our conclusion that the microstructure and pre-existed crack distribution pattern significantly affect the pulling force sensitivity and the most difference can be achieved up to 6 times based on our studies. Generally, it can be expected a carefully designed crack pattern can certainly be made much flexible and tunable in pulling force ratio.

7. FUTURE WORK

From the aforementioned result, we found there's a huge potential for the material design to achieve more flexible tuning in soft griping system. We have studied two different mechanisms including the thermal expansion crack affect during the Joule heating and the PDMS coating for high temperature scenario.

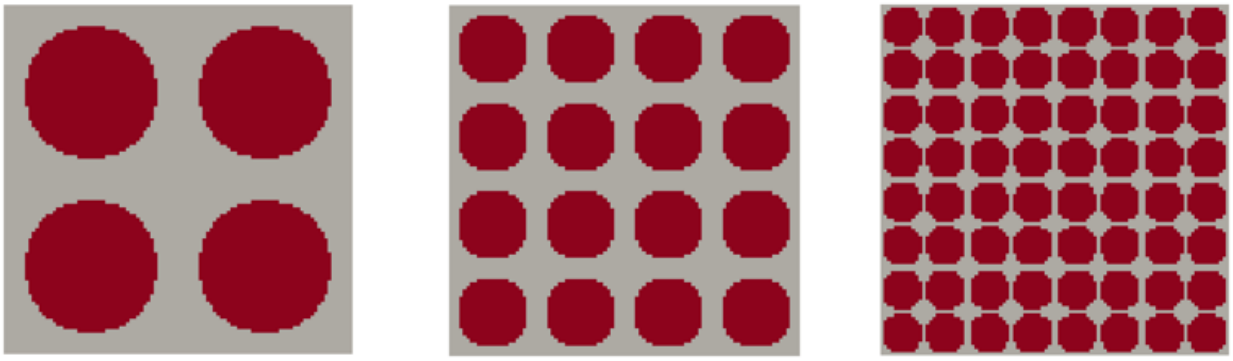

Fig. 7.1 designed crack initiation pattern

While, there's not only these two factors that can provide tunable rigidity. We have further designed few simple crack pattern and studied the effect of the pulling force ratio as shown in the figure 7.1. All the red regions represent the crack area and all the bonds connected to the gripped sample are broken. The designed pattern is feasible in sample fabrication by controlling the fabrication process or applying post-processing, for example, the laser oblation.

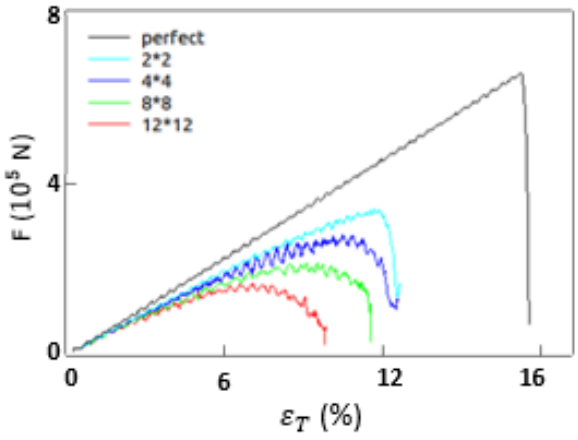

Fig. 7.2 Reaction force as a function of tensile strain ε_T 5 different designed circular crack patterns

As the preliminary result shows, more uniform distributed crack initiation leads to a lower fracture strength which is used for lighter object. On the contrary, the structure in which all the crack aggregate together as cluster would be hard to fracture and is better for afford heavy sample. As shown in the figure 7.2, the simple nucleation patterns provide us up to 4 times pulling force differences without any other parameter changes.

Hence, the next step of this project is we can design more different patterns by using stochastic reconstruction and generate a spectrum of the structure-property relations. Furthermore, we would like to use deep learning techniques to study this relations and inverse design the microstructure by input a demand property value.

REFERENCE

[1] S. Torquato and F. H. Stillinger, Local density fluctuations, hyperuniform systems, and order metrics, Phys.Rev. E 68, 041113 (2003).

[2] C. E. Zachary and S. Torquato, Hyperuniformity in point patterns and two-phase heterogeneous media, J. Stat. Mech.: Theory Exp. (2009) P12015.

[3] A. Gabrielli, M. Joyce, and F. Sylos Labini,Glass-like universe: Real-space correlation properties of standard cosmological models, Phys. Rev. D 65, 083523 (2002).

[4] A. Donev, F. H. Stillinger, and S. Torquato, Unexpected density fluctuations in disordered jammed hard-sphere packings, Phys. Rev. Lett. 95, 090604 (2005).

[5] C. E. Zachary, Y. Jiao, and S. Torquato, Hyperuni-form long-range correlations are a signature of disorderedjammed hard-particle packings, Phys. Rev. Lett. 106,178001 (2011).

[6] Y. Jiao and S. Torquato, Maximally random jammed packings of Platonic solids: Hyperuniform long-range correlations and isostaticity, Phys. Rev. E 84, 041309 (2011).

[7] D. Chen, Y. Jiao, and S. Torquato, Equilibrium phase behavior and maximally random jammed state of truncated tetrahedra, J. Phys. Chem. B 118, 7981 (2014).

[8] C. E. Zachary and S. Torquato, Anomalous local coordination, density fluctuations, and void statistics in disordered hyperuniform many-particle ground states, Phys.Rev. E 83, 051133

[9] S. Torquato, G. Zhang, and F. H. Stillinger, Ensemble theory for stealthy hyperuniform disordered ground states, Phys. Rev. X 5, 021020 (2015).

[10] O. U. Uche, F. H. Stillinger, and S. Torquato, Constraints on collective density variables: Two dimensions, Phys. Rev. E 70, 046122 (2004).

[11] R. D. Batten, F. H. Stillinger, and S. Torquato, Classical disordered ground states: Super-ideal gases, and stealth and equi-luminous materials, J. Appl. Phys. 104, 033504 (2008);

[12] R. D. Batten, F. H. Stillinger, and S. Torquato, Novel low-temperature behavior in classical many-particle systems, Phys. Rev. Lett. 103, 050602 (2009).

[13] J. L. Lebowitz, Charge fluctuations in Coulomb systems, Phys. Rev. A 27, 1491 (1983).

[14] G. Zhang, F. Stillinger, and S. Torquato, Ground states of stealthy hyperuniform potentials. I. Entropically favored configurations, Phys. Rev. E 92, 022119 (2015).

[15] G. Zhang, F. Stillinger, and S. Torquato, Ground states of stealthy hyperuniform potentials: II. Stacked-slider phases, Phys. Rev. E 92, 022120 (2015).

[16] L. Berthier, P. Chaudhuri, C. Coulais, O. Dauchot, and P. Sollich, Suppressed compressibility at large scale in jammed packings of size-disperse spheres, Phys. Rev. Lett. 106, 120601 (2011).

[17] R. Kurita and E. R. Weeks, Incompressibility of polydisperse random-close-packed colloidal particles, Phys. Rev. E 84, 030401 (2011).

[18] G. L. Hunter and E. R. Weeks, The physics of the colloidal glass transition, Rep. Prog. Phys. 75, 066501 (2012).

[19] R. Dreyfus, Y. Xu, T. Still, L. A. Hough, A. G. Yodh, and S. Torquato, Diagnosing hyperuniformity in two-dimensional, disordered, jammed packings of soft spheres, Phys. Rev. E 91, 012302 (2015).

[20] D. Hexner and D. Levine, Hyperuniformity of critical absorbing states, Phys. Rev. Lett. 114, 110602 (2015).

[21] R. L. Jack, I. R. Thompson, and P. Sollich, Hyperuniformity and phase separation in biased ensembles of trajectories for diffusive systems, Phys. Rev. Lett. 114, 060601(2015).

[22] J. H.Weijs, R. Jeanneret, R. Dreyfus, and D. Bartolo, Emergent hyperuniformity in periodically driven emulsions, Phys. Rev. Lett. 115, 108301 (2015).

[23] E. Tjhung and L. Berthier, Hyperuniform density fluctuations and diverging dynamic correlations in periodically driven colloidal suspensions, Phys. Rev. Lett. 114,148301 (2015).

[24] S. Torquato,A. Scardicchio, and C. E. Zachary, Point processes in arbitrary dimension from fermionic gases, random matrix theory, and number theory, J. Stat. Mech.: Theory Exp. (2008) P11019.

[25] R. P. Feynman and M. Cohen, Energy spectrum of the excitations in liquid helium, Phys. Rev. 102, 1189 (1956).

[26] Y. Jiao, T. Lau, H. Hatzikirou, M. Meyer-Hermann, J. C. Corbo, and S. Torquato,Avian photoreceptor patterns represent a disordered hyperuniform solution to a multi-scale packing problem, Phys. Rev. E 89, 022721 (2014).

[27] A. Mayer, V. Balasubramanian, T. Mora, and A. M. Walcza, How a well-adapted immune system is organized, Proc. Natl. Acad. Sci. USA 112, 5950 (2015).

[28] M. Hejna, P. J. Steinhardt, and S. Torquato, Nearly hyperuniform network models of amorphous silicon, Phys. Rev. B 87, 245204 (2013).

[29] R. Xie, G. G. Long, S. J. Weigand, S. C. Moss, T. Carvalho, S. Roorda, M. Hejna, S. Torquato, and P. J. Steinhardt, Hyperuniformity in amorphous silicon based on the measurement of the infinite-wavelength limit of the structure factor, Proc. Natl. Acad. Sci. USA 110, 13250 (2013).

[30] M. Florescu, S. Torquato, and P. J. Steinhardt, Designer disordered materials with large complete photonic band gaps, Proc. Natl. Acad. Sci. USA 106, 20658 (2009).

[31] W. Man, M. Florescu, K. Matsuyama, P. Yadak, G. Nahal, S. Hashemizad, E. Williamson, P. Steinhardt, S. Torquato, and P. Chaikin, Photonic band gap in isotropic hyperuniform disordered solids with low dielectric contrast, Opt. Express 21, 19972 (2013).

[32] W. Man, M. Florescu, E. P. Williamson, Y. He, S. R. Hashemizad, B. Y. C. Leung, D. R. Liner, S. Torquato, P. M. Chaikin, and P. J. Steinhardt, Isotropic band gaps and freeform waveguides observed in hyperuniform disordered photonic solids, Proc. Natl. Acad. Sci. USA 110, 15886 (2013).

[33] G. Zhang, F. H. Stillinger, and S. Torquato, Transport, Geometrical, and topological properties of stealthy disordered hyperuniform two-phase systems, J. Chem. Phys. 145, 244109 (2016).

[34] S. Torquato, Disordered hyperuniform heterogeneous materials, J. Phys.: Condensed Matt., 28, 414012 (2016).

[35] S. Torquato, Hyperuniformity and its generalizations, Phys. Rev. E 94, 022122 (2016).

[36] J. Haberko, N. Muller, and F. Scheffold, Direct laser writing of three dimensional network structures as templates for disordered photonicmaterials, Phys. Rev. A 88, 043822 (2013).

[37] G. Zito, G. Rusciano, G. Pesce, A. Malafronte, R. DiGirolamo, G. Ausanio, A. Vecchione, and A. Sasso, Nanoscale engineering of two-dimensional disordered hyperuniform blockcopolymer assemblies, Phys. Rev. E 92, 050601 (2015).

[38] C. L. Y. Yeong and S. Torquato, Reconstructing random media, Phys. Rev. E 57, 495 (1998).

[39] S. Torquato, Microstructure characterization and bulk properties of disordered two-phase media, J. Stat. Phys. 45, 843 (1986).

[40] S. Torquato, Random Heterogeneous Materials: Microstructure and Macroscopic Properties, New York: Springer (2002).

[41] Y. Jiao, F. H. Stillinger, and S. Torquato, Modeling heterogeneous materials via two-Point correlation functions: Basic principles, Phys. Rev. E. 76, 031110 (2007).

[42] Y. Jiao, F. H. Stillinger, and S. Torquato, Modeling heterogeneous materials via two-point correlation functions: II. Algorithmic details and applications, Phys. Rev. E 77, 031135 (2008).

[43] Y. Jiao, F. H. Stillinger, and S. Torquato, A superior descriptor of random textures and its predictive capacity, Proc. Natl. Acad. Sci. 106, 17634 (2009).

[44] C. Gommes, Three-dimensional reconstruction of liquid phases in disordered mesopores using in situ small-angle scattering, J. Appl. Crystal. 46, 493 (2013).

[45] A. P. Roberts, Statistical reconstruction of three-dimensional porous media from two-dimensional images, Phys. Rev. E 56, 3203 (1997).

[46] D. T. Fullwood, S. R. Kalidindi, S. R. Niezgoda, A. Fast, and N. Hampson, Gradient-based microstructure reconstructions from distributions using fast Fourier transforms, Mater. Sci. Eng. A 494, 68 (2008)

[47] D. T. Fullwood, S. R. Niezgoda, and S. R. Kalidindi, Microstructure reconstructions from 2-point statistics using phase-recovery algorithms, Acta Mater. 56, 942 (2008).

[48] A. Hajizadeh , A. Safekordi, and F. A. Farhadpour, A multiple-point statistics algorithm for 3D pore space reconstruction from 2D images, Adv. Water. Res. 34, 1256 (2011).

[49] P. Tahmasebi and M. Sahimi, Cross-correlation function for accurate reconstruction of heterogeneous media, Phys. Rev. Lett. 110, 078002 (2013).

[50] M. G. Rozman and U. Utz, Uniqueness of reconstruction of multiphase morphologies from two-point correlation functions, Phys. Rev. Lett. 89, 135501 (2002).

[51] T. Tang, Q. Teng, X. He and D. Luo, A pixel selection rule based on the number of differentphase neighbours for the simulated annealing reconstruction of sandstone microstructure, J. Microscopy 234, 262 (2009).

[52] L. M. Pant, S. K. Mitra, and M. Secanell, Stochastic reconstruction using multiple correlation functions with different-phase-neighbor-based pixel selection, Phys. Rev. E 90, 023306 (2014).

[53] Y. Jiao, E. Pallia, and N. Chawla, Modeling and predicting microstructure evolution in lead/tin alloy via correlation functions and stochastic material reconstruction, Acta Mater. 61, 3370 (2013).

[54] S. Singh, J. J. Williams, Y. Jiao, and N. Chawla, Modeling anisotropic multiphase heterogeneous materials via direction correlation functions: Simulations and experimental verification, Metall. Mater. Trans. A 43, 4470 (2012).

[55] K. M. Gerke, M. V. Karsanina, R. V. Vasilyev, and D. Mallants, Improving pattern reconstruction using directional correlation functions, EPL 106, 66002 (2014).

[56] Y. Jiao and N. Chawla, Modeling and characterizing anisotropic inclusion orientation in heterogeneous material via directional cluster functions and stochastic microstructure, J. Appl. Phys. 115, 093511 (2014).

[57] H. Li, N. Chawla, and Y. Jiao Reconstruction of heterogeneous materials via stochastic optimization of limited angle X-ray tomographic projections, Scripta Mater. 86, 48 (2014).

[58] S. Chen, H. Li, and Y. Jiao Dynamic reconstruction of heterogeneous materials and microstructure evolution, Phys. Rev. E 92, 023301 (2015).

[59] H. Li, C. S. Kaira, J. Mertens, N. Chawla, and Y. Jiao Accurate stochastic reconstruction of heterogeneous microstructures by limited X-ray tomographic projections, J. Microscopy 264, 339 (2016).

[60] S. Chen, A. Kirubanandham, N. Chawla and Y. Jiao Stochastic multi-scale reconstruction of 3D microstructure consisting of polycrystalline grains and second-phase particles from 2D micrographs, Metall. Mater. Trans. A 47, 1440 (2016).

[61] S. Kirkpatrick, C. D. Gelatt, and M. P. Vecchi, Optimization by simulated annealing, Science 220, 671 (1983).

[62] H. Chen, E. Lin, Y. Jiao, and Y. Liu, A generalized 2D non-Local lattice spring model for fracture simulation, Comput. Mech. 54, 1541 (2014).

[63] H. Chen, Y. Jiao and Y. Liu, A nonlocal lattice particle model for fracture simulation of anisotropic materials, Composites Part B 90, 141 (2016).

[64] H. Chen, Y. Jiao, and Y. Liu, Investigating the microstructural effect on elastic and fracture behavior of polycrystals using a nonlocal lattice-particle model, Mater.Sci. Eng. A 631, 173 (2015).

[65] H. Chen, Y. Xu, Y. Jiao and Y. Liu, A novel discrete computational tool for microstructure-sensitive mechanical analysis of composite materials, Mater.Sci. Eng. A659, 234 (2016).

[66] H. Chen, L. Meng, S. Chen, Y. Jiao and Y. Liu, Numerical investigation of microstructure effect on mechanical properties of bi-continuous and particulate re-inforced composite materials, Comput. Mater. Sci. 122, 288 (2016).

[67] W.X. Xu, F. Wu, Y. Jiao, M. Liu, A general micromechanical framework of effective moduli for the design of nonspherical nano- and micro-particle reinforced composites with interface properties. Materials & Design, (2017).

[68] W.X. Xu, H.F. Ma, S.Y. Ji, H.S. Chen, Analytical effective elastic properties of particulate composites with soft interfaces around anisotropic particles, Compos. Sci. Technol. 129, 10 (2016).

[69] Friedl P and Gilmour D 2009 Collective cell migration in morphogenesis, regeneration and cancer Nat. Rev. Mol. Cell Biol. 10 445

[70] AmanA and Piotrowski T 2010 Cell migration during morphogenesis Dev. Biol. 341 20–33

[71] Friedl P, Noble P B, Walton PA, Laird DW, Chauvin P J, TabahRJ, Black M and ZänkerKS 1995 Migration of coordinated cell clusters in mesenchymal and epithelial cancer explants in vitroCancer Res. 55 4557–60

[72] Gjorevski N and NelsonC M 2011 Integrated morphodynamic signalling of the mammary gland Nat. Rev. Mol. Cell Biol. 12 581

[73] VaeziA, BauerC, VasioukhinV and Fuchs E 2002 Actin cable dynamics and Rho/Rock orchestrate a polarized cytoskeletal architecture in the early steps of assembling a stratified epithelium Dev. Cell 3 367–81

[74] Werner S, Krieg T and Smola H 2007 Keratinocyte–fibroblast interactions in wound healing J. Invest. Dermatol. 127 998–1008

[75] Ochoa-EspinosaA and Affolter M 2012 Branching morphogenesis: from cells to organs and back Cold Spring Harbor Perspect. Biol. 4 a008243

[76] Mittelbrunn M and Sánchez-Madrid F 2012 Intercellular communication: diverse structures for exchange of genetic information Nat. Rev. Mol. Cell Biol. 13 328

[77] Agnati L F, Zoli M, Strömberg I and FuxeK 1995 Intercellular communication in the brain: wiring versus volume transmission Neuroscience 69 711

[78] TrepatX, Wasserman M R, Angelini T E, Millet E, Weitz DA, ButlerJ P and Fredberg J 2009 Physical forces during collective cell migration Nat. Phys. 5 426

[79] Friedl P, Wolf K and Zegers M M 2014 Rho-directed forces in collective migration Nat. Cell Biol. 16 208

[80] Grinnell F and PetrollWM 2010 Cell motility and mechanics in three-dimensional collagen matrices Annu. Rev. Cell Dev. Biol. 26 335–61

[81] MaX, Schickel M E, Stevenson M D, Sarang-SieminskiAL, GoochKJ, Ghadiali S N and HartRT 2013 Fibers in the extracellular matrix enable long-range stress transmission between cells Biophys. J. 104 1410–8

[82] Liang L, JonesC, Chen S, Sun B and JiaoY 2016 Heterogeneous force network in 3D cellularized collagen networks Phys. Biol. 13 066001

[83] DuFortCC, Paszek M J and WeaverV M 2011 Balancing forces: architectural control of mechanotransduction Nat. Rev. Mol. Cell Biol. 12 308

[84] JonesCAR, Cibula M, Feng J, Krnacik EA, McIntyre D H, Levine H and Sun B 2015 Micromechanics of cellularized biopolymer networks Proc. Natl Acad. Sci. USA112 E5117

[85] Hall M S, Alisafaei F, Ban E, FengX, HuiC, ShenoyVB and Wu M 2016 Fibrous nonlinear elasticity enables positive mechanical feedback between cells and ecms Proc. Natl Acad. Sci. USA113 14043 [18] ValenciaA M J et al 2015 Collective cancer cell invasion induced by coordinated contractile stresses Oncotarget 6 43438

[86] Gjorevski N, PiotrowskiAS, VarnerV D and NelsonC M 2015 Dynamic tensile forces drive collective cell migration through three-dimensional extracellular matrices Sci. Rep. 5 11458

[87] Kim J, JonesCAR, Groves N and Sun B 2016 Threedimensional reflectance traction microscopy PLoS One 11 e0156797

[88] AlobaidiA and Sun B 2016 Probing three-dimensional collective cancer invasion with DIGME Cancer Convergence at press (arxiv:1608.06723)

[89] Lindström S B, Vader DA, KulachenkoA and Weitz DA 2010 Biopolymer network geometries: characterization, regeneration, and elastic properties Phys. Rev. E 82 051905

[90] Torquato S and JiaoY 2009 Dense packings of platonic and archimedean solids Nature 460 876

[91] Chen H, Lin E, JiaoY and LiuY 2014 A generalized 2d non-local lattice spring model for fracture simulation Comput. Mech. 54 1541

[92] Chen H, XuY, JiaoY and LiuY 2016 A novel discrete computational tool for microstructure-sensitive mechanical analysis of composite materials materials Mater. Sci. Eng. A 659 234

[93] JiaoY, Stillinger F H and Torquato S 2009 A superior descriptor of random textures and its predictive capacity Proc. Natl Acad. Sci. 106 17634

[94] Sun B, Duclos G and Stone HA 2013 The network characteristics of collective chemosensing Phys. Rev. Lett. 110 158103

[95] Poujade M, Grasland-Mongrain E, HertzogA, Jouanneau J, Chavrier P, Ladoux B, BuguinA and Silberzan P 2007 Collective migration of an epithelial monolayer in response to a model wound Proc. Natl Acad. Sci. 104 15988

[96] Tao J and Sun SX 2015 Active biochemical regulation of cell volume and a simple model of cell tension response Biophys. J. 109 1541–50

[97] Ye, Z., et al., Phase Change of Gallium Enables Highly Reversible and Switchable Adhesion. Advanced Materials, 2016. 28(25): p. 5088-5092.

[98] Purtov, J., M. Frensemeier, and E. Kroner, Switchable Adhesion in Vacuum Using Bio-Inspired Dry Adhesives. Acs Applied Materials & Interfaces, 2015. 7(43): p. 24127-24135.

[99] Schubert, B.E. and D. Floreano, Variable stiffness material based on rigid low-melting-point-alloy microstructures embedded in soft poly(dimethylsiloxane) (PDMS). Rsc Advances, 2013. 3(46): p. 24671-24679.

[100] McKnight, G. and C. Henry, Variable stiffness materials for reconfigurable surface applications. Smart Structures and Materials 2005: Active Materials: Behavior and Mechanics, 2005. 5761: p. 119-126.

[101] Shan, W.L., et al., Rigidity-tuning conductive elastomer. Smart Materials and Structures, 2015. 24(6): p. 065001.

[102] Shan, W.L., T. Lu, and C. Majidi, Soft-matter composites with electrically tunable elastic rigidity. Smart Materials and Structures, 2013. 22(8): p. 085005.

[103] McEvoy, M.A. and N. Correll, Thermoplastic variable stiffness composites with embedded, networked sensing, actuation, and control. Journal of Composite Materials, 2015. 49(15): p. 1799-1808.

[104] Van Meerbeek, I.M., et al., Morphing Metal and Elastomer Bicontinuous Foams for Reversible Stiffness, Shape Memory, and Self-Healing Soft Machines. Advanced Materials, 2016. 28(14): p. 2801-2806.

[105] Shan, W.L., et al., Thermal analysis and design of a multi-layered rigidity tunable composite. International Journal of Heat and Mass Transfer, 2013. 66: p. 271-278.

[106] Majidi, C., Soft Robotics: A Perspective-Current Trends and Prospects for the Future. Soft Robotics, 2014. 1(1): p. 5-11.

[107] Roberts, P., et al., Soft-Matter Capacitive Sensor for Measuring Shear and Pressure Deformation. 2013 Ieee International Conference on Robotics and Automation (ICRA), 2013: p. 3529-3534.

[108] Fassler, A. and C. Majidi, Liquid-Phase Metal Inclusions for a Conductive Polymer Composite. Advanced Materials, 2015. 27(11): p. 1928-1932.

[109] Lazarus, N., C.D. Meyer, and W.J. Turner, A microfluidic wireless power system. Rsc Advances, 2015. 5(96): p. 78695-78700.

[110] Dickey, M.D., et al., Eutectic gallium-indium (EGaIn): A liquid metal alloy for the formation of stable structures in microchannels at room temperature. Advanced Functional Materials, 2008. 18(7): p. 1097-1104.

[111] Mohammadi Nasab, A., et al., A Soft Gripper with Rigidity Tunable Elastomer Strips as Ligaments. Soft Robotics, 2017.

[112] Tatari, M., et al., Dynamically Tunable Reversible Dry Adhesion Enabled by Rapid Drastic Stiffness Tuning. In Preparation, 2017.

[113] Baruchel, J., J.-Y. Buffiere, and E. Maire, X-ray tomography in material science. 2000.

[114] Kinney, J.H. and M.C. Nichols, X-ray tomographic microscopy (XTM) using synchrotron radiation. Annual review of materials science, 1992. 22(1): p. 121-152.

[115] Singh, S.S., et al., 3D microstructural characterization and mechanical properties of constituent particles in Al 7075 alloys using X-ray synchrotron tomography and nanoindentation. Journal of Alloys and Compounds, 2014. 602: p. 163-174.

[116] Weck, A., et al., Visualization by X-ray tomography of void growth and coalescence leading to fracture in model materials. Acta Materialia, 2008. 56(12): p. 2919-2928.

[117] Jiao, Y., F. Stillinger, and S. Torquato, Modeling heterogeneous materials via two-point correlation functions: Basic principles. Physical Review E, 2007. 76(3): p. 031110.

[118] Jiao, Y., F. Stillinger, and S. Torquato, Modeling heterogeneous materials via two-point correlation functions. II. Algorithmic details and applications. Physical Review E, 2008. 77(3): p. 031135.

[119] Jiao, Y., F. Stillinger, and S. Torquato, A superior descriptor of random textures and its predictive capacity. Proceedings of the National Academy of Sciences, 2009. 106(42): p. 17634-17639.

[120] Chen, H., Y. Jiao, and Y. Liu, A Nonlocal Lattice Particle Model for Fracture Simulation of Anisotropic Materials. Composites Part B: Engineering, 2016.

[121] Chen, H., et al., A generalized 2D non-local lattice spring model for fracture simulation. Computational Mechanics, 2014. 54(6): p. 1541-1558.

[122] Chen, H. and Y. Liu, A non-local 3D lattice particle framework for elastic solids. International Journal of Solids and Structures, 2015.

[123] Chen, H., Y. Jiao, and Y. Liu, Investigating the microstructural effect on elastic and fracture behavior of polycrystals using a nonlocal lattice particle model. Materials Science and Engineering: A, 2015. 631: p. 173-180.

[124] Chen, H., et al., Numerical investigation of microstructure effect on mechanical properties of bi-continuous and particulate reinforced composite materials. Computational Materials Science, 2016. 122: p. 288-294.

[125] Chen, H., et al., A novel discrete computational tool for microstructure-sensitive mechanical analysis of composite materials. Materials Science and Engineering: A, 2016. 659: p. 234-241.

[126] Sigmund, O. and S. Torquato. Design of materials with extreme thermal expansion using a three-phase topology optimization method. in Smart Structures and Materials' 97. 1997. International Society for Optics and Photonics.

[127] Sigmund, O. and S. Torquato, Design of smart composite materials using topology optimization. Smart Materials and Structures, 1999. 8(3): p. 365.

[128] Sigmund, O., S. Torquato, and I.A. Aksay, On the design of 1–3 piezocomposites using topology optimization. Journal of materials research, 1998. 13(04): p. 1038-1048.

[129] Cang, R., et al., Microstructure Representation and Reconstruction of Heterogeneous Materials via Deep Belief Network for Computational Material Design. Journal of Mechanical Design, 2017. 139(7): p. 071404.

[130] Aureli, M., et al., Non-equilibrium microscale thermomechanical modeling of bimetallic particulate fractal structures during ball milling fabrication. Journal of Applied Physics, 2017. 122(2).

[131] Li, J., et al., Laser Shock-Based Platform for Controllable Forming of Nanowires. Nano Letters, 2012. 12(6): p. 3224-3230.

[132] Liu, Z.K., et al., Direction-tunable nanotwins in copper nanowires by laser-assisted electrochemical deposition. Nanotechnology, 2012. 23(12).

[133] Liao, Y.L., Y.L. Yang, and G.J. Cheng, Enhanced Laser Shock by an Active Liquid Confinement-Hydrogen Peroxide. Journal of Manufacturing Science and Engineering-Transactions of the Asme, 2012. 134(3).

[134] Zhu, Z.T., et al., Aligned electrospun ZnO nanofibers for simple and sensitive ultraviolet nanosensors. Chemical Communications, 2009(18): p. 2568-2570.

[135] Liao, Y.L., et al., Preparation, characterization, and encapsulation/release studies of a composite nanofiber mat electrospun from an emulsion containing poly(lactic-co-glycolic acid). Polymer, 2008. 49(24): p. 5294-5299.

[136] Bayrak, A.E., Y. Ren, and P.Y. Papalambros, Topology Generation for Hybrid Electric Vehicle Architecture Design. Journal of Mechanical Design, 2016. 138(8): p. 081401.

[137] Ren, Y., H. Lee, R. Gonzalez, and P.Y. Papalambros, Improving Design Preference Prediction Accuracy Using Feature Learning. Ann Arbor. 1001: p. 48109.

[138] Jones, C.A.R., et al., The spatial-temporal characteristics of type I collagen-based extracellular matrix. Soft Matter, 2014. 10(44): p. 8855-8863.

[139] Chen, S., et al., Enhancing the physical modeling capability of open-source MFIX-DEM software for handling particle size polydispersity: Implementation and validation. Powder Technology, 2017. 317: p. 117-125.

[140] Torquato, S. and G. Stell, Microstructure of two-phase random media. I. The n-point probability functions. The Journal of Chemical Physics, 1982. 77(4): p. 2071-2077.

[141] Torquato, S. and G. Stell, Microstructure of two-phase random media. III. The n-point matrix probability functions for fully penetrable spheres. The Journal of chemical physics, 1983. 79(3): p. 1505-1510.

[142] Torquato, S. and G. Stell, Microstructure of two-phase random media. V. The n-point matrix probability functions for impenetrable spheres. The Journal of chemical physics, 1985. 82(2): p. 980-987.

[143] Prager, S., Interphase transfer in stationary two-phase media. Chemical Engineering Science, 1963. 18(4): p. 227-231.

[144] Torquato, S., Interfacial surface statistics arising in diffusion and flow problems in porous media. The Journal of chemical physics, 1986. 85(8): p. 4622-4628.

[145] Lu, B. and S. Torquato, Lineal-path function for random heterogeneous materials. Physical Review A, 1992. 45(2): p. 922.

[146] Lu, B. and S. Torquato, Lineal-path function for random heterogeneous materials. II. Effect of polydispersivity. Physical Review A, 1992. 45(10): p. 7292.

[147] Torquato, S. and M. Avellaneda, Diffusion and reaction in heterogeneous media: Pore size distribution, relaxation times, and mean survival time. The Journal of chemical physics, 1991. 95(9): p. 6477-6489.

[148] Cinlar, E. and S. Torquato, Exact determination of the two-point cluster function for one-dimensional continuum percolation. Journal of statistical physics, 1995. 78(3-4): p. 827-839.

[149] Torquato, S., Random heterogeneous materials: microstructure and macroscopic properties. Springer Science & Business Media, 2013. 16.

[150] Friedman, H., et al., Micro- and nano-spheres of low melting point metals and alloys, formed by ultrasonic cavitation. Ultrasonics Sonochemistry, 2013. 20(1): p. 432-444.

[151] Friedman, H., et al., Formation of metal microspheres by ultrasonic cavitation. Journal of Materials Research, 2010. 25(4): p. 633-636.

[152] Pyatenko, A., et al., Synthesis of silver nanoparticles by laser ablation in pure water. Applied Physics a-Materials Science & Processing, 2004. 79(4-6): p. 803-806.

[153] Dolgaev, S.I., et al., Nanoparticles produced by laser ablation of solids in liquid environment. Applied Surface Science, 2002. 186(1-4): p. 546-551.

[154] Bozon-Verduraz, F., et al., Production of nanoparticles by laser-induced ablation of metals in liquids. Quantum Electronics, 2003. 33(8): p. 714-720.

[155] Yang, G.W., Laser ablation in liquids: Applications in the synthesis of nanocrystals. Progress in Materials Science, 2007. 52(4): p. 648-698.

[156] Lowrie, N. How to make a metal foam. 2012;

[157] Guest, J.K., J.H. Prévost, and T. Belytschko, Achieving minimum length scale in topology optimization using nodal design variables and projection functions. International journal for numerical methods in engineering, 2004. 61(2): p. 238-254.

[158] Wang, F., B.S. Lazarov, and O. Sigmund, On projection methods, convergence and robust formulations in topology optimization. Structural and Multidisciplinary Optimization, 2011. 43(6): p. 767-784.

[159] Marck, G., et al., Topology optimization using the SIMP method for multiobjective conductive problems. Numerical Heat Transfer, Part B: Fundamentals, 2012. 61(6): p. 439-470.

[160] Allaire, G., F. Jouve, and A.-M. Toader, Structural optimization using sensitivity analysis and a level-set method. Journal of computational physics, 2004. 194(1): p. 363-393.

[161] Wang, M.Y., X. Wang, and D. Guo, A level set method for structural topology optimization. Computer methods in applied mechanics and engineering, 2003. 192(1): p. 227-246.

[162] Arora, J.S. and E.J. Haug, Methods of design sensitivity analysis in structural optimization. AIAA journal, 1979. 17(9): p. 970-974.

[163] Komkov, V., K.K. Choi, and E.J. Haug, Design sensitivity analysis of structural systems. Vol. 177. 1986: Academic press.

[164] Myers, R.H., D.C. Montgomery, and C.M. Anderson-Cook, Response surface methodology: process and product optimization using designed experiments. 2016: John Wiley & Sons.

[165] He, K., et al. Deep residual learning for image recognition. in Proceedings of the IEEE conference on computer vision and pattern recognition. 2016.

[166] Simonyan, K. and A. Zisserman, Very deep convolutional networks for large-scale image recognition. arXiv preprint arXiv:1409.1556, 2014.

[167] Chen, S., et al., Stochastic Multi-Scale Reconstruction of 3D Microstructure Consisting of Polycrystalline Grains and Second-Phase Particles from 2D Micrographs. Metallurgical and Materials Transactions A, 2016. 47: p. 1-11.

[168] Chen, S., H. Li, and Y. Jiao, Dynamic reconstruction of heterogeneous materials and microstructure evolution. Physical Review E, 2015. 92(2): p. 023301.

[169] Chen, S., Y. Xu, and Y. Jiao, Modeling morphology evolution and densification during solid-state sintering via kinetic Monte Carlo simulation. Modelling and Simulation in Materials Science and Engineering, 2016. 24(8): p. 085003.

[170] Guo, E.-Y., et al., Accurate modeling and reconstruction of three-dimensional percolating filamentary microstructures from two-dimensional micrographs via dilation-erosion method. Materials Characterization, 2014. 89: p. 33-42.

[171] Jiao, Y., Three-Dimensional Heterogeneous Material Microstructure Reconstruction from Limited Morphological Information via Stochastic Optimization. AIM Materials Science, 2014. 28.

[172] Jiao, Y., A Generalized Lattice-Point Method for Reconstructing Heterogeneous Materials from Lower-Order Correlation Functions. Ann J Materials Sci Eng, 2014. 1(1): p. 11.

[173] Jiao, Y. and N. Chawla, Three dimensional modeling of complex heterogeneous materials via statistical microstructural descriptors. Integrating Materials and Manufacturing Innovation, 2014. 3(1): p. 1-19.

[174] Jiao, Y. and N. Chawla, Modeling and characterizing anisotropic inclusion orientation in heterogeneous material via directional cluster functions and stochastic microstructure reconstruction. Journal of Applied Physics, 2014. 115(9): p. 093511.

[175] Jiao, Y., E. Padilla, and N. Chawla, Modeling and predicting microstructure evolution in lead/tin alloy via correlation functions and stochastic material reconstruction. Acta Materialia, 2013. 61(9): p. 3370-3377.

[176] Li, H., N. Chawla, and Y. Jiao, Reconstruction of heterogeneous materials via stochastic optimization of limited-angle X-ray tomographic projections. Scripta Materialia, 2014. 86: p. 48-51.

[177] Li, H., et al., Accurate Stochastic Reconstruction of Heterogeneous Microstructures by Limited X-ray Tomographic Projections. Journal of microscopy, 2016. 264: p. 339.

[178] Li, H., et al., Direct Extraction of Spatial Correlation Functions from Limited X-ray Tomography Data for Microstructure Quantification. in preparation, 2017.

[179] Li, H., et al., Microstructural Quantification and Property Prediction Using Limited X-ray Tomography Data. JOM, 2016. 68: p. 2288.

[180] Singh, S., et al., Direct prediction of mechanical properties of polymer-matrix composites from limited x-ray tomography data. in preparation, 2017

[181] R. Cang, and M.Y. Ren. Deep Network-Based Feature Extraction and Reconstruction of Complex Material Microstructures. in ASME 2016 International Design Engineering Technical Conferences and Computers and Information in Engineering Conference. 2016. American Society of Mechanical Engineers.

[182] C. Majidi. Soft robotics:a perspective-current trends and prospects for the future. Soft Robotics, 1:5–11, 2013.